Studies of oxide Nanostructures of TiO_2, ZnO, NiO & Ion Beam Patterned Surfaces for Photo-absorption and Resistive Switching Properties

By

Vanarajsinh Jashavantsinh Solanki

PHYS07200804008

Institute of Physics, Bhubaneswar

A thesis submitted to the
Board of Studies in Physical Sciences

In partial fulfillment of requirements
For the Degree of

DOCTOR OF PHILOSOPHY
of
HOMI BHABHA NATIONAL INSTITUTE

January, 2016

STATEMENT BY AUTHOR

This dissertation has been submitted in partial fulfillment of requirements for an advanced degree at Homi Bhabha National Institute (HBNI) and is deposited in the Library to be made available to borrowers under rules of the HBNI.

Brief quotations from this dissertation are allowable without special permission, provided that accurate acknowledgment of source is made. Requests for permission for extended quotation from or reproduction of this manuscript in whole or in part may be granted by the Competent Authority of HBNI when in his or her judgment the proposed use of the material is in the interests of scholarship. In all other instances, however, permission must be obtained from the author.

(Vanarajsinh Jashavantsinh Solanki)

CERTIFICATE

This is to certify that the thesis entitled "**Studies of oxide Nanostructures of TiO_2, ZnO, NiO & Ion Beam Patterned Surfaces for Photo-absorption and Resistive Switching Properties**", which is being submitted by **Mr. Vanarajsinh Jashavantsinh Solanki**, in partial fulfillment of the degree of **Doctor of Philosophy in Physics** of **Homi Bhabha National Institute** is a record of his own research work carried by him. He has carried out his investigations for the last six years on the subject matter of the thesis under my supervision at **Institute of Physics, Bhubaneswar**. To the best of our knowledge, the matter embodied in this thesis has not been submitted for the award of any other degree.

Signature of the Candidate **Signature of the Supervisor**

Vanarajsinh Jashavantsinh Solanki
Institute of Physics
Bhubaneswar

Prof. Shikha Varma
Professor
Institute of Physics
Bhubaneswar

DECLARATION

I, hereby declare that the investigation presented in the thesis has been carried out by me. The work is original and has not been submitted earlier as a whole or in part for a degree/diploma at this or any other Institution/University.

(Vanarajsinh Jashavantsinh Solanki)

To my Parents

Contents

Acknowledgement

This thesis is the result of nearly six years of research work that I have carried out in the group of SPM/XPS laboratory, Institute of Physics, Bhubaneswar. Certainly, the work described here could not have been accomplished without the help of many people. I have received a lot of support both in my everyday job and life. Now, at the end of my IoP adventure, is the perfect time to give my sincere gratitude.

First and foremost I am grateful for having Prof. Shikha Varma as my Ph.D advisor. Shikha's steady leadership and motto of focusing on "how far we have come" rather than "how far we need to go" was one of the driving force in carrying this long journey through the toughest of times. Her ability to understand the essence of what others try to say, no matter how vague they make the arguments, helped me to transform my clumsy work to something meaningful. She also provided me enough freedom to work in my own way. It has been amazing to witness and learn from her special ability to communicate delicate physical concepts in scientific writing, presentation, and discussion.

The another person I would like to thank is Prof. Ajit Mohan Srivastava. A million dollar smile on his face let you pretermit all the sorrows and sadness. His unique approach to general physics infused within me the idea that physics is not always about solving problems; it is also about being able to listen to different perspectives. It was fun amidst his company during tea time, pizza parties and movie session at his home on a glorious "Big Screened, 46 inch, LED TV".

It was almost impossible to finish this journey without supporting, forgiving, well wisher and loving friends. For my case, it was Pramita who played this role together with Tanmoy and Raghav. These are the people with whom I had celebrated my B'day first time in my life. I will never forget "The Chilika Trip" with these buddies. They graced my stay at IoP with cooking parties, evening and late night roaming in campus. A special thank to my dearest friend Pramita who was always there to cheer me up and take away my frowns. I am simply very lucky to have such a beautiful human being as a friend. Memories of arguments during discussions, her addiction towards "Gujarati kadhi and Lassi", confusions during cooking and her innocent replies will always bring a smile on my face. A last piece of chocolate will always make me recollect her cherish. If I have to choose between walking with a friend like her in the dark or alone in the light, I prefer dark. I thank her with all my heart.

A graduate life at IoP is not all about research. Many friends during this period made me a socially acceptable being, I believe. Specially, thanks to Abhishek and Trilochan for their continuous encouragement and support. It is almost difficult to irritate Abhishek except when asking him to sing a famous song ”jhumka gira re ”. No doubt he is a good singer but his practice session on harmonium was annoying and anyway I have to prove my leg pulling capability. The late night tea time gossips with Trilochan and his mimicry are unforgettable. I would also like to thank Ashutosh and Jatish for arranging our first outstanding trip to Harishankarpur. All players in the football and lawn tennis team, members of Khichdi party and IoP express magazine, deserve my acknowledgement.

I am thankful to the people in my group, who always supported me and made me a part of their social as well as academic activities. I wish to extend my hearty thank to Dipak, Dr. Ramarao, Dr. Anupama, Subrata, Indrani, Shalik, Priyadarshini and Ashish. I am very thankful to Mr. Santosh Choudhury, the backbone of our XPS laboratory, not only for his support in all the experiments but also for accepting me as his family member. He and his family never let me feel away from home. I really miss their hospitality and outing in his car.

I would also like to acknowledge all the members who helped me on the professional front. I wish to express my warm thanks to Dr. D. Kanjilal, Dr. D. Avasthi and Dr. Kabiraj for their help and useful guidance during experiments at Inter University Accelerator Center (IUAC), New Delhi. I am also thankful to all the member of material science group at IUAC. Prof. P. V. Satyam, Prof. B. R. Shekhar, Prof. N. C. Mishra, Prof. S. N. Sahoo, Dr. S. Rath and Vantari Siva also deserve my sincere acknowledgement. I am grateful to all my teachers starting from school days to predoctoral course work without their encouragements this journey may not have reached at this level.

I am also thankful to my doctoral committee members, Prof. T. Som, Prof. P. Agrawal and Dr. P. K. Sahoo for their useful guideline and comments which helped me to improve my work to satisfactory level. I am also grateful to DAE for the financial support and the grant in terms of the fellowship and the contingency. I would also like to thank HBNI and SERB’s international travel support scheme for hosting my expenses during international conference ”IBMM-2014” held at Leuven, Belgium. I wish to express my warm thanks to all IoP members including technical as well as library and administrative staffs for their timely help.

Last but not least, my deepest gratitude to my dearest parents, brothers and my loving wife Neeta. I want to especially thank my mother for her understanding and support. She had never

complained for my short stay at home during last seven years but her eyes always do. I am also thankful to all of my family for their continued supports and the cultural environment they have raised me up in. I am very grateful to my beloved wife Neeta, for her love, care, fondness and kind support to reach at this stage. Her philosophies that used to be incomprehensible to me at some point of time, have gradually become a powerful belief that kept my mind focused, peacefully and joyfully, in the heat of scientific research. At this stage, I could not forget to thank my cutest and affectionate nephew, Aviraj, and sweetest niece, Ishikha, for making my stay joyful and very busy at home, in the last three years.

Date: **Vanarajsinh Jashavantsinh Solanki**

Synopsis

Frontier areas of fundamental as well as application oriented research motivate for and demand nanostructures with exciting functional properties [1–3]. With this focus, a variety of routes are being extensively utilized to develop nano- dimensional structures and patterns having tailor made characteristics. Achieving nanostructures through self-assembly is an active area of research exhibiting impressive results with far reaching consequences. Often the exceptional advantages stem from their uncomplicated fabrication processes. Oxide semiconductors demonstrate many exciting properties at nano- dimensional scales. Expression of many new and accentuated properties in the fields of photovoltaics, photocatalysis, sensors, optoelectronics, memory devices etc. [1, 2, 4–6] by these nanostructures have led to intensive efforts for designing and controlling their behavior.

In the present thesis, fabrication of metal oxide nanostructures of TiO_2, ZnO and NiO have been investigated by a variety of methods. Low energy irradiation techniques have been utilized for developing the nanostructures for TiO_2 and ZnO, whereas NiO nanostructures have been grown by hydrothermal method. Developed by self organized assembly processes, these nanostructures demonstrate many interesting properties, like enhanced photoabsorption behaviour, magnetic response, resistive switching characteristics etc. These have been primarily achieved through the control on fabrication parameters.

The first part of this thesis discusses the photo absorption and magnetic behavior of rutile titania nanostructures through ion beam sputtering of TiO_2 (110) surfaces by argon ions of 60 keV from an ECR source. A modulation in the size and properties of the nanostructures is observed as a function of ion fluence which was varied from 5×10^{15} to 5×10^{17} ions/cm^2. Ion irradiation causes the surfaces to evolve by two dominant processes, erosion and surface diffusion [7–9]. The surface morphology, thus, develops as a consequence of competition between variety of processes like roughening dynamics, relaxation processes, generation of defects, material transport etc. [10, 11]. Fabrication of self organized structures, by ion irradiation process, is an attractive route for creating self organized regular arrays and patterns of nanostructures on large area by technologically simple single step procedure. Techniques of Scanning Probe Microscopy (SPM), X-ray Photoelectron Spectroscopy (XPS), X-ray diffraction (XRD), Optical (UV-Vis) absorption spectroscopy, Photoluminescence (PL) and Superconducting Quantum Interference Device (SQUID) have been utilized here. Ion irradiation of bi-component surfaces

can lead to the preferential sputtering of low mass atoms. This promotes the formation of Ti-rich zones on the surface, along with oxygen vacancy sites, resulting in the nucleation of self-assembled nanodots. A significant increase in photo absorbance is demonstrated by all the nanostructured surfaces studied here [12, 13]. Surprisingly, the highest photo-absorption response is observed from the small nanostructures (15nm) conjugated with largest oxygen vacancies, and not the smaller nanostructures with larger surface area. In addition, increase of optical bandgap, $\sim$0.1 eV, is also observed for nanostructured surfaces, due to the pronounced quantum confinement effect. With the detailed quantitative investigation of oxygen vacancy states, it is observed that the competition between the size of nanostructures and the number of vacancy states controls the photo- absorption response of TiO_2 nanostructures. The complex relationship between these factors is responsible for the observed anomalous absorption response. The results from photoluminescence spectroscopy display lowered PL intensity for ion irradiated surfaces, compared to pristine. This is caused by the decreased charge carrier recombination, through trapping, by the oxygen vacancies. The observed results, in the absence of any dopant material, can have extensive implications in the area of TiO_2 based photo-voltaic and photocatalytic devices.

The magnetic properties of these TiO_2 nanostructures, fabricated by ion sputtering of TiO_2 (110) surfaces, have also been investigated here [14]. TiO_2 has attracted immense attention in the oxide based dilute magnetic semiconductor (DMS) technology after discovery of room temperature ferromagnetism (FM) in Co-doped anatase TiO_2 thin films [15]. Existence of oxygen vacancies and nano-dimensions significantly modulate the magnetic nature and properties of the nanophase materials. Results from magnetic studies of TiO_2 nanostructures (of size 5, 10, 25 nm) display pronounced quantum confinement effect and interesting correlations between the size of nanodots and magnetic behaviour [14]. Though the smallest ($\sim$5 nm) nanostructures display superparamagnetic (SPM) behavior, ferromagnetism is observed for the larger nanostructures. The single domain nature of TiO_2 nanostructures is responsible for the observed SPM behavior [14]. These results can have potential for spintronic devices.

Constrained TiO_2 nanostructures fabricated at higher irradiation fluences, 6×10^{17} - 1×10^{19} ions/cm^2, have also been investigated here for their photo- absorption properties [16]. The nanostructures are anisotropic in nature, being elongated along [001] direction. With increasing fluence, the anisotropy of the nanostructures increases. Their width along [$1\bar{1}0$], however is constrained and does not grow proportionally. Angle resolved XPS (ARXPS) results display

development of Ti-rich zones in near-surface regions due to the development of Ti^{3+}, Ti^{0} and other oxygen vacancy related states via preferential sputtering of oxygen atoms during irradiation [16]. Asymmetric diffusion of these mobile species, on the TiO_2(110) surface, play crucial role in defining the nanostructure morphology as well as their photo- absorption properties. Role of ion beam direction upon the nanostructure morphology and subsequent modulation in photo absorption properties have also been investigated. The enhanced photo-absorption response from TiO_2 nanostructures, as observed here, is in absence of any dopant material and displays a decaying exponential dependance on the size of nanostructures along [001], the fast diffusion direction.

We have also investigated the formation of nanostructures on ZnO(0001) single crystals through irradiation with 1.5 keV neutral Ar atom beam [17]. Irradiations were performed at two different incident angles at the fluence of 1.2×10^{17} ions cm^{-2}, leading to the formation of self-assembled crystalline nanostructures of two different sizes. The surface morphology, upon atom beam sputtering, is controlled through competition between the erosive and diffusive processes which leads to the spontaneous formation of nano dimensional patterns on the surface. XPS results from atom beam irradiated ZnO(0001) indicate surface regions to become Zn rich. Preferential sputtering of low mass oxygen atoms has been shown to be responsible for this. ZnO nanostructures, displaying hexagonal ordering and long ranged periodic behavior, also demonstrate higher photo absorption response along with a bandgap reduction of $\sim$0.09 eV. Existence of Zn-rich surface regions and oxygen vacancies, in conjunction with the presence of new crystalline photoactive phases for these nanostructures, become responsible for the enhanced photoabsorption properties and reduced bandgap observed here.

In the last part of the thesis, photo absorption response and resistive switching properties for NiO nanostructures grown by hydrothermal method have been discussed [18]. XPS results indicate the presence of metallic Ni^{0} as well as Ni^{2+} states on these nanoflakes. However, the metallic Ni content varies with reaction time. The nanoflakes grown at the smallest reaction time delineate the highest photo-absorbance response, smallest bandgap as well as low voltage resistive switching behavior. Conducting AFM measurements on NiO nanoflake devices, with gold bottom electrode, have been performed. With the detailed quantitative investigations of the current and voltage (I-V) characteristics, it is observed that the metallic Ni content, in NiO nanostructures, controls the voltages for the formation and rupturing of conducting filaments leading to creation of two stable resistance states i.e. a Low resistance state (LRS) and a High

resistance state (HRS). The studies, presented here, display bi-stable reversible resistive switching characteristics in NiO nanoflakes. With high photo absorption response and demonstrated resistive switching behaviour these NiO nanoflake devices can be important in optoelectronic applications.

Thus in this thesis, the formation of TiO_2, ZnO and NiO nanostructures as well as their properties in relation to UV-Vis photo-absorption, magnetism, resistive switching etc. have been investigated. Nanostructures of TiO_2 and ZnO have been fabricated by low energy irradiation methods and NiO nanoflakes are grown by hydrothermal method. Development of TiO_2 nanostructures lead to the creation of Ti rich zones along with the creation of Ti^{3+} and other vacancy states on the surface. These together contribute to the enhanced photoabsorption response and bandgap modifications observed here in the absence of any dopant element. In addition, at low fluences, highest photo absorbance is displayed, in an anomalous fashion, by 15 nm nanostructures and not the smaller nanostructures due to the competition between the size of nanostructures and the number of vacancy states. Small single domain nanostructures, however, show super-paramagnetic behavior not shown by larger nanostructures which demonstrate ferromagnetic character. Formation of anisotropic TiO_2 nanostructures, which are elongated along [001] direction, is observed at high ion fluences. The results presented here demonstrate that this is regulated by asymmetric diffusion of mobile species, like Ti^{3+}, Ti^0, which are created during ion irradiation of the TiO_2 (110) via the preferential sputtering. Enhanced photoabsorption response, observed here, surprisingly indicates an exponentially decaying dependence on the size of TiO_2 nanostructure along [001] direction, i.e. the fast diffusion direction. Self organised ZnO nanostructures, created by atom beam sputtering technique, display hexagonal closed packed ordering and long ranged periodic behavior. Additionally, presence of vacancy states and development of new crystalline photoactive phases for these nanostructures contribute to the high photo absorbance and narrower bandgap as observed here. NiO nanoflakes have been grown here by hydrothermal method and demonstrate bi-stable reversible resistive switching properties through the formation and rupturing of conducting filaments.

Bibliography

[1] A. Fujishima, and K. Honda, Nature **238**, 37 (1972).

[2] X. Chen, and S. S. Mao, Chem. Rev. **107**, 2891 (2007).

[3] D. Caruntu, G. Caruntu, and C. J. O'Connor, J. Phys. D: Appl. Phys. **40**, 5801 (2007).

[4] J. Zhu, Z. Gui, Y. Ding, Z. Wang, Y. Hu, and M. Zou, J. Phys. Chem. C **111**, 5622 (2007).

[5] S. Majumder, D. Paramanik, V. Solanki, B. P. Bag, and S. Varma, Applied Physics Letters **98**, 053105 (2011).

[6] D. S. Jeong, R. Thomas, R. S. Katiyar, J. F. Scott, H. Kohlstedt, A. Petraru, and C. S. Hwang, Reports on Progress in Physics **75**, 076502 (2012).

[7] S. Facsko, T. Dekorsy, C. Koerdt, C. Trappe, H. Kurz, A. Vogt, and H. L. Hartnagel, Science **285**, 1551 (1999).

[8] U. Valbusa, C. Boragno, and F. B. de Mongeot, J. Phys. Cond. Mat. **14**, 8153 (2002).

[9] R. M. Bradley, and J. M. E. Harper, J. Vac. Sci. Technol. A **6**, 2390 (1988).

[10] M. A. Makeev, R. Cuerno, and A. L. Barabasi, Nucl. Instrum. Methods Phys. Res. B **197**, 185 (2002).

[11] F. Frost, B. Ziberi, T. Hoche, and B. Rauschenbach, Nucl. Instrum. Methods Phys. Res. B **216**, 9 (2003).

[12] V. Solanki, S. Majumder, I. Mishra, P. Dash, C. Singh, D. Kanjilal, and S. Varma, Journal of Applied Physics **115**, 124306 (2014).

[13] Vanaraj Solanki, Subrata Majumder, Indrani Mishra, Shalik R. Joshi, Dinakar Kanjilal, and Shikha Varma, Radiation Effects and Defects in Solids, **168**, 518 (2013).

[14] V. Solanki, I. Mishra, S. R. Joshi, P. Mishra, P. Dash, N. C. Mishra, D. Kanjilal, and Shikha Varma, Nucl. Inst. Meth. Phys. B In press (2015).

[15] Y. Matsumoto, M. Murakami, T. Shono, T. Hasegawa, T. Fukumura, M. Kawasaki, P. Ahmet, T. Chikyow, S. Y. Koshihara, and H. Koinuma, Science **291**, 854 (2001).

[16] Vanaraj Solanki, Shalik Ram Joshi, Indrani Mishra, D. Kanjilal and Shikha Varma, Applied physics Letters, (Under Review).

[17] Vanaraj Solanki, Shalik R. Joshi, Indrani Mishra, D. Kabiraj, N.C. Mishra, D. Avasthi, and Shikha Varma, (to be Submitted).

[18] Vanaraj Solanki, Shalik R. Joshi and Shikha Varma, (to be Submitted).

List of Publications :

1. ***** Enhanced anomalous Photo-absorption from TiO_2 Nanostructures, **Vanaraj Solanki**, Subrata Majumder, I. Mishra, P. Dash, C. Singh, D. Kanjilal, and Shikha Varma, Journal of applied physics 115, 124306 (2014).

2. ***** Size-dependent optical properties of TiO_2 nanostructures, **Vanaraj Solanki**, Subrata Majumder, Indrani Mishra, Shalik R. Joshi, Dinakar Kanjilal, and Shikha Varma, Radiation Effects and Defects in Solids 168, 518 (2013).

3. ***** Room Temperature Superparamagnetism in Rutile TiO_2 Quantum Dots : Produced via ECR Sputtering, **Vanaraj Solanki**, I. Mishra, S. R. Joshi, P. Mishra, P. Dash, N. C. Mishra, D. Kanjilal, and Shikha Varma, Nuclear Instruments and Methods in Physics Research B 365, 82 (2015).

4. ***** Photo-Absorbance Properties of Constrained Nanostructures on rutile TiO_2 (110) surfaces, **Vanaraj Solanki**, Shalik Ram Joshi, Indrani Mishra, D. Kanjilal, and Shikha Varma, Applied physics Letters (Under Review).

5. ***** Enhanced Photo-absorption from ZnO(0001) Nanostructures fabricated by Atom Beam Sputtering, **Vanaraj Solanki**, Shalik R. Joshi, Indrani Mishra, D. Kabiraj, N. C. Mishra, D. K. Avasthi, and Shikha Varma, (to be Submitted).

6. ***** Resistive Switching characteristics and Photo-absorption Properties of Hydrothermally grown NiO nanoflakes, **Vanaraj Solanki**, Shalik R. Joshi, and Shikha Varma, (to be Submitted).

7. ZnO Nanocrystals: Magnetic Study, S. Majumder,**Vanaraj Solanki**, A. Gupta, Shikha Varma, Asian Journal of Physics 19, 269 (2010).

8. Band gap tailoring of rutile TiO_2 (110) via surface patterning with electron cyclotron resonance sputtering, S. Majumder, D. Paramanik, **Vanaraj Solanki**, B. P. Bag, and Shikha Varma, Applied Physics letter 98, 053105 (2011).

9. Formation of Patterns and Scaling Properties of Tantalum Surface after Low Energy Ion Beam Irradiation, S. Majumder, Rama Rao Medicherla, D. Paramanik, **Vanaraj Solanki**, Indrani Mishra, and Shikha Varma, Radiation Effect and Defect in Solid 166, 592 (2011).

10. Ion Irradiation induced nano patterning on TiO_2 Single Crystal by ECR Sputtering, S. Majumder, D. Paramanik, **Vanaraj Solanki**, Indrani Mishra, D. K. Avasthi, D. Kanjilal, and Shikha Varma, Applied Surface Science 258, 4122 (2012).

11. Magnetic Properties of Cu/Ni Bilayer on Si (100) Surface, S. K. Parida, V. R. R. Medicherla, D. K. Mishra, **Vanaraj Solanki**, Shikha Varma, Manoj Kumar Sharma, and Ratnamala Chatterjee, Materials Focus 3, 239 (2014).

12. X-Ray Photoelectron Spectroscopic Study of Bulk $SrTiO_3$, R. R. Mohanta, V. R. R. Medicherla, K. L. Mohanta, N. C. Nayak, **Vanaraj Solanki**, and Shikha Varma, Advanced Science Letters 20, 703 (2014).

13. Comparison of Core Levels of Bulk and Thin Film of $BaTiO_3$, R. R. Mohanta, V. R. R. Medicherla, K. L. Mohanta, N. C. Nayak, **Vanaraj Solanki**, and Shikha Varma, Advanced Science Letters 20, 584 (2014).

14. Ion beam induced Chemical and Morphological changes in TiO_2 films deposited on Si(111) surface by Pulsed Laser Deposition, R. R. Mohanta, V. R. R. Medicherla, K. L.Mohanta, Nimai C. Nayak, S. Majumder, **V. Solanki**, Shikha Varma, Komal Bapna, D. M. Phase, and V. Sathe, Applied surface science 325, 185 (2015).

15. Structural and optical study of MeV Cobalt ion implanted Silicon, Pramita Mishra, **V. Solanki**, Ashutosh Rath, Soumee Chakraborty, Himanshu Lohani, Pratap Kumar Sahoo, Biju Raja Sekhar, Advanced Materials Letters 5, 699 (2014).

16. Effect of thermal annealing on the microstructure and surface morphology of NiO thin film, P. Mallick, B. N. Dash, **Vanaraj Solanki**, Shikha Varma, and N.C. Mishra, Adv. Scie. Enge. Med. 6, 1118 (2014).

17. Low energy ion beam modification of Cu/Ni/Si(100) surface, S. K. Parida, V. R. R. Medicherla, D. K. Mishra, S. Choudhary, **Vanaraj Solanki**, and Shikha Varma, Bulletin of Mat. Science 37, 1569 (2014).

18. Study of thickness dependent sputtering in gold thin films by swift heavy ion irradiation, P. Dash, P. K Sahoo, **V. Solanki**, U. B. Singh, D. K Avasthi, Nuclear Instruments and Methods in Physics Research B In Press (2015).

Conference Proceedings :

1. Reduction of anatase TiO_2 on Si(111) by ion beam sputtering, V. R. R. Medicherla, R. R. Mohanta, K. L. Mohanta, Nimai C. Nayak, S. Choudhary S. Majumder, **Vanaraj Solanki**, Shikha Varma, D. M. Phase, and V. Sathe, AIP Conf. Proc. 1461, 403 (2012).

2. Bandgap Engineering, Enhanced UV-Vis Absorbance and Higher PL Emission from Ion Beam Modified and Nanodot Patterned Rutile TiO_2(110) Surfaces, Subrata Majumder, **Vanaraj Solanki**, Indrani Mishra, Shalik R. Joshi, Dinakar Kanjilal, Shikha Varma.AES-ATEMA 2012 Conference Proceedings pp 131-138, (2012).

***** indicates papers on which this thesis is based

List of Figures

Chapter 1

Introduction

1.1 Introduction :

Nanostructured materials have gained immense attention as they exhibit a variety of fascinating and useful properties with many technological implications. With frontier research in many disciplines getting guided by nanodimensional science and technology, their fundamental understanding and application regimes demand the exciting attention that this field is receiving. For nano-scale ($\sim$1-100 nm) objects the larger active surface area and modified properties, which differ significantly from bulk, control many aspects of their behaviour [1, 2]. Consequently, their synthesis routes and processes gain high significance [3, 4]. The goal is to provide good control on size, shape and composition of nanostructures. In addition, process should be efficient and fast, with low cost for eventual technological applications to be compatible with mass production. With this trend, there is an interest in developing methods for achieving this through the route of self organization process.

A variety of techniques and methods are utilized for fabricating nanoscale structures [2]. These methods are mainly divided into two categories, ”Bottom Up” and ”Top Down” approach. They offer possibilities for designing technologically important structures with desirable characteristics and improved performances [3, 4]. In the bottom-up approach, fabrication of larger and more complex nanostructures is achieved via self-assembly of smaller and simpler building units, like atoms or molecules. In this approach, the source of raw material can be in the form of gas, liquid or solid. On the other hand, top-down approach incorporates the down scaling of an existing system to produce smaller structures. This opens a way for direct patterning of nanoscale structures. Both these approaches have led to a variety of fabrication techniques like chemical vapor deposition, sol-gel, direct oxidation, sputtering, spray pyroly-

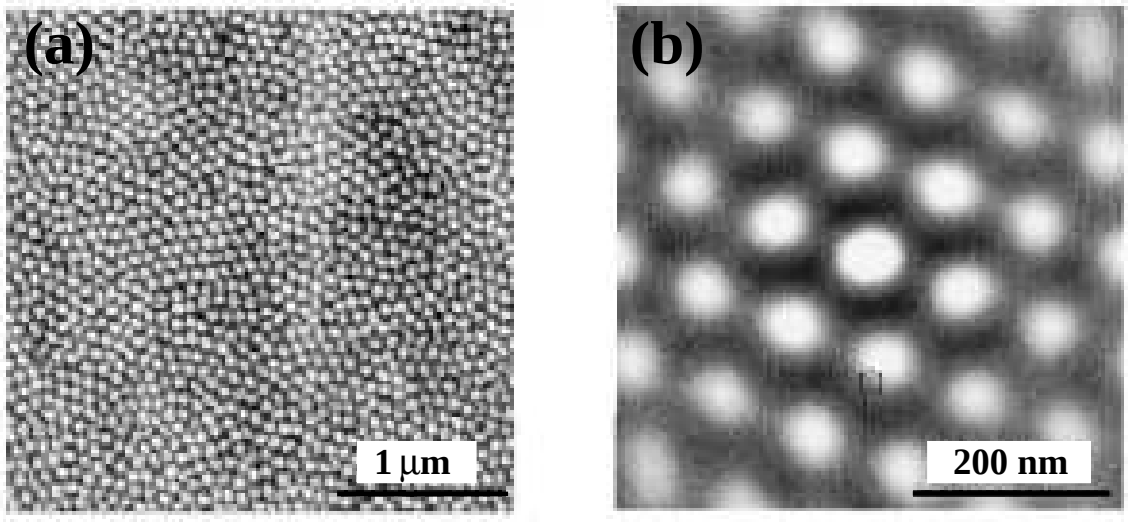

Figure 1.1: (a) Self-organized nanopattern formation on InP(100) after irradiation with 500 eV Ar^+ ion beam at an incident angle of 40°, measured from surface normal (flux=150 μA cm^{-2} and t=9600 sec). Image (b) represents the two-dimensional autocorrelation function calculated from a magnified area of image (a) which clearly shows the hexagonal symmetry of the mound arrangement. (from ref [5])

sis, physical vapor deposition, pulse laser deposition, atomic layer deposition, nanolithography etc. [2–7].

Unique properties of metal oxide nanostructures have attracted enormous interest and are being extensively explored for both their fundamental as well as technological aspects [8–15]. Remarkable applications in photocatalysis [8, 16, 17], photo electrochemical cells [18–20], memory devices [14], and sensors [21, 22] are based on their attractive electronic properties [14, 15]. With many superior properties like chemical stability, high reactivity, biocompatibility, nontoxicity, and good oxidative characteristics, TiO_2, ZnO and NiO are considered important wide band gap semiconductors [6, 13, 23]. Nanosized TiO_2 and ZnO demonstrate many prominent applications in photocatalysis, water splitting, photovoltaic cells, self-cleaning surfaces, dye-sensitized solar cells, environmental remediation etc. [8, 16–20]. NiO nanostructures with characteristic properties like high power density, high energy efficiency and low toxic nature, act as potential candidates for sensors, electrochemical films, battery electrodes, magnetic data storage material, catalyst etc. [10, 12–14].

Ion bombardment of solid surface often produces characteristic surface morphologies which depend on ion beam parameters such as ion fluence, ion energy, incident angle, sample temperature etc. [24–32]. Through this top down approach, well controlled topographies on sub-micron

scale have been achieved on a variety of surfaces of crystalline semiconductors, metals as well as on amorphous and polycrystalline materials [5–7, 24–34]. This method is of special interest because it opens way for the synthesis of a regular array of self organized nanostructures, on large scale, in a single technological step [5–7]. The spontaneous evolution of patterns is a result of competition between curvature dependent erosive processes, that roughen the surface, and diffusive processes that relax or smooth the surface [5–7, 30–32]. The pattern formation on InP(100) after its irradiation with 500 eV Ar^+ ions is shown in fig. 1.1 [5]. Here, the spontaneously developed nanostructures exhibit a hexagonal organization.

Hydrothermal method is a solution phase synthesis technique for producing self organized nanostructures in aqueous solutions via bottom up approach. A variety of other solution phase synthesis processes include sol-gel route, template assisted growth, spray pyrolysis, electrophoresis etc. [35–42]. Hydrothermal growth is a simple and cost effective method. It is an attractive technique as it can synthesize structures at lower temperatures, under slow and controlled conditions. Nanostructures thus produced also display lower defect densities. Unique and metastable crystalline phases of nanostructures, not achievable by usual traditional methods, have also been produced by this technique [43].

In the present thesis, the fabrication and characterization of TiO_2, ZnO and NiO nanostructures have been reported by utilizing a variety of techniques. The nanostructures of these oxide semiconductors display enormous potential for the applications in photo catalysis, photovoltaic cells, spintronics, multiferroics, sensors, magnetic recording media etc. [8–14]. TiO_2 and ZnO nanostructures have been fabricated by utilizing the top-down approach, where sputtering by ion or atom beam irradiation leads to the formation of self assembled nanostructures. NiO nanostructures through bottom-up approach, have been produced by hydrothermal growth method. As the oxide nanostructures are being widely applied in opto-electronics, spintronics, resistive memory etc. applications [8, 14–20], we have also studied their photo-absorption response, magnetic nature as well as resistive switching properties. By controlling the compositional properties, oxidation states, vacancy states and metallic content etc. at nanoscale, during the synthesis process (irradiation or hydrothermal growth), it is possible to design high quality devices with improved predefined performances.

This chapter is organized in following order. Section 1.2 discusses the basics of ion-solid interaction. The sputtering process along with the formation of patterns by ion or atom beam irradiation and their theoretical aspects are discussed in section 1.3. The synthesis of nanos-

tructures with hydrothermal growth method is discussed in section 1.4. Importance of photo-absorption response and resistive switching behaviour, in current research, and their utilization for technological applications is discussed in section 1.5 and 1.6, respectively.

1.2 Basics of Ion-Solid Interaction :

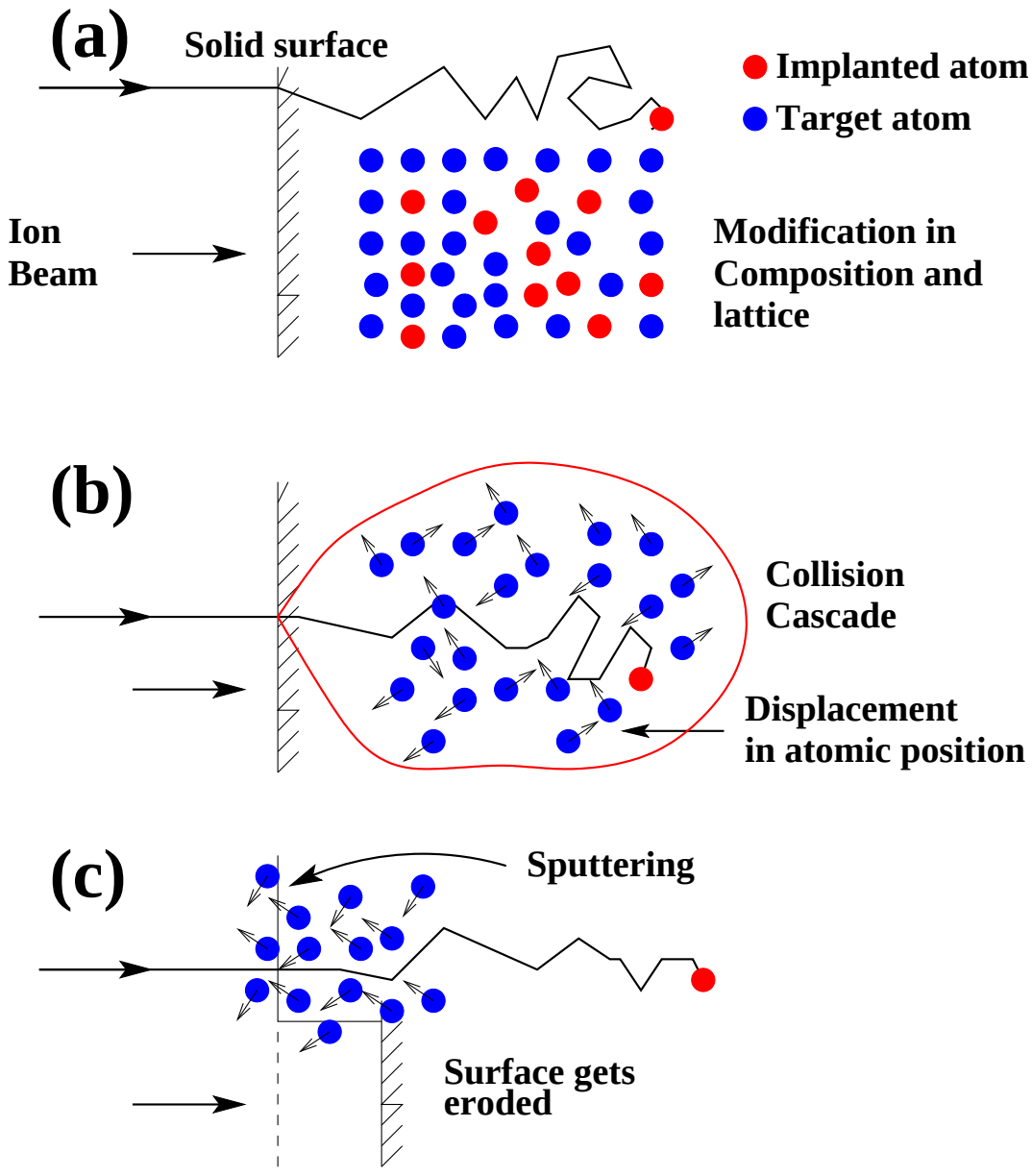

Figure 1.2: Implantation of an Ion (a), Damage in Material after ion implantation (b) and Atomic Sputtering with surface erosion (c) (from ref [44]).

Bombardment of energetic ions on a solid surface significantly influence and modify the

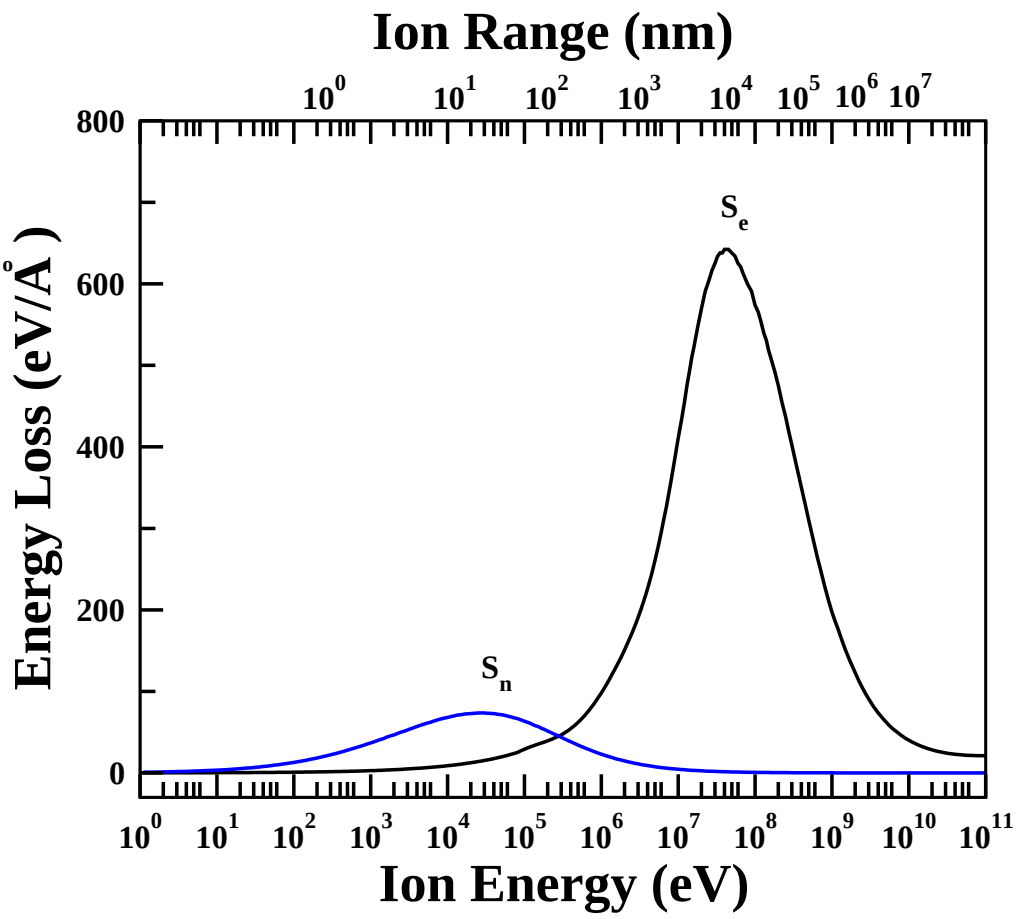

Figure 1.3: Ion range and Energy losses, nuclear S_n, and electronic S_e, as a function of ions kinetic energy, as calculated using the SRIM2012 simulation code [45], for Ar ions in ZnO target.

properties of the material [46]. During irradiation, an energetic ion interacts with atomic electrons, of material, through purely coulombic interaction. This results in an excited or an ionized atom which finally returns to its ground state. Various processes involved in the modification of material, during ion beam irradiation, are shown in fig. 1.2. Figure 1.2(a) displays the process of ion implantation. This builds up a concentration profile of foreign atoms within a solid and alters the composition and lattice structure in the implanted zone. The spatial distribution of the implanted atoms will depend on ion energy and various stopping processes like nuclear and electronic. The process of displacement or collision cascade, as shown in fig. 1.2(b), involve the hard nuclear collisions between incident heavy ion and the target atoms. These heavy ions can displace large number of lattice atoms within the region around the ion trajectory and create considerable structural damage to the material. Figure 1.2(c) shows the process of surface

atom ejection from the target material through nuclear collisions, known as ”sputtering”. This phenomenon leads to surface erosion and sometime also produce the nanostructures via self-assembly. In the case of low energies (keV) ion irradiation, sputtering is a predominant process whereas high energy (MeV) ion bombardment leads to the lattice modifications and deep layer implantation.

Two basic energy transfer mechanisms, nuclear (S_n=$(dE/dx)_n$) and electronic energy loss (S_e = $(dE/dx)_e$) (dE/dx (stopping power) is energy transfer per path length), are involved during energy loss process when energetic ions strike the surface. In the elastic collisions, incident ions colliding with atomic nuclei loose their energy via S_n whereas S_e results from the inelastic excitations and ionizations of the electrons [47]. In both the cases, processes involved in the interactions are Coulomb type. Ion-electron interactions are purely Coulombic whereas screened Coulomb potential play role in nuclear interaction. However, the dominant energy regimes for these processes are different.

For ions with energies of a few keV/amu, the velocity of incident ions is much less than the Bohr velocity of electrons. This provides larger interaction time between projectile and the nucleus. In this energy regime, bombarding ions lose their energy predominantly through nuclear energy loss mechanism. On the other hand, at higher energy of about few MeV/amu, the inelastic electronic energy loss mechanism is dominant in slowing down the incident ions. In this regime, the velocity of projectile and the Bohr velocity of electrons is comparable. Figure 1.3 displays the dominant regions of S_n and S_e for Argon (Ar) ions bombarding the zinc oxide (ZnO) target as a function of ion energy.

1.3 Sputtering Process :

Sputtering is a process whereby atoms are ejected from a solid target material due to energetic particles bombardment. Physical sputtering is driven by the momentum exchange between ions and atoms in the materials by collisions [48]. The secondary collisions sometime also generate recoil atoms. During this process, many atoms do not gain threshold energy and hence do not vacate their regular lattice position. However, atoms located at near surface region gain enough energy to break bonds between them and get sputtered out permanently from their regular lattice site. Although, a large number of target atoms participate in the collision cascade, the magnitude of sputtered atoms is much less. The sputtering yield (S), defined as the mean

number of sputtered target atoms per incident ion, is given by:

$$S = \alpha N \frac{S_n(E)}{E_B} \tag{1.1}$$

Here, N and E_B are the density of target atoms and binding energy of the surface atoms, respectively, whereas α is a material and geometry dependent parameter. The energy loss per unit length, as ion travels in the target is describe by the product $NS_n(E)$. Sputtering yield is very sensitive to different parameters like kinetic energy of the incident ions, surface binding energy of target atoms, surface roughness and the stoichiometry of real surfaces [49]. The bombardment of multi-component target leads to the different sputtering rate of various elemental constituents due to preferential sputtering. In this process the lighter atoms get preferentially sputtered compared to heavier atoms. This drastically changes the surface composition compared to the stoichiometric bulk composition [50,51]. As other processes like radiation induced mass transport, segregation etc. also produce similar effect during sputtering, altering the near surface compositions of target, it is quite difficult to distinguish them from preferential sputtering.

1.3.1 Self-organized Pattern Formation by Ion Beam irradiation :

In 1956, Navez et. al. [52] first time observed the formation of ripple pattern on glass substrates, after bombardment with a 4 keV ion beam of air. Though they could not predict accurate explanation at that time, but tried to correlate it with similar macroscopic phenomena like ripple structures formed by wind over sand bed and in cumulus clouds on a partially sunny day. After more than five decades, the evolution of surface morphology during ion beam sputtering is reasonably well understood. It arises due to competition between erosive process, due to ion beam, and the surface relaxation or smoothening by diffusive processes. In general, the shape and the orientation of the patterns is governed by ion beam incidence angle [30] as well as ion energy, current density, ion fluence, compositions of the target, substrate temperature, presence of impurity, direction dependent sputter yield etc. Anisotropic surface diffusion and Ehrlich-Schwoebel (ES) barrier also play key role in ion induced pattern formation [32–34] near step edges. The impact of these parameters on self-organization of patterns, during low energy ion-beam irradiation, have been investigated by many researchers [24–32,52]. In the last few decades, significant amount of experimental and theoretical works have been undertaken to simulate the self-organization on variety of surfaces like semiconductors, insulators, metals,

polymers etc. via ion bombardment [24–34, 52].

Several models, based on continuum dynamical equation for height of the interface, have been proposed and evaluated numerically to study the morphological evolution of the patterns, on ion beam sputtered surfaces [30, 44, 53–56]. Most of these models are extension of the Bradley and Harper (BH) theory [30] and are based on Sigmund's finding of curvature dependent sputtering yield [57]. Variations in these models incorporate various other physical phenomenon at surface, including redeposition, viscous flow, step edge barrier, anisotropic diffusion, nonlinear effect etc. [32, 54–56].

The ion induced pattern formation is not only fascinating from the fundamental physics point of view but is also important for technological aspects. Pattern formation on binary metal oxides [6, 7, 24] as well as metal surfaces [8–20] show many interesting properties.

1.3.2 Theoretical Aspects of Pattern Formation via Sputtering Technique :

Sigmund's Approch to the curvature dependent sputtering and Bradley-Harper Model

Models, based on continuum dynamical equation for the height of interface, describe the surface at a length scale much larger than the atomic scale. A surface height function, h(x, y, t), describes the solid surface in the laboratory coordinate at time t. In this coordinate x and y axes are parallel to the initial flat surface whereas z-axis is normal to it. Assuming an infinite medium, Sigmund showed that, in low energy regime (few keV/amu) the spatial distribution of average energy, deposited by an incident ion at point O inside an amorphous solid, can be approximated by a Gaussian distribution. The former situation is schematically shown in Fig. 1.4. The average energy deposited at point O, by an incident ion striking at point P′ is given by,

$$E(r) = \frac{\varepsilon}{(2\pi)^{3/2}\sigma\mu^2} exp\left[-\frac{x'^2 + y'^2}{2\mu^2} - \frac{(z'+a)^2}{2\sigma^2} \right] \tag{1.2}$$

where, impact point P′ is origin of the coordinate system r′=(x′, y′, z′). a and ε are ion penetration depth and total deposited energy. Here, z′ is aligned along ion beam direction whereas x′ and y′ are perpendicular to z′. σ and μ are longitudinal and transverse straggling widths of the Gaussian distribution (fig. 1.4). The erosion rate at any point P can be expressed in terms of erosion velocity, ν, and is proportional to the total energy deposited by all incident ions. The normal erosion velocity at point P is given by,

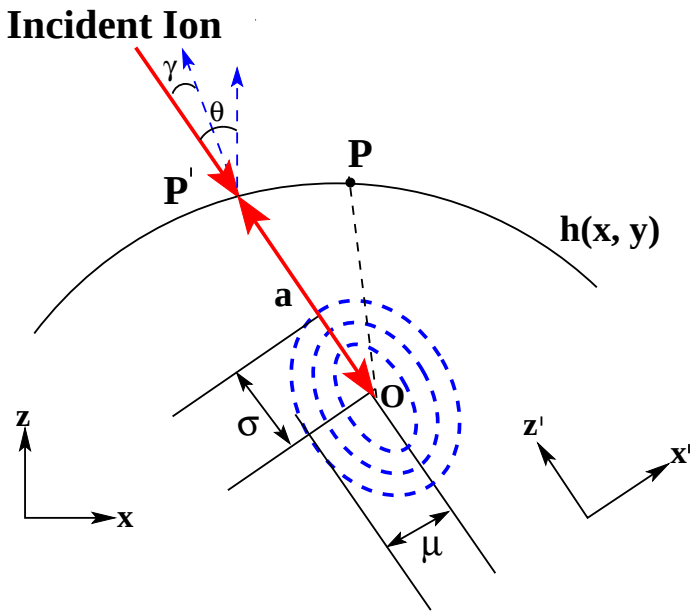

Figure 1.4: Schematic illustration of Gaussian energy deposition by an incoming ion inside a target. θ and γ are global and local angle of incidence, respectively [48].

$$\nu = P \int_{\Re} \phi(r')E(r')dr' \tag{1.3}$$

Here, the integral is taken over region $\Re$ covering impact of all ions which significantly contribute to the total energy deposition. ϕ(r′) is the corrected ion flux due to variation in local slope. γ and θ are local and global incidence angles. The proportionality constant P depends on substrate characteristic and an atomic density, N, given by,

$$P = \frac{3}{4\pi}\frac{1}{NU_OC_O} \tag{1.4}$$

where, U_O and C_O are the surface binding energy and a constant, respectively.

For a slowly varying surface, the radius of curvature, R, at any point is much larger than the depth *a* of mean energy deposition. The height of the surface at any point near point P, in the laboratory coordinate system (x, z), is approximated by,

$$h(x) = -\frac{1}{2}\left(\frac{x^2}{R}\right) \tag{1.5}$$

Combining all above equations with eqn. 1.2, the curvature dependent erosion velocity, $\nu(\theta$, R), for small slope approximation, is approximated by,

$$\nu(\theta, R) \cong \frac{pEfa}{\sqrt{2\pi}\sigma\mu} {B_1}^{-\frac{1}{2}} exp\Big(-\frac{a^2}{2\sigma^2} + \frac{A^2}{2B_1}\Big) \Big[\cos\theta + \Gamma_1(\theta)\frac{a}{R}\Big]. \tag{1.6}$$

Parameters A, B_1, and Γ_1 depend on incidence angle (θ), ion flux, f, a, σ, μ and have been discussed in [30]. In the limit of R=∞, where surface is flat, the sputtering yield is given by $Y_o(\theta)$=N$\nu(\theta, R=\infty)$/fcosθ, where N is the atomic density of solid. Using eq. 1.6 we can write,

$$Y_o(\theta) \cong \frac{pENa}{\sqrt{2\pi}\sigma\mu} {B_1}^{-\frac{1}{2}} exp\Big(-\frac{a^2}{2\sigma^2}\Big) exp\Big(\frac{A^2}{2B_1}\Big) \tag{1.7}$$

For $\sigma > \mu$, A and B_1 are increasing function of incident angle (θ); thus $Y_o(\theta)$ is also an increasing function of θ up to critical angle θ_c. For $\theta > \theta_C$, the sputtering yield decreases when reflection of ions becomes important. From 1.6 and 1.7 one can write

$$\nu(\theta, R) \cong \frac{f}{N} Y_o(\theta) \Big[\cos\theta + \Gamma_1(\theta)\frac{a}{R}\Big] \tag{1.8}$$

The term $\Gamma_1(\theta)$a/R depends on curvature dependent erosion velocity. At normal incidence, $\Gamma_1(\theta)$ is negative, whereas radius of curvature R is negative in a trough and positive at a crest. Figure 1.5, shows ion irradiation processes at trough (Concave) and crest (Convex) region of the surface. According to eq. 1.8, the deposited energy density at point G for the ions striking at A is larger than the energy deposited at G$'$ due to the ions striking at A$'$, since G$'$A$' >$ GA. Hence, trough gets eroded faster than the crest region. This difference in erosion rate creates surface instability. The alternative smoothening processes help to overcome instability generated by roughening process. The competition between these processes finally stabilizes the surface with formation of periodically modulated structures like ripples, dots, etc. The B-H model predicts formation of parallel mode ripples (with wave vector, $\hat{k}$ being parallel to ion beam direction) for $\theta < \theta_C$, and perpendicular mode ripples (with $\hat{k}$ being perpendicular to ion beam direction) at grazing incidence geometry [30].

Finally, the equation of motion for slowly varying surface is better described as the height modulation h(x, y, t) of the eroding surface and is given by,

$$\frac{\partial h}{\partial t} \cong -\nu_o + \nu\nabla^2 h - D\nabla^4 h \tag{1.9}$$

where ν_o, ν and D are constant erosion velocity, effective negative surface tension and surface diffusion coefficient, respectively. The realistic solution of eq. 1.9 predicts an exponential growth of surface with fluence, along with a characteristic wavelength. Wavelength of this

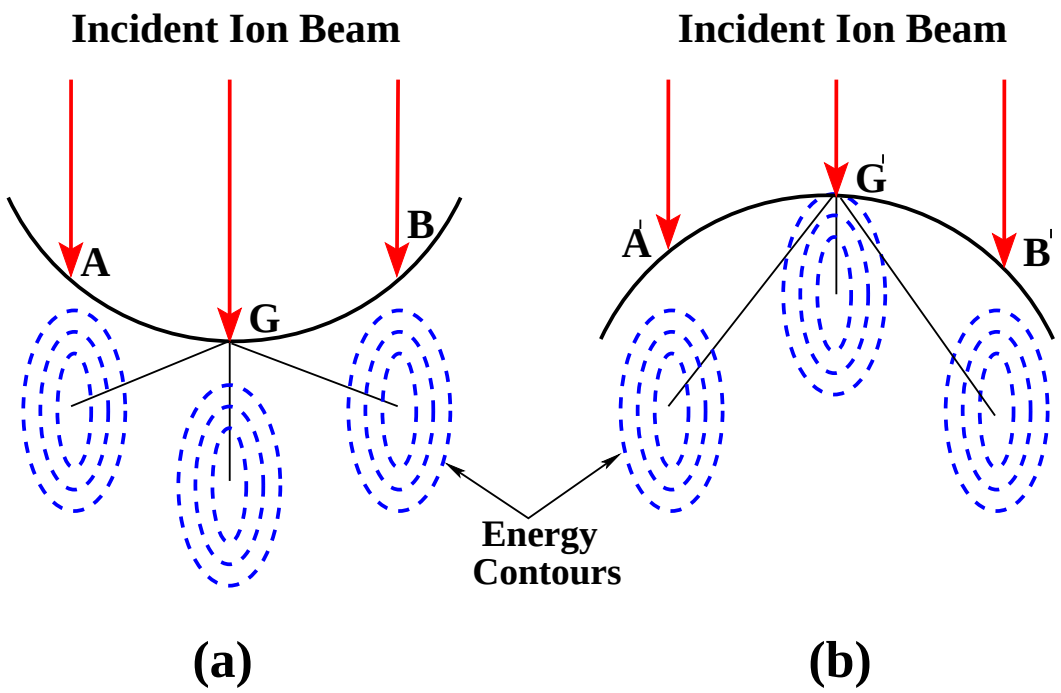

Figure 1.5: Schematic illustration of Gaussian energy deposition profiles, for (a) concave and (b) convex surfaces, by incident energetic ion. The energy deposited at G is larger than at G′, since G′A′>GA [48].

growth is independent of the ion fluence. But in many cases, sputtering vary in different ways and the generated surface morphologies are not unique for different substrates. To overcome this, in 1995, Cuerno and Barabasi (CB) [58] developed a model to describe the ion induced pattern morphology in early time regime of BH model. The later time dynamics is dominated by the nonlinear term proposed by Kuramoto-Tsuzuki [59]. Taking care of the nonlinear effects, the revised characteristic equation, describing the surface evolution, is given by:

$$\frac{\partial h}{\partial t} \cong -\nu_o + \nu\nabla^2 h - D\nabla^4 h + \frac{\lambda}{2}(D\nabla h)^2 + \eta \tag{1.10}$$

where the term η represents the uncorrelated noise with zero mean, i.e. the randomness resulting from the stochastic nature of the incident ions striking the surface. The term $\frac{\lambda}{2}(D\nabla h)^2$ accounts for the slope dependent erosion yield. This eventually stabilize the surface by saturation of the surface roughness with time [60–62].

Anisotropic surface diffusion and Ehrlich-Schwoebel barrier

The pattern formation on anisotropic metal and metal oxide surfaces is more complex than amorphous surfaces due to higher and anisotropic diffusivity of metal adatoms [32]. In this case, the build-up of a regular pattern is produced by surface instability caused by the surface curvature dependent sputtering and the presence of an extra barrier at step edge (ES barrier). This barrier is seen by the diffusing adatom while trying to descend the step edge [32, 63–66]. Equations 1.9 and 1.10 do not explain the pattern formation for metals, since the contribution of the diffusive term $D\nabla^4 h$ is oversimplified. To address this issue a different diffusion term for each principal surface direction is added and discussed in [64]. It is assumed that these terms depend exponentially on temperature. A corrected characteristic equation for surface evolution is written as,

$$\frac{\partial h}{\partial t} \cong -\nu_o + \nu\nabla^2 h - \left(D_{\vec{n}}\nabla^4_{\vec{n}} h - S_{\vec{n}}\nabla^2_{\vec{n}} h\right) + \eta \tag{1.11}$$

Here, the terms $D_{\vec{n}}\nabla^4_{\vec{n}} h$ and $S_{\vec{n}}\nabla^2_{\vec{n}} h$ account for the diffusion along $\vec{n}$ crystallographic orientation and diffusion arising from the Ehrlich-Schwoebel barrier, respectively [66].

1.4 Nanostructuring by Hydrothermal Growth :

Simple and cost effective hydrothermal technique producing self-organized nanostructures, via bottom-up approach, falls in the class of solution phase synthesis method. Most of the solution based synthesis methods utilize the supercritical properties of water, i.e. combination of liquid and gas phase, at elevated temperature and pressure above its boiling point [67]. When water is used as a solvent, the method is referred to as “hydrothermal”. In comparison to other solution based methods, this method requires much lower temperature and pressure for the growth of nanomaterials. Other properties of water like viscosity, solvation, dielectric, etc. are extremely sensitive to the pressure and temperature, and hence even small variation in these parameters greatly affect the kinetics of chemical reactions [67]. The low dielectric constant of water causes low solubility of compounds so sometimes additional mineralizer solutions like fluorides, chlorides, hydroxides, carbonates etc. are required to enhance the solubility of the starting material [67].

Hydrothermal method has been widely used for the synthesis of nanostructures of desired dimension with variety of shapes like nanowires, nanorods, nanocombs, nanorings, nanoloops

and nanohelices, nanobows, nanobelts, nanoflakes and nanocages [68–74] etc. Synthesis of elemental nanostructures, like Carbon, Si, Ge [75–77], and nanostructures of compound semiconductors, like InP, GaAs, ZnO, TiO_2, NiO [10, 78–84] by this method have also been earlier reported. The hydrothermal growth method is an advantageous technique due to the relatively low crystallization temperature, controllable reaction conditions, low growth rates, formation of high optical quality metastable and unique phases, not easily attainable by traditional methods. In addition, several other controllable reaction parameters like cooling rate, pressure, mineralizer solution, length of reaction, and stoichiometry of reactant also provide better control on optimization of good quality nano crystal growth [67, 85]. These nano crystals have relatively less thermal strain and defect density compared to other NS, grown by traditional methods, which is important for designing and synthesis of new materials for many applications.

1.5 Photo-absorption behaviour :

The photovoltaic effect refers to the creation of an electromotive force through the utilization of radiation or photons and the performance of such devices depend on the photon absorption and photo carrier collection. For converting the radiation into electricity, the first step is the generation of an electron hole pair. The energy of a photon is absorbed by an electron that is excited from the valence band to the conduction band. A positively charged hole is left behind in the process. During a recombination process, both the carriers will annihilate each other by electrons occupying the empty state of the hole. Both the carriers disappear in this process. For efficient trapping of the light it is necessary to absorb the maximum amount of radiation from a large part of the desired spectrum and to reduce the recombination of the charge carriers.

Nanostructures have gained tremendous attention in the field of photovoltaics as they demonstrate enhanced light trapping characteristics along with high carrier collection efficiency [86, 87]. Metal oxide nano structures also display potential as a superior candidate for photocatalytic and photovoltaic applications [88]. These are also excellent materials with many other desirable properties like their utilization in energy sources and in environmental areas. However, they usually posses large band gap which dominate light absorption in UV region. Hence, investigating their absorbance of visible light spectrum, and enhancing it, becomes critical in order to facilitate application of these systems in the fields of photovoltaics and visible light photocatalysis. Dye sensitization and band gap tailoring by doping are some techniques fre-

quently utilized for achieving the absorbance in long wavelength regimes. For the first, there are several inherent problems associated due to the instability of the organic complex and the change of selectivity of host semiconductor. During bandgap tailoring by doping, the performance of various transition metal dopants is limited by thermal instability and increase of carrier recombination centers [89]. Incorporation for anionic nonmetal dopants like nitrogen(N) and carbon(C) have also been investigated for extension of photovoltaic activity for visible light [90]. These dopants are also sometimes unsuitable for photocatalyst and photochemical material, because the dopant related isolated bandgap states can act as recombination centers of carriers [90].

1.6 Resistive Switching behaviour :

Resitive RAM (ReRAM) devices based on as manganates, titanates, and zirconates have been explored for some decades now [91–96]. However, in recent years Resistive RAM devices based on Transition metal oxides (TMO) have attracted lot of attention as a candidate for future computer memories. This is due to their potential of a low power consumption conjugated with fast switching speeds and good scalability. A typical device consists of an active layer (or layers) of TMO within two electrodes. By the application of an electric field, the active layer can be driven to exist in two resistive states namely, a High restive state (HRS) and a Low resistive state (LRS). This switching happens by the virtue of the electroforming that leads to formation of some conducting filament (CF) paths between the two electrodes.

With nano-dimensional switching elements technically and theoretically possible, high density ReRAM devices are being actively explored [97,98]. These investigation, however, are still in developmental stages due to many intricacies. Primarily, the mechanisms behind switching behaviour, which are related to CF formation, are complicated and not fully understood. The switching process is inherently governed by the redox processes that take place in the active layer, when an electric field is applied [99, 100]. During this redox (reduction and oxidation) process, oxygen ions and oxygen vacancies will migrate towards anode and cathode, respectively, in n-type semiconductor. On the other hand, oxygen vacancies and cation vacancies migrate towards cathode and anode, respectively, in p-type semiconductor. Depending on the mobile species (oxygen ions, oxygen vacancies, or metal atoms) present, their movement alters the local charge balance, concentration as well as the resistivity nature of the oxide layer. These

processes reflect the main premise of *resistive switching* (RS) behaviour in oxides. Investigations of spatially resolved conductivity, along with structural and compositional behaviour, are necessary for understanding the issues related to switching mechanisms. However there are only few investigations in this regard [101, 102]. Moreover for exceptional performance and efficient scaling-down of these devices, it becomes necessary that RS phenomena are confined to nano-dimensions [103, 104].

The organization of present thesis is as follows. Chapter 2 discusses the various experimental techniques that have been utilized in this thesis. Chapter 3 deals with the fabrication of nanostructures on rutile TiO_2 (110) single crystals by ion irradiation method. The surface morphology, core level photoelectron emission, optical absorption and photoluminescence response of the patterned surfaces have also been investigated. Magnetic properties of TiO_2 nanostructures have been presented in chapter 4. Single and multi domain nature of these nanostructures and their superparamagnetic and ferromagnetic properties are reported. Chapter 5 discusses the formation of constrained nanostructures on rutile TiO_2 (110) single crystals at higher irradiation fluences. The dependency of photo absorption response on the anisotropic size of nanostructures is also presented. Fabrication of nanostructures on wurtzite ZnO (0001) single crystals by atom beam sputtering technique have been discussed in chapter 6. Morphological evolution, core level photoelectron emission and optical absorption response of nanostructured surfaces have also been presented. Chapter 7 discusses the growth of NiO nanostructures by hydrothermal growth method. The photo absorption and resistive switching properties of NiO nanostructures have been discussed. The conclusions are presented in Chapter 8.

Bibliography

[1] A. D. Maynard, R. J. Aitken, T. Butz, V. Colvin, K. Donaldson, G. Oberdorster, M. A. Philbert, J. Ryan, A. Seaton, V. Stone, S. S. Tinkle, L. Tran, N. J. Walker, and D. Warheit, Nature **444**, 267 (2006).

[2] D. Caruntu, G. Caruntu, and C. J. OConnor, J. Phys. D: Appl. Phys. **40**, 5801 (2007).

[3] G. M. Whitesides, and B. Grzybowski, Science **295**, 2418 (2002).

[4] K. K. Nanda, and S. N. Sahu, Appl. Phys. Lett. **79**, 2743 (2001).

[5] F. Frost, A. Schindler, and F. Bigl, Phys. Rev. Lett. **85**, 4116 (2000).

[6] S. Majumder, D. Paramanik, V. Solanki, B. P. Bag, and S. Varma, Appl. Phys. Lett. **98**, 053105 (2011).

[7] V. Solanki, S. Majumder, I. Mishra, P. Dash, C. Singh, D. Kanjilal, and S. Varma, J. Appl. Phys. **115**, 124306 (2014).

[8] A. Fujishima, and K. Honda, Nature **238**, 37 (1972).

[9] Y. Matsumoto, M. Murakami, T. Shono, T. Hasegawa, T. Fukumura, M. Kawasaki, P. Ahmet, T. Chikyow, S. Koshihara, and H. Koinuma, Science **291**, 854 (2001).

[10] Z. L. Wang, J. Phys.: Cond. Mat. **16**, R829 (2004).

[11] P. V. Kamat, R. Huehn, and R. Nicolaescu, J. Phys. Chem. B **106**, 788794 (2002).

[12] K. Jung, J. Choi, Y. Kim, H. Im, S. Seo, R. Jung, D. Kim, J. S. Kim, B. H. Park, and J. P. Hong, J. Appl. Phys. **103**, 034504 (2008).

[13] F. Nardi, D. Deleruyelle, S. Spiga, C. Muller, B. Bouteille, and D. Ielmini, J. Appl. Phys. **112**, 064310 (2012).

[14] D. S. Jeong, R. Thomas, R. S. Katiyar, J. F. Scott, H. Kohlstedt, A. Petraru, and C. S. Hwang, Rep. Prog. in Phys. **75**, 076502 (2012).

[15] X. Chen, and S. S. Mao, Chem. Rev. **107**, 2891 (2007).

[16] D. Li, and H. Haneda, Chemosphere **51**, 129 (2003).

[17] M. Qamar, and M. Muneer, Desalination **249**, 535 (2009).

[18] K. S. Ahn, Y. Yan, S. Shet, K. Jones, T. Deutsch, J. Turner, and M. Al-Jassim, Appl. Phys. Lett. **93**, 163117 (2008).

[19] Q. Yu, and C. Cao, J. Nanosci. Nanotech. **12**, (5):3984 2012.

[20] F. Decker, J. F. Juli, and M. Abramovich, Appl. Phys. Lett. **35**, 397 (1979).

[21] B. Karunagaran, P. Uthirakumar, S.J. Chung, S. Velumani, and E.K. Suh, Materials Characterization **58**, 680 (2007).

[22] Q. Qi, T. Zhang, Q. Yu, R. Wang, Y. Zeng, L. Liu, and H. Yang, Sens. and Actu. B **133**, 638 (2008).

[23] J. Zhu, Z. Gui, Y. Ding, Z. Wang, Y. Hu, and M. Zou, J. Phys. Chem. C **111**, 5622 (2007)

[24] S. Facsko, T. Dekorsy, C. Koerdt, C. Trappe, H. Kurz, A. Vogt, and H.L. Hartnagel, Science **285**, 1551 (1999).

[25] A. Keller, S. Rossbach, S. Facsko, and W. Mller, Nanotechnology **19**, 135303 (2008).

[26] F. Frost, and R. Rauschenbach, Appl. Phys. A **77**, 1 (2003).

[27] R. Gago, L. Vzquez, R. Cuerno, M. Varela, C. Ballesteros, and J. Albella, Nanotechnology **13**, 304 (2002).

[28] B. Ziberi, F. Frost, T. Hoche, and B. Rauschenbach, Vacuum **81**, 155 (2006).

[29] T. Basu, J. R. Mohanty, and T. Som, Appl. Surf. Sci. **258**, 9944 (2012).

[30] R. M. Bradley, and J. M. E. Harper, J. Vac. Sci. Technol. A **6**, 2390 (1988).

[31] A. R. Cubero, R. Gago, F. Palomares, A. Mucklich, M. Vinnichenko, and L. Vazquez, Phys. Rev. B **86**, 085436 (2012).

[32] U. Valbusa, C. Boragno, and F. B.de Mongeot, J. Phys.: Cond. Matt. **14**, 8153 (2002).

[33] H. B. Huntington, and G. A. Sullivan, Phys. Rev. Lett. **14**, 177 (1965).

[34] M. Kolmer, A. A. Zebari, M. Goryl, F. B. de Mongeot, F. Zasada, W. Piskorz, P. Pietrzyk, Z. Sojka, F. Krok, and M. Szymonski, Phys. Rev. B **88**, 195427 (2013).

[35] L. Spanhel, J. SolGel Sci. Technol. **39**, 7 (2006).

[36] X. Ma, H. Zhang, Y. Ji, J. Xu, and D. Yang, Mater. Lett. **59**, 3393 (2005).

[37] M. Kohls, M. Bonnani, and L. Spanhel, Appl. Phys. Lett. **81**, 3858 (2002).

[38] H. Y. Xu, H. Wang, Y. C. Zhang, S. Wang, M. Zhu, and H. Yan, Cryst. Res. Technol. **38**, 429 (2003).

[39] S. Shingubara, J. Nanoparticle Res. **5**, 17 (2003).

[40] M. Krunks, and E. MellikovE, Thin Solid Films **270**, 33 (1995).

[41] R. Ayouchi, F. Martin, D. Leinen, and J. R. Ramos Barrado, J. Cryst. Growth **247**, 497 (2003).

[42] Y. C. Wan, I. C. Leu, Y. W. Chung, and M. H. Hon, Nanotechnology **17**, 4445 (2006).

[43] X. Xia, Y. Zhang, D. Chao, C. Guan, Y. Zhang, L. Li, X. Ge, I. M. Bacho, J. Tu, and H. J. Fan, Nanoscale **6**, 5008 (2014).

[44] M. A. Makeev, R. Cuerno, and A. L. Barabsi, Nucl. Instr. Meth. Phys. Res. B **197**, 185 (2002).

[45] J. P. Biersack, and L. G. Haggmark, The Transport and Ranges in Matter. Nucl Instrum.Meth **174**, 257 (1980), Available from www.srim.org.

[46] L. C. Feldman, J. W. Mayer, and S. T. Picraux In: Material Analysis By Ion Channeling, Academic Press, New York, p. 1.1 (1982).

[47] U. Littmark, and J. F. Ziegler, Handbook of Range Distributions for Energetic Ions in All Elements, Vol. 6, Pergamon Press, New York (1980); J. F. Ziegler, Handbook of Stopping Cross Sections for Energetic Ions in All Elements, Pergamon Press, 1980; and

J. F. Ziegler, J. P. Biersack, U. Littmark, Proceedings of the US-Japan Seminar on Charged Particle Penetration Phenomena, ORNL report CONF820131 (1982), p.88.

[48] P. Sigmund, Nucl. Instr. Meth. Phys. Res. B **27**, 1 (1987).

[49] P. Sigmund, Ion Sputtering by Particle Bombardment, I, R. Behrisch, ed. (Springer- Verlag: Berlin (1981)).

[50] Z.L. Liau, J.W. Mayer, W.L. Brown, and J.M. Poate, J. Appl. Phys. **49**, 5295 (1978).

[51] H. H. Andersen, and H. L. Bay, J. Appl. Phys. **46**, 2416 (1975).

[52] M. Navez, C. Sella, and D. Chaperot, C. R. Acad. Sci. Paris **254**, 240 (1962).

[53] M. Castro, R. Cuerno, L. Vzquez, and R. Gago, Phys. Rev. Lett. **94**, 016102 (2005).

[54] A. D. Brown, J. Erlebacher, W. L. Chan, and E. Chason, Phys. Rev. Lett. **95**, 056101 (2005).

[55] D. A. Pearson, and R. M. Bradley, J. Phys.: Cond. Matt. **27**, 015010 (2015).

[56] Q. Wei, J. Lian, L. Boatner, L. Wang, and R. Ewing, Phys. Rev. B **80**, 085413 (2009).

[57] P. Sigmund, J. Mat. Sci. **8**, 1545 (1973).

[58] R. Cuerno, and A. L. Barabasi, Phys. Rev. Lett. **74**, 4746 (1995).

[59] Y. Kuramoto, and T. Tsuzuki, Prog. Theor. Phys. **55**, 356 (1976).

[60] R. Cuerno, H. A. Makse, S. Tomassone, S. T. Harrington, and H. E. Stanley, Phys. Rev. Lett. **75**, 4464 (1995).

[61] M. Rost, and J. Krug, Phys. Rev. Lett. **75**, 3894 (1995).

[62] S. Park, B. Kahng, H. Jeong, and A. L. Barabasi, Phys. Rev. Lett. **83**, 3486 (1999).

[63] T. Luttrell, and M. Batzill, Phys. Rev. B **82**, 035408 (2010).

[64] E. A. Eklund, E. J. Snyder, and W. R. Stanley, Surf. Sci. **285**, 157 (1993).

[65] G. Costantini, S. Rusponi, F. B. de Mongeot, C. Boragno, and U. Valbusa, J. Phys.: Cond. Matt. **13**, 5875 (2001).

[66] P. Politi, and J. Villain, Phys. Rev. B **54,** 5114 (1996).

[67] K. Byrappa, and M. Yoshimura, Handbook of Hydrothermal Technology. Elsevier Science: (2008).

[68] S. Baruah, C. Thanachayanont, and J. Dutta, Sci. Technol. Adv. Mater. **9**, 025009 (2008).

[69] Y. Huang, Y. Zhang, X. Bai, J. He, J. Liu, and X. Zhang, J. Nanosci. Nanotechnol. **6**, 2566 (2006).

[70] W. L. Hughes, and Z. L. Wang, Appl. Phys. Lett. **86**, 043106 (2005).

[71] X. Y. Kong, and Z. L. Wang, Nano Lett. **3**, 1625 (2003).

[72] W. L. Hughes, and Z. L. Wang, J. Am. Chem. Soc. **126**, 6703 (2004).

[73] T. Sun, J. Qiu, and C. Liang, J. Phys. Chem. C **112**, 715 (2008).

[74] M. Snure, and A. Tiwari, J. Nanosci. Nanotechnol. **7**, 485 (2007).

[75] S. Iijima, Nature **354**, 56 (1991).

[76] Y. Cui, L. J. Lauhon, and M. S. Gudiksen, Appl. Phys. Lett. **78**, 2214 (2001).

[77] G. M. Burghard, G. T. Kim, G. S. Dusberg, P. W. Chiu, V. Krstic, S. Roth, and W. Q. Han, J. Appl. Phys. **90**, 5747 (2001).

[78] X. Duan, Y. Huang, Y. Cui, J. Wang, and C. M. Lieber, Nature **409**, 66 (2001).

[79] Z. G. Bai, D. P. Yu, H. Z. Zhang, Y. Ding, S. Q. Gai, X. Z. Hang, Q. L. Hiong, and G. C. Feng, Chem. Phys. Lett. **303**, 311 (1999).

[80] M. H. Huang, Y. Wu, H. Feick, N. Tran, E. Webe, and P. Yang, Adv. Mater. **13**, 113 (2001).

[81] M. H. Huang. S. Mao, H. Feick, H. Yan, Y. Wu, H. Kind, E. Weber, R. Russo, and P. Yang, Science **292**, 1897 (2001).

[82] G. Shi, C. M. Mo, W. L. Cai, and L. D. Zhang, Sol. Sta. Comm. **115**, 253 (2005).

[83] Y. Lia, M. Guoa, M. Zhanga, and X. Wang, Mat. Res. Bull. **44**, 1232 (2009).

[84] P. Justin, S. K. Meher, and G. R. Rao, J. Phys. Chem. C **114**, 5203 (2010).

[85] R. A. Laudise, Chem. Eng. News **65**, 30 (1987).

[86] R. Yu, Q. Lin, S. F. Leung, and Z. Fan, Nano Energy **1**, 57 (2012).

[87] E. C. Garnett, and P. D. Yang, Nano Lett. **10**, 1082 (2010).

[88] A. Fujishima, T. N. Rao, and D. A. Tryk, J. Photochem. Photobiol. C **1**, 1 (2000).

[89] W. Choi, A. Termin, and M. R. Hoffmann, J. Phys. Chem. **98**, 13669 (1994).

[90] J.Y. Lee, J. Park, and J. H. Cho, Appl. Phys. Lett. **87**, 011904 (2005).

[91] A. Asamitsu, Y. Tomioka, H. Kuwahara, and Y. Tokura, Nature **388**, 50 (1997).

[92] H. Oshima, K. Miyano, Y. Konishi, M. Kawasaki, and Y. Tokura, Appl. Phys. Lett. **75**, 1473 (1999).

[93] Y. B. Nian, J. Strozier, N. J. Wu, X. Chen, and A. Ignatiev, Phys. Rev. Lett. **98**, 146403/1 (2007).

[94] M. Quintero, P. Levy, A. G. Leyva, and M. J. Rozenberg, Phys. Rev. Lett. **98**, 116601/1 (2007).

[95] Y. Watanabe, J. G. Bednorz, A. Bietsch, Gerber Ch, D. Widmer, A. Beck, and S. J. Wind, Appl. Phys. Lett. **78**, 3738 (2001).

[96] A. Beck, J. G. Bednorz, C. Gerber, C. Rossel, and D. Widmer, Appl. Phys. Lett. **77**, 139 (2000).

[97] K. Szot, W. Speier, G. Bihlmayer, and R. Waser, Nat. Mater. **5**, 312, (2006).

[98] K. Szot, R. Dittmann, W. Speier, and R. Waser, Phys. Sta. Sol. Rap. Res. Lett. **1**, R86 (2007).

[99] M. Janousch, G. I. Meijer, U. Staub, B. Delley, S. F. Karg, and B. P. Andreasson, Adv. Materials **19**, 2232 (2007).

[100] B. P. Andreasson, M. Janousch, U. Staub, and I. G. Meijer, Appl. Phys. Lett. **94**, 13513 (2009).

[101] C. Rossel, G. I. Meijer, D. Bremaud, and D. Widmer, J. Appl. Phys. **90**, 2892 (2001).

[102] F. Miao, J. J. Yang, J. P. Strachan, D. Stewart, R. S. Williams, and C. N. Lau, Appl. Phys. Lett. **95**, 113503 (2009).

[103] S. Hong, T. Choi, J. H. Jeon, Y. Kim, H. Lee, H. Y. Joo, I. Hwang, J. S. Kim, S. O. Kang, S. V. Kalinin, and B. H. Park, Adv Mater. **25**, 2339 (2013).

[104] K. Nagashima, T. Yanagida, K. Oka, M. Kanai, A. Klamchuen, J. S. Kim, B. H. Park, and T. Kawai, Nano Lett. **11**, 2114 (2011).

Chapter 2

Experimental Techniques

The present chapter discusses the experimental techniques related to the fabrication and investigations of nanostructures of TiO_2, ZnO and NiO. These metal oxides, with wide band gap, are semiconducting in nature and their nanostructures display many interesting properties and applications. The nanostructures have been prepared by a variety of routes. The techniques of ion irradiation and atom beam sputtering have been applied for obtaining TiO_2 and ZnO nanostructures, respectively. Hydothermal growth methods have been utilized for preparing NiO nanostructures. The nanostructures, here, have been investigated by many techniques like Scanning Probe Microscopy (SPM), X-ray Photoelectron Spectroscopy (XPS), UV-Vis Spectroscopy (UV-Vis), Photoluminescence (PL), Superconducting Quantum Interference Device (SQUID), Field Emission Scanning Electron Microscopy (FESEM), Transmission Electron Microscopy (TEM) etc. In this chapter, various fabrication and growth facilities, methods and characterization techniques, applied in this thesis, have been discussed.

Section 2.1 discusses various growth methods. In section 2.2 characterization techniques are presented. Crystal structures of TiO_2, ZnO and NiO are discussed in section 2.3.

2.1 Techniques for Fabrication of Nanostructures:

2.1.1 Ion beam Irradiations and Atom Beam Sputtering :

In the present thesis TiO_2 nanostructures have been fabricated by utilizing the Electron Cyclotron Resonance (ECR) based Low Energy Ion Beam Facility (LEIBF) at Inter University Accelerator Centre (IUAC), New Delhi. In the following, the ECR facility and some beam line components are discussed.

Ion Beam Irradiation with ECR source :

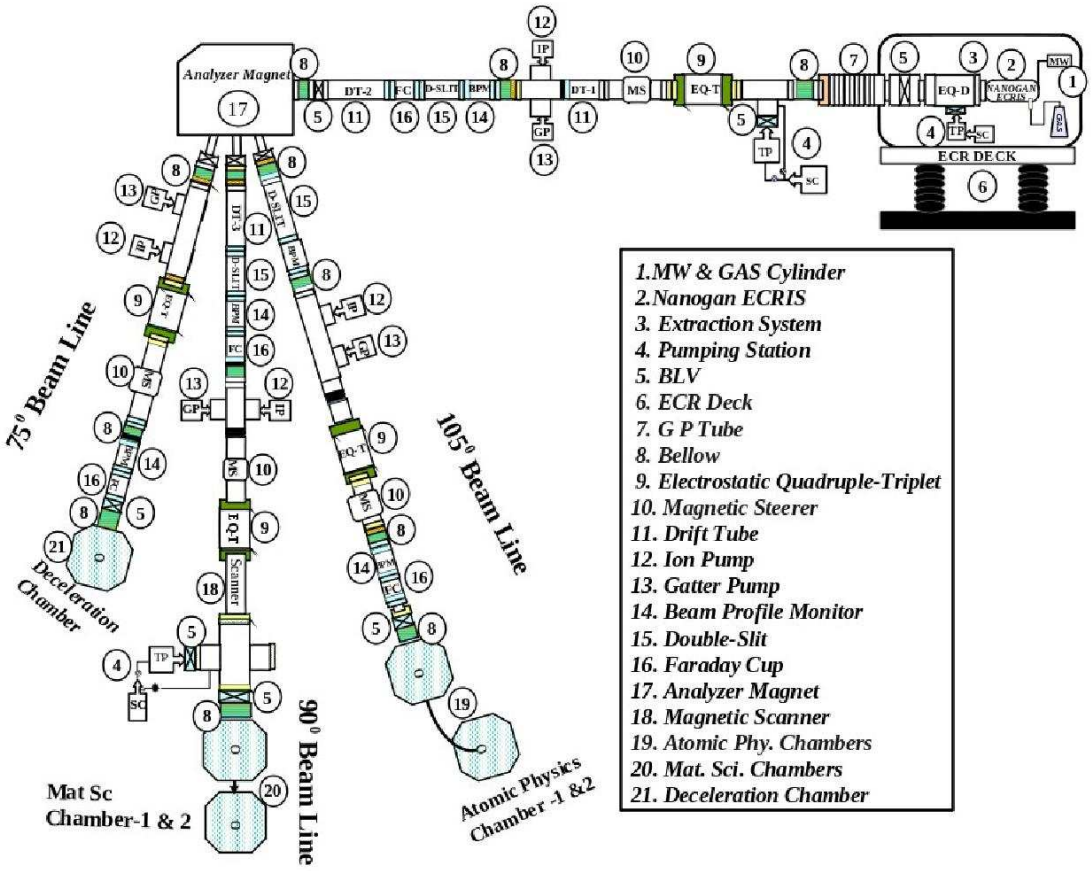

Figure 2.1: Schematic diagram of ECR ion source based LEIBF facility at IUAC, New Delhi [1]. [with permission]

Fig. 2.1 shows the schematic diagram of LEIBF facility. The facility is equipped with a Nanogan type ECR ion source (from Panteknik, France). This ion source is based on a fully permanent magnet (NdFeB) which is designed for radial and axial confinement of the plasma. The principles of ECR ion source operation have been discussed by Geller [2] and Drentje [3]. All peripheral electronics (10 GHz (200 W) ultrahigh frequency transmitter, power supplies and vacuum components together with ECR ion source are installed on a 400 kV HV platform. The high current of multiply charged positive ions, with energy varying, from few tens of keV to few MeV, can be extracted from this ion source.

Ion source, magnetic mass analyzer and accelerating unit are integral parts of the ion im-

planter or low energy ion beam accelerator. A conventional implanter produces a beam of positively charged ions from plasma, created by ionization of injected gas molecules. Ions are produced inside 10 GHz ECR source. These are extracted under high vacuum (pressure $< 10^{-5}$ mbar) by applying an electrostatic field. All components (high frequency transmitter and gas cylinder (1), Nanogan ECRIS (2), and extraction system (3)) of the implanter are placed on a high voltage deck (6) and controlled using optical fiber communication. High vacuum, of $\sim 10^{-6}$ mbar, is maintained inside the extraction and the accelerating region through a pumping station (4) consisting of a turbo pump backed by a rotary pump. The isolation between two different sections of the beam line is maintained by utilizing Beamline Vacuum Valves, BLV, (5). Ions of required kinetic energy are extracted from an ion source with applied voltage difference between the high potential deck and the ground. This difference is distributed over accelerating tube (marked as 7) grounded on beam line end. The ion beam of required spot size is focused on desired location with help of electric quadrupole-triplet (QT, 9) whereas magnetic steerer (10) steers the beam on sample surface. Distribution of ions can be viewed in two perpendicular (x- and y-) directions using a Beam Profile Monitor (BPM, 14). Faraday cup and double slit (15) are respectively used for stopping the beam (if required) and for controlling the size of beam spot. Ions are mass analyzed, by applying the required value of magnetic field to the Mass Selection Magnet (17), and focussed, in the shape of a fine circular spot, during beam tuning. The beam is electromagnetically scanned using a beam scanner (18) for a homogeneous irradiation.

The ECR facility has been utilized for fabricating TiO_2 nanostructures. TiO_2(110) single crystals have been irradiated with 60 keV Ar^+ ions (flux = 1.8×10^{14} ions/cm^2.sec) from ECR. Irradiations were done for many ion fluences at room temperature.

Atom beam sputtering technique :

Fig. 2.2 shows the schematic diagram of Atom Beam Source (ABS) at IUAC, New Delhi. During operation, the Atom Gun ionizes gaseous atoms in the source region and transfers them towards the sample after accelerating them at high potential. The gas is directly fed into the source region which creates large number of positively charged ions during collision with heating plates. Ions produced in the source region are then accelerated towards the accelerating grid. These ions get neutralized through collisions with neutralizer gas atoms via charge exchange (in region after accelerating grid) before they striking sample surface. Atom beam of

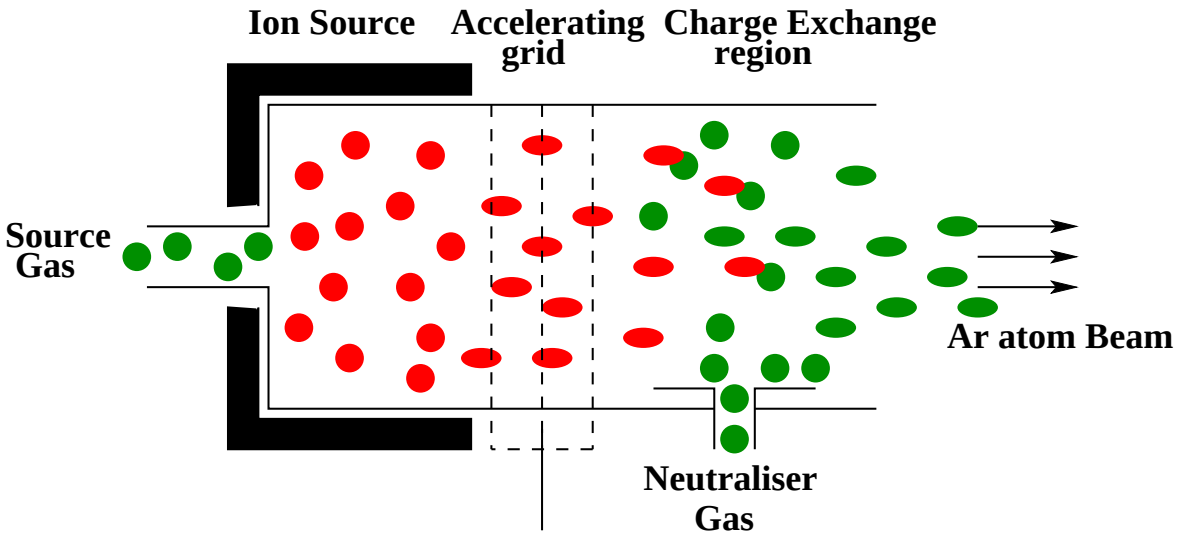

Figure 2.2: Schematic diagram of Atom Beam Source (ABS).

energy 100 eV-1.5 keV can be produced with this source. The beam current can be controlled by the gas pressure and acceleration voltage.

A schematic figure of ABS deposition system is shown in fig. 2.3. This system has been utilized for fabricating ZnO nanostructures by atom beam sputtering technique. ZnO(0001) single crystals were irradiated using 1.5 keV neutral Ar atom beam at room temperature under a vacuum of 7×10^{-7} Torr. An ion fluence of 1.2×10^{17} ions cm^{-2} and a flux of 2×10^{14} ions cm$^{-2} \cdot s^{-1}$ were used.

2.1.2 Hydrothermal Growth Method :

The hydrothermal technique is a popular solution-based synthesis method which has been widely utilized for the synthesis of various transition metal oxide nanostructures with desired size and morphology. It offers the synthesis of high quality nano-materials owing to its relatively lower crystallization temperature, controllable reaction conditions, slower growth rates etc. Several other controllable reaction parameters like cooling rate, pressure, mineralizer solution, length of reaction, and stoichiometry of reactant also provide better control on optimization of good quality nano crystal growth [4, 5]. The nano crystals, obtained by this growth method, have relatively less thermal strain and defect density compared to other NS, grown by traditional methods. This is important for designing and synthesis of new materials for many

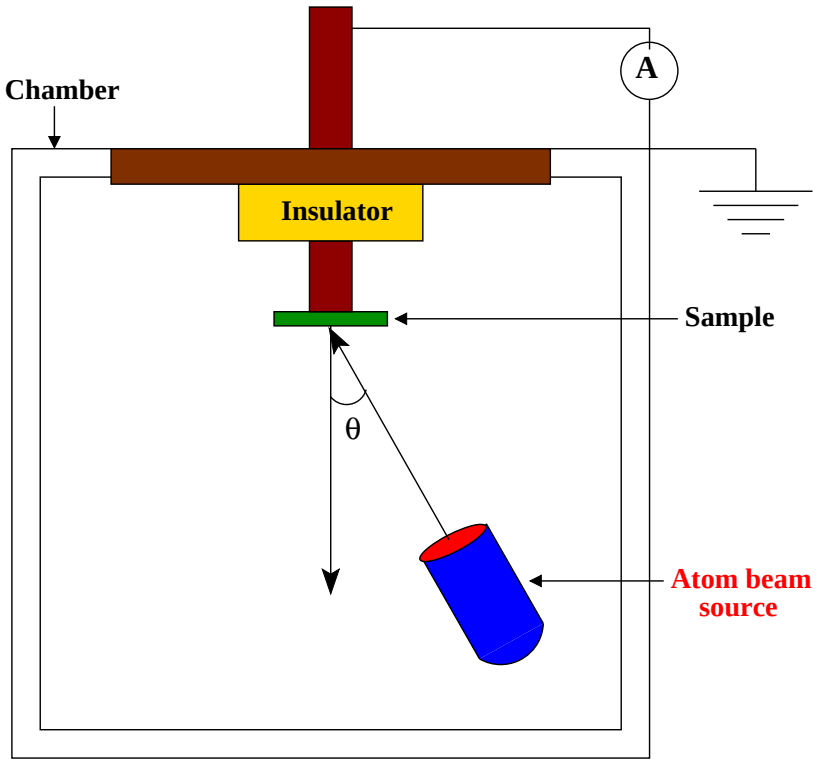

Figure 2.3: Schematic diagram of ABS deposition system.

applications.

A typical hydrothermal process requires the source of metallic cations, whose oxide phase is to be grown, and precipitants which work together and drive the whole reaction during the growth [6]. The typical hydrothermal synthesis is conducted in a sealed reaction container, reactor, with water as a medium for reaction. Reactions are allowed to proceed usually at temperature of $< 100°C$. A self-developed pressure increases with the reaction temperature. This pressure in the reactor is also sensitive to other parameters like the percentage fill of the vessel and the concentration of dissolved salts [4, 6]. Hydrothermal method requires simple reaction equipment like an oven and autoclave (reactor) and process can be easily controlled. This method can produce metastable phase formation utilizing the solubility difference between the growing phase and that serving as the starting material. During metastable growth by hydrothermal method, the nutrient consists of compounds that are thermodynamically unstable under the growth conditions. This leads to formation of metastable phase having higher solubility compared to the stable growing phase leading to the dissolution of metastable phase and crystallization of stable phase.

In the present thesis, $Ni(NO_3)_2$ and hexamine (HMT) were utilized as a source of Ni^{2+} ions and as a precipitant, respectively, for synthesis of NiO nanostructures. The deposition was performed at constant temperature of 60°C at varying reaction times from 2 to 10 hr.

2.2 Characterization Techniques :

2.2.1 X-ray Photoelectron Spectroscopy (XPS) :

In 1905, Albert Einstein [7] explained photoelectric effect using concepts of quantum nature of light. Kai Siegbahn and his group at Uppsala University (Sweden), in 1954, demonstrated the potential of XPS as powerful surface sensitive technique for revealing oxidation states and quantification of elemental distribution in any material [8, 9]. The unique ability of XPS to identify the chemical states of atoms, as a function of depth, makes it an invaluable tool for understanding the elemental composition and chemical interactions.

Photoemission can be described as a photon in and electron out process. In XPS, when X-ray photons strike a surface, in vacuum, electrons in core level can get excited and produce photoelectrons. These photoelectrons are energy analyzed and provide information on density of state (DOS) of the sample. The schematic of XPS process is shown in fig. 2.4 and fig. 2.5(a) presents the experimental setup for XPS. The X-ray source is a dual Mg-Al anode. X-rays on bombarding the sample produce photoelectrons which are energy analyzed by Hemispherical Analyzer and are counted or detected by the Channeltron (shown in figure 2.5(a)).

The kinetic energy of the photoelectron, E_K, of the photoemitted electron is given by the following relation:

$$E_K = h\nu - |E_B| - \phi_s \tag{2.1}$$

where $h\nu$, ϕ_s and E_B are the photon energy, spectrometer work function and binding energy of an electron in a specific level, respectively. As spectrometer and sample Fermi surfaces are at the same energy level during the measurements, the kinetic energy of the emitted electrons depends only on the spectrometer work function (fig. 2.5(b)).

XPS is a extremely surface sensitive technique. Though the X-ray photons can penetrate up to few micrometer within any material, elastically scattered electrons are from only top few nanometers due to small inelastic mean free path (IMFP) of electrons. The detection limit of

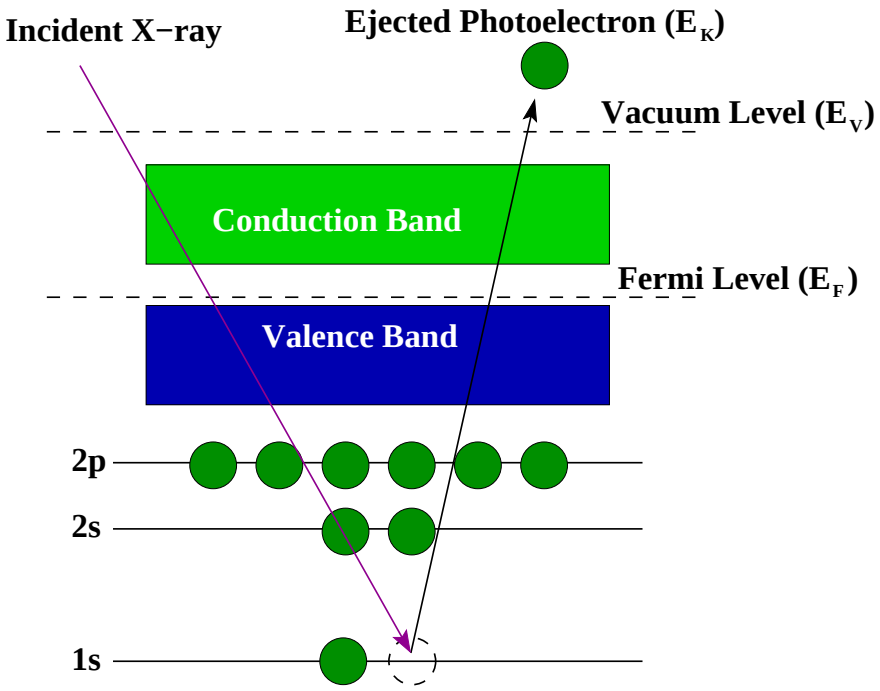

Figure 2.4: Pictorial representation of core level X-ray photoelectron emission process.

XPS for many elements is in the range of parts per million (ppm). This, however, requires special conditions like good concentration in the top surface layers and long collection times.

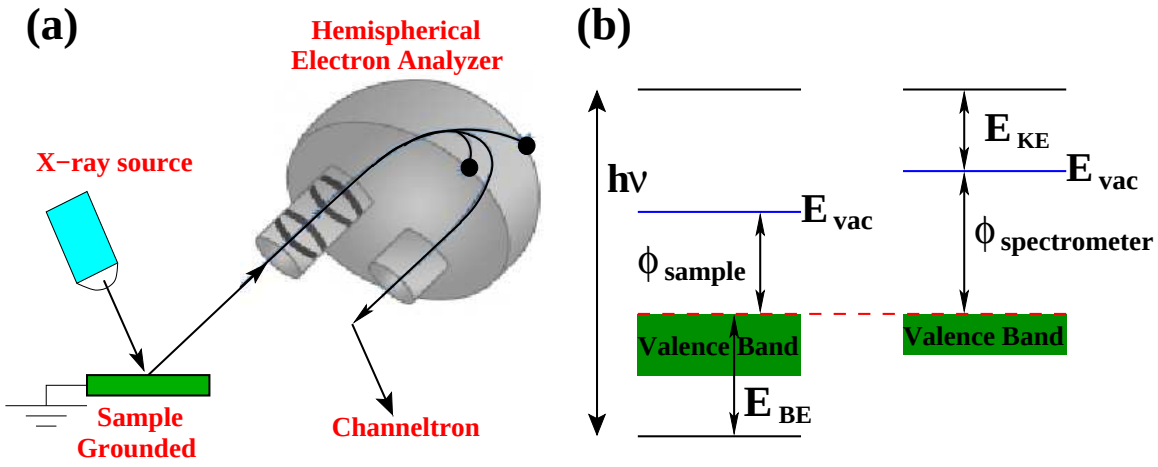

Figure 2.5: (a) Process of the photoelectron emission via X-ray-surface interaction and its detection by channeltron, and (b) schematic diagram to evaluate the kinetic energy, E_K, of the electron inside the atom.

The signal intensity, I_A, of photoelectrons derived from particular atoms, A, of a material at depth x is given by [10],

$$I_A(\theta, x) = FS_A N_A(x) exp\Big(\frac{-x}{\lambda cos\theta}\Big) \tag{2.2}$$

here, F, S_A, N_A and λ are the transmission function, relative sensitivity factor, concentration of atoms A and IMFP of electrons from atom A. θ is the electron emission angle measured from the surface normal. If some *i* types of atoms exist in the sample then the measured atomic concentration of element A, at emission angle θ is given by,

$$X_A(\theta) = \frac{I_A(\theta)/S_A}{\sum_i I_i(\theta)/S_i} \tag{2.3}$$

where, the term S_i is atomic sensitivity factor of i^{th} element and $\sum_i$ is the summation over all elements. Angle resolved XPS (ARXPS) spectra, thus obtained, at various photoelectron emission angles (θ) can provide depth dependent information. Here, large emission angles supply surface sensitive information (within top few Å) and low emission angles give results from surface to about 1 nm below. This characteristic behaviour arises due to the exponential dependence of XPS signal on sample depth. The surface sensitivity in ARXPS is a result of shorter attenuation length of electrons from sample. This is a very powerful technique for understanding depth dependent chemical state identification of elements present in sample, along with information on the local bonding nature of atoms and density of state (DOS).

In the present thesis, XPS system from VG has been used. The schematic diagram of the system setup is shown in fig. 2.6. The main system operates under UHV with a base pressure of 1×10^{-10} Torr. The load lock chamber has a base pressure of 1×10^{-8} Torr and is equipped with an Ar ion gun. For maintaining UHV, system is equipped with an ion pump, turbo molecular pump and rotary pump. The XPS system consists of a dual anode gun, Mg-Al, a hemispherical analyzer, and a channeltron unit. X-rays of energies 1253.6eV for Mg-Kα and 1486.6 eV for Al-Kα can be generated using dual anode gun. For any new sample, survey scans of around 1-1000 eV are first acquired by operating the analyzer with pass energy of $\sim$200 eV. After identifying the Regions of Interest (ROI) in survey scan, high resolution scans with $\sim$20 eV pass energy are obtained for all ROI. The instrumental resolution of the setup is 0.9 eV. The XPS signal has been collected at various emission angles (θ). For background subtraction of XPS data, Shirley background has been used. Binding energy corrections have been done by using adventitious Carbon 1s peak at position of 284.6 eV. The VGX-900 software has been used for analysis and peak fitting of XPS data.

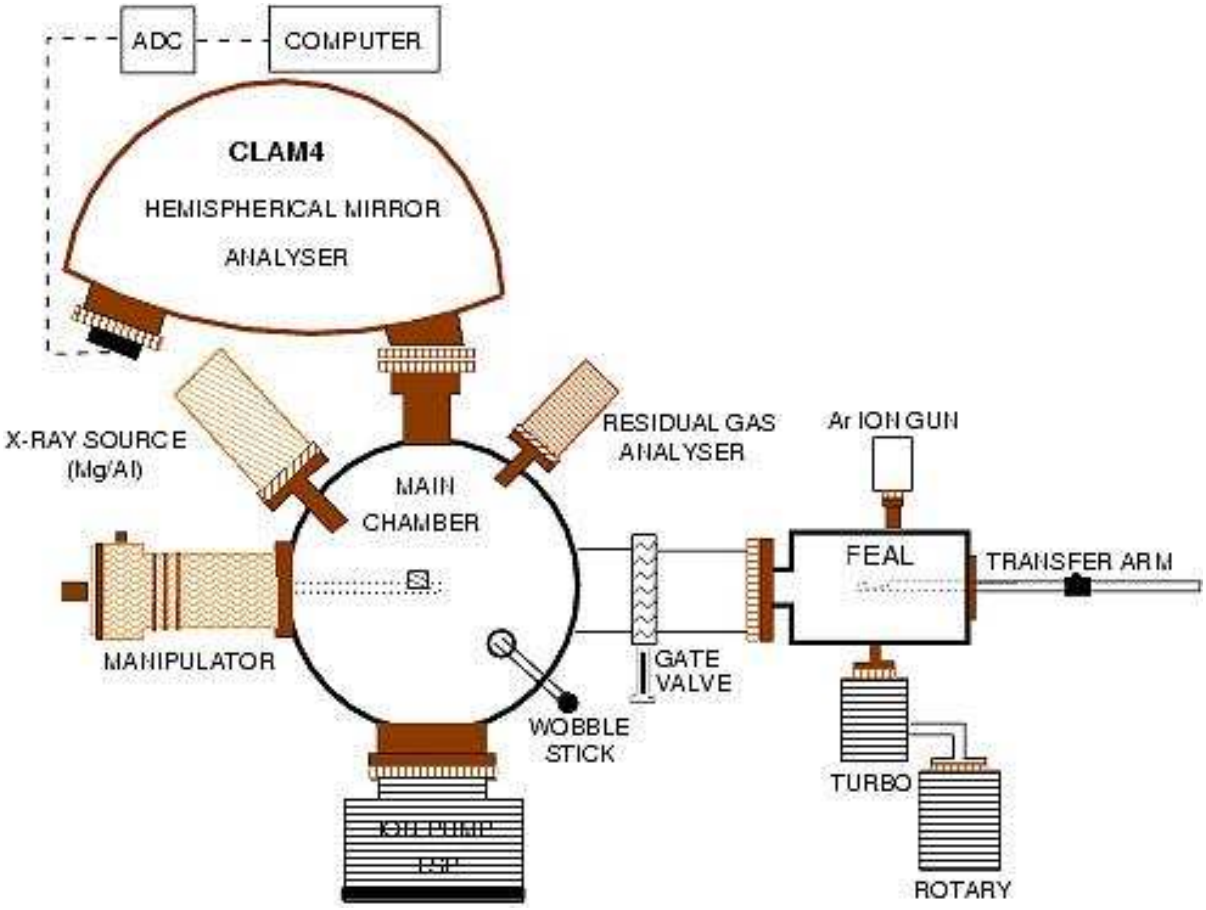

Figure 2.6: XPS system at IOP

2.2.2 Scanning Probe Microscopy (SPM) :

Scanning probe microscopy (SPM) consists of various microscopy technique which provide variety of surface information through scanning of a physical probe on the sample surface. Scanning probe microscopes can image several surface properties and related interactions simultaneously in real space. Depending on the property being measured, various techniques and modes of SPM have been developed. G. Binnig and H. Rohrer developed first Scanning Probe Microscope (SPM), in 1980, also known as Scanning Tunnelling Microscope (STM) [11, 12]. STM is based on the principle of quantum mechanical tunnelling phenomena. In STM, electrons tunnel through the vacuum gap between the conducting surface and conducting tip, generating a tunnelling current when a small bias is applied. Binnig, Quate and Gerber later invented atomic force microscope (AFM) [13] which has become a very powerful technique, measur-

ing forces between the atoms of the scanning tip and surface underneath. This technique of measuring forces does not require presence of conducting surface and can be utilized on any surface leading to many new developments in the field of SPM. Along with obtaining high resolution surface topography (by AFM or STM) many other surface information on magnetism (by Magnetic Force microscopy or MFM), conductivity (by tunnelling atomic force microscopy or TUNA, conducting AFM or CAFM) electrical (by Electrical Force microscopy or EFM), friction (frictional force microscopy), electrochemistry etc. can be obtained from same SPM setup by making few minor modifications of tips and sometime in its head unit.

In AFM, topographic information of the surface is collected by scanning a sharp tip, mounted at the end of a cantilever, over the surface. A tip is typically made of silicon or silicon nitride. The tip radius can be 10-50 nm and is attached to a 100-200μm long cantilever. The silicon tip is used for the non-contact mode (attractive forces) imaging whereas silicon nitride tip is more suitable for contact mode (repulsive mode) imaging. When the tip is brought in proximity to a sample surface, the measured forces between the tip and sample surface generate the topographic image of the sample. The forces measured in AFM are mechanical contact force, Van-der Waals forces, capillary forces, chemical bonding, electrostatic forces, magnetic forces, Casimir forces, solvation forces etc.

The main parts of AFM are its head, scanner and base as shown in fig. 2.7. Also shown in the figure are positions for laser, photo diode and the tip holder on the head. All electronic adjustments get displayed in Base (fig. 2.7). The sample is scanned in x, y directions under the AFM tip by piezoelectric translators made of Lead Zirconium Titanate (PZT). During imaging, a constant deflection (contact mode) or oscillatory amplitude (tapping mode) of the cantilever is maintained by feedback loop. Forces, acting between the atoms of the tip and the atoms of sample surface, lead to deflection of the cantilever. The photo- diode measures these deflections by detecting the reflection of laser light from the cantilever. The scheme used during surface imaging is shown in fig. 2.8.

Short range repulsive and long range, van-der Waals type, attractive interactions are the most important forces between atoms of the tip and the surface and are shown in fig. 2.9 through force-distance curve. The inter-atomic Lennard-Jones force F(r) can be expressed as :

$$F(r) = -\frac{A}{r^7} + \frac{B}{r^{13}} \tag{2.4}$$

where, A and B are constant parameters whereas r is the separation between tip and the

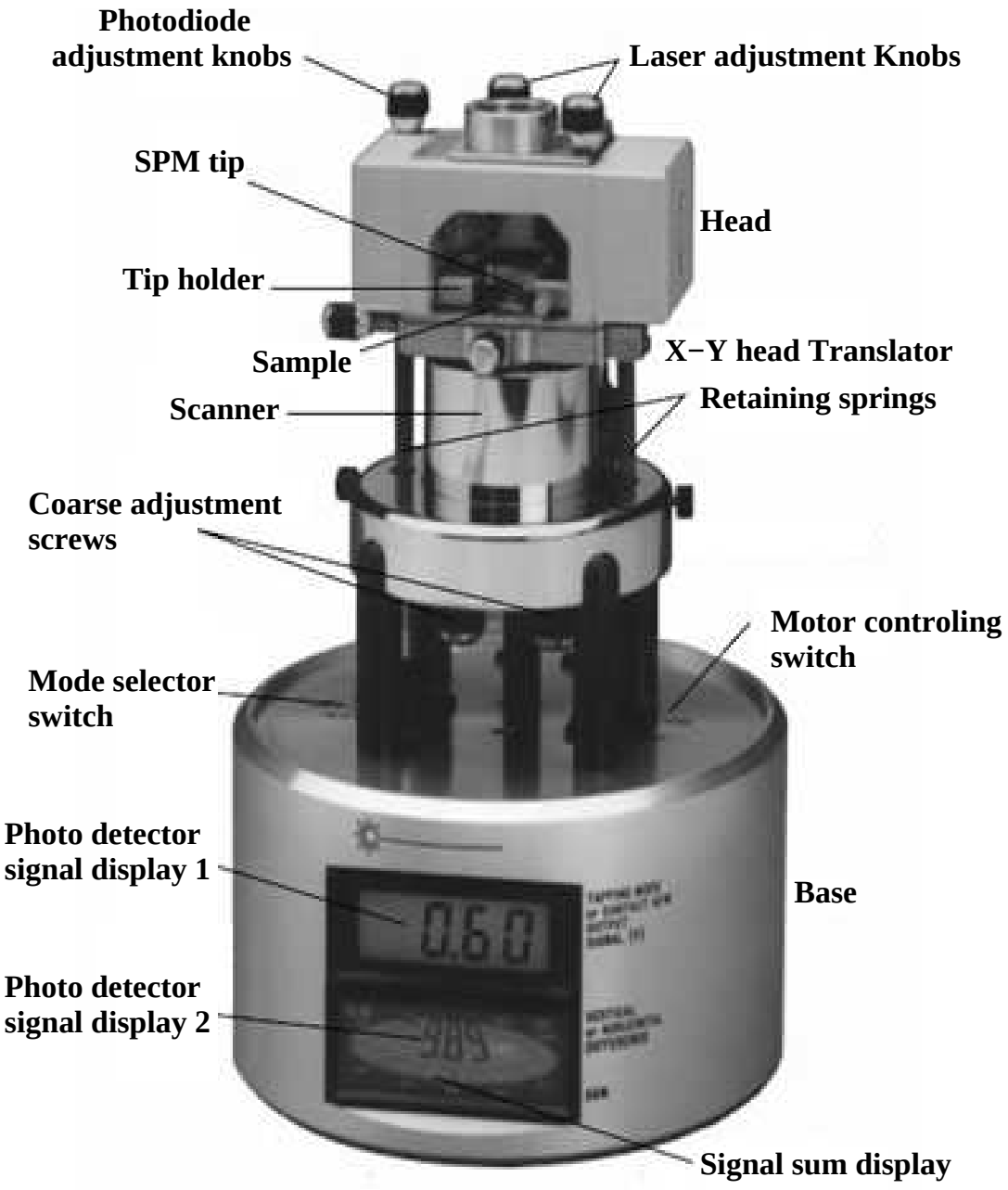

Figure 2.7: AFM system at IOP

sample surface. The probe predominantly experiences the repulsive forces when it is in contact with the sample (contact mode). The attractive forces start dominating as the tip moves away from the surface (non-contact mode). Out of these two, very high resolution imaging of the surfaces can be obtained by the varying repulsive inter-atomic force. Long range attractive forces greatly influence the motion of the tip, by pulling it towards the sample surface, resulting in generation of noise in the image. Depending on the nature of interactions between the atoms

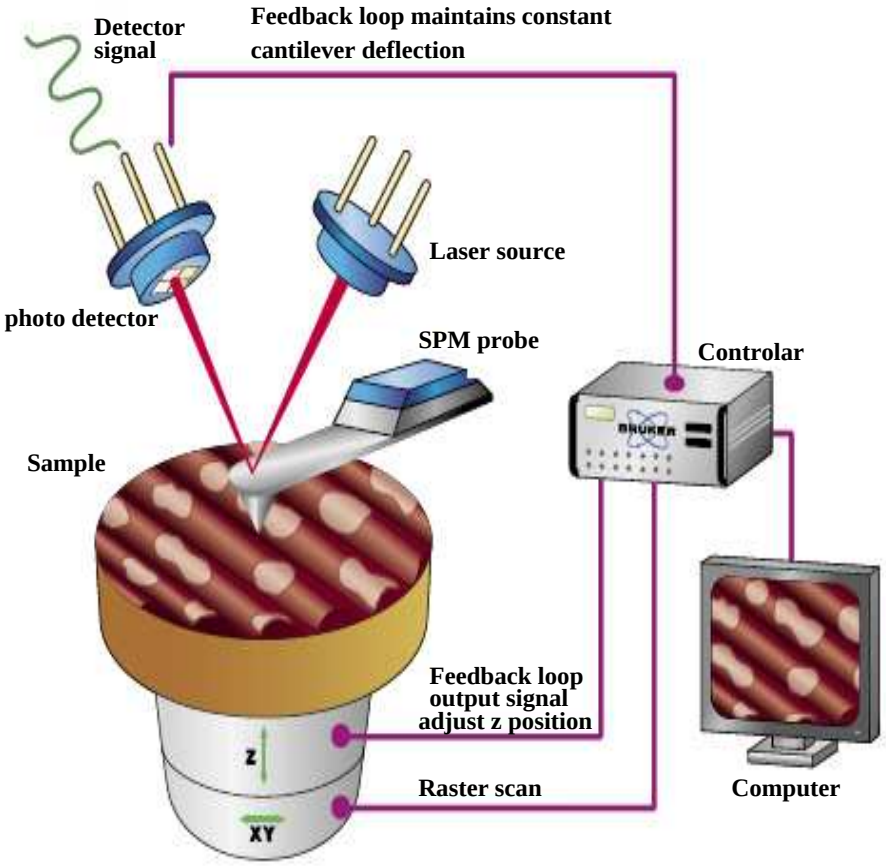

Figure 2.8: Operation of AFM

of the tip and the surface, there are three modes of operation used in AFM. They are described below:

Different modes of AFM :

i. Contact mode operation :

In contact mode, the tip is in direct contact with the surface and force acting between the atoms of tip and the sample is counter balanced by the elastic force produced by the deflected cantilever, according to Hooke's law F= -kz where k and z are spring constant and deflection of the cantilever, respectively. The relatively small stiffness of the cantilever, used in contact mode, allows one to image the surface topography with high sensitivity. The system can be operated under constant height mode or constant force mode. In constant height mode, the typical separation between the tip and the sample is < 0.5 nm. In constant force mode, the motion of the

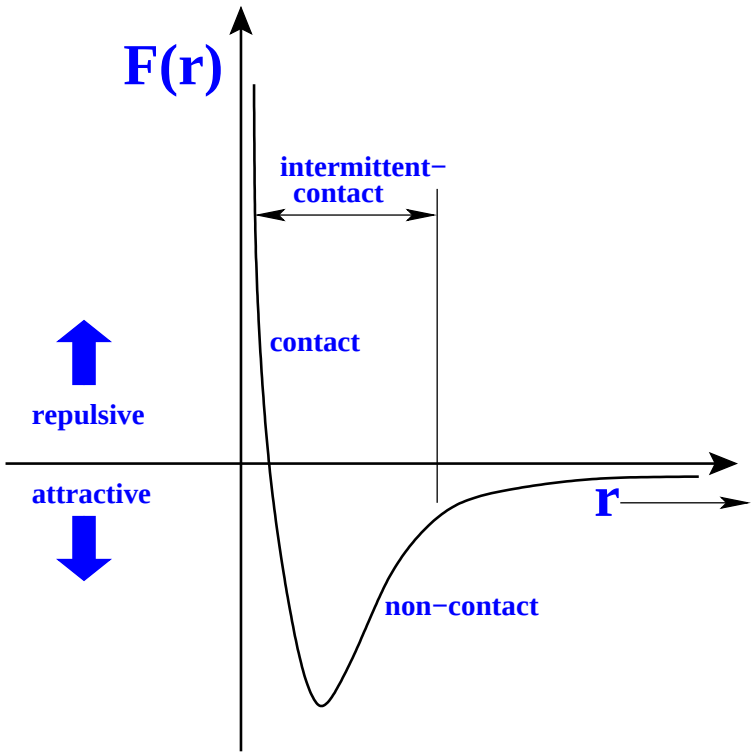

Figure 2.9: Force Displacement curve (F-r) for two atoms

scanner along z-direction is recorded for constant cantilever deflection. The drawback here is the lateral force exerted on the sample can be quite high. This can result in sample damage or the movement of relatively loosely attached objects. Therefore, this mode is more suitable for hard materials.

ii. Non-contact mode operation :

In non-contact mode, the tip does not make any physical contact with the sample surface. The cantilever oscillates with a resonant frequency where the amplitude of oscillation is typically a few nanometers ($<$ 10 nm) down to a few picometers. The oscillation amplitude of the cantilever is influenced by the long range Van der Waals forces, which are strongest from 1 to 10 nm above the surface. This change in resonant frequency combined with the feedback loop system maintains a constant oscillation amplitude or frequency by adjusting the average tip-to-sample distance. The measured tip-to-sample distance at each (x, y) data point is used to construct the topographic image of sample surface.

iii. Tapping mode operation :

In tapping mode, the cantilever is driven to oscillate up and down at near its resonance frequency similar to the non-contact mode. However, the amplitude of this oscillation is larger than 10 nm, typically 100 to 200 nm. When the tip approaches the surface, the forces (like Van der Waals, dipole-dipole, electrostatic etc.) between the atoms of tip and sample can change the vibration amplitude of the cantilever. Here, the surface is scanned at constant reduction of the oscillation amplitude instead of constant deflection. Hence, there is no mechanical contact between the tip and the surface during the scan. The amplitude used for the feedback and the vertical adjustments of the piezoscanner are recorded as a height image.

In the present thesis, surface morphology investigations have been performed by using multimode AFM (fig. 2.7), with Nanoscope IIIa (with quadrature) and V controllers, from Bruker. All the 2d and 3d morphology images reported here are acquired in tapping mode. Tunnelling AFM (TUNA) or Conducting Atomic Force Microscopy (CAFM) has been utilized for measuring I-V properties of the surface and nanostructures. Analysis has been performed with Nanoscope software.

2.2.3 UV-VIS Spectroscopy :

When radiation passes through matter, various processes like reflection, scattering, absorbance, fluorescence/phosphorescence, photochemical reaction etc. can take place. The absorbance of light or photon by matter can increase the total energy content of the molecules or atoms. This provides important information about absorbing nature of the material. Investigations in Ultra- violet (UV) and Visible (Vis) regions of the energy spectrum are especially useful while understanding wideband gap materials which exhibit interesting properties in this energy range. The total energy of the molecules is given by:

$E_{total} = E_{electronic} + E_{vibrational} + E_{rotational}$

And the energy difference among the different states are in the order

$E_{electronic} > E_{vibrational} > E_{rotational}$

When the energy of incident photon is enough to cause transitions between the different electronic energy levels, then an electron transits from a lower energy level to a higher energy level.

In the case of atoms, these transitions produce very narrow absorbance bands at wavelengths

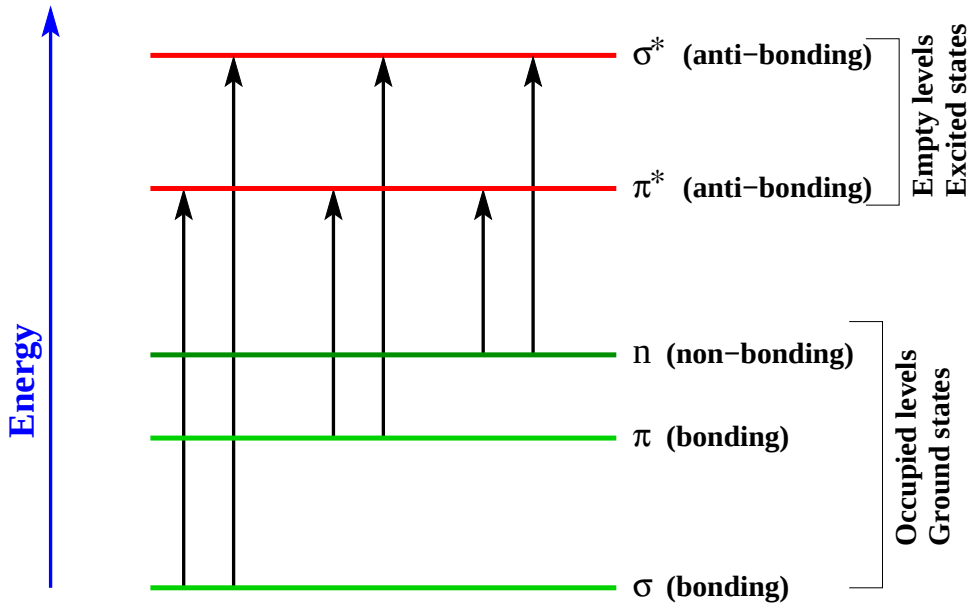

Figure 2.10: Generalised molecular orbital energy level diagram and different possible transitions.

highly characteristic of the difference in energy levels of the absorbing species. However, for molecules, the bands are broadened due to the superimposition of many vibrational and rotational energy levels on the electronic energy levels.

The absorption of light by a sample in the ultraviolet or visible region is accompanied by the changes in electronic states of the molecules. The energy supplied by the light will promote electrons from their ground state orbitals to the higher energy excited state orbitals or anti-bonding orbitals. Three types of ground state bonding orbitals may involve in the electronic transitions: σ bonding orbitals, π bonding orbitals and non bonding (n) orbitals (see fig. 2.10). In addition two anti-bonding orbitals, σ^* orbitals and π^* orbitals, are also involved in the transition. The different types of allowed transitions between bonding and anti-bonding orbitals are as follows:

• σ to σ^*: An electron in a bonding σ orbital is excited to the corresponding anti-bonding orbital. This type of transitions require large energy and therefore occur in the far ultraviolet region and not in typical UV-Visible region (200-700 nm). As a result electrons involved in this type of transitions generally absorb UV light, with lower wavelength, and these are rare transitions.

• n to σ^* : An electron in a non-bonding (n) orbital is excited to the anti-bonding σ^* orbital. This type of transitions usually need less energy compared to σ to σ^* transitions. They can be initiated by photons whose wavelength is in the range of 150 - 250 nm. Saturated compounds containing atoms with lone pairs (non-bonding electrons) can show this type of transitions.

• n to π^* and π to π^* : As these type of transitions fall into an experimentally convenient region of the spectrum (200 - 700 nm, UV-Visible), most absorption spectroscopy of organic compounds is based on n to π^* and π to π^* transitions. These transitions occur in the molecules with unsaturated centers. They require less energy compared to σ to σ^* and n to σ^* transitions and occur at longer wavelength.

The absorption spectra help to determine the electronic property of the material. The wavelength at maximum absorption can provide the information regarding the electronic structure of the material. According to Beer's Law, the absorbance is directly proportional to the path length, *l*, and the concentration, c, of the absorbing species [14], and is given by,

$$A = \varepsilon lc = \alpha l \tag{2.5}$$

where ε is a constant of proportionality, called the molar absorptivity or molar extinction coefficient and α is absorption coefficient. Using absorbance (A) and Beer's law we can determine either the concentration of a sample if the molar extinction coefficient is known, or the molar absorptivity, if the concentration is known.

Assume that radiation of intensity, I_i, is incident on a solid sample, a portion of this radiation gets absorbed in the sample, and intensity, I_o, of radiation is transmitted through the solid. Then, the amount of radiation absorbed in sample can be measured. This absorbance (A) depends on the transmittance (T) or the percent transmittance (%T) of radiation through the sample as :

$A = \log_{10} T$ or $A = 2 - \log_{10}(\%T)$.

where $T = I_o/I_i$ and $\%T = 100\ T$.

Measurement of the Electronic Bandgap of Semiconducting Materials :

In semiconductors, there is a finite energy difference between top of the valence band and bottom of the conduction band, known as bandgap energy, E_g, of the material. This is the minimum energy required for an electron excitation from the top of valence band to the bottom

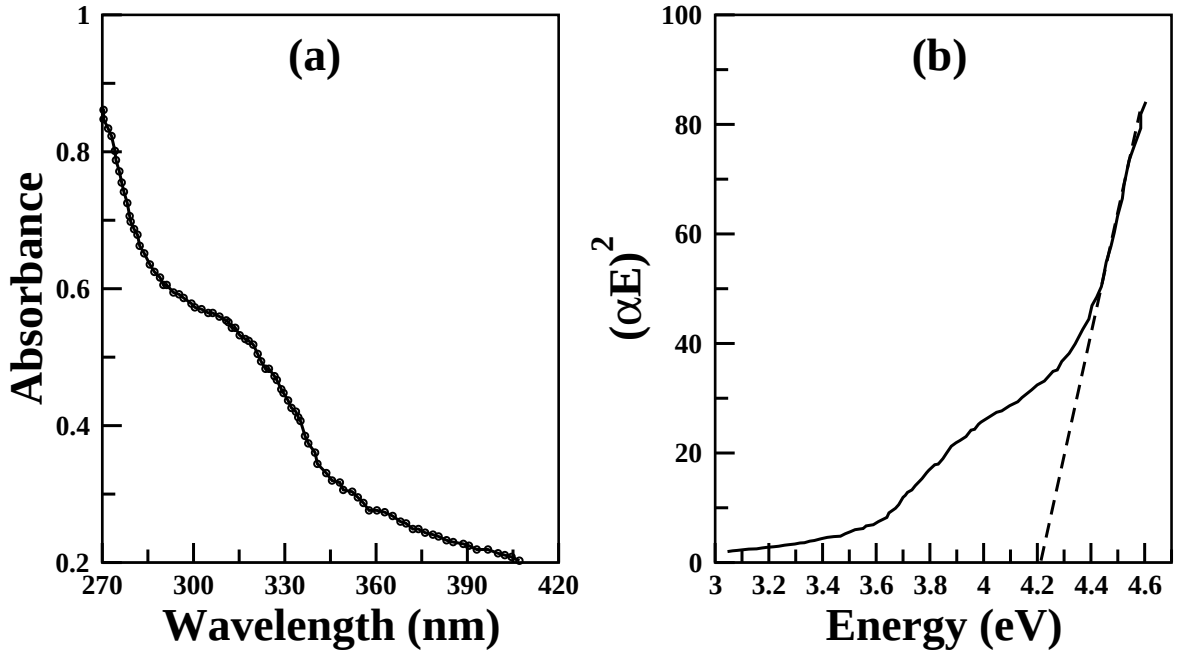

Figure 2.11: A typical UV-Vis spectra (a) and corresponding Tauc plot (b) for ZnS nanoparticles with E_g= 4.22 eV [15].

of the conduction band [16]. If the energy of the incident radiation (photon), hν, is higher than E_g then electronic transition takes place from valance band to conduction band and a sharp absorption profile is observed. Absorption remains high for photon energies higher than E_g. However, for energy less than E_g, the absorption will be small, or absent. Therefore, the material displays a sharp increase of absorption near E_g. This gets manifested as an absorption edge (or reflection threshold) in the UV-Vis absorbance spectrum.

A typical absorbance spectrum, e.g. for ZnS nanoparticles, with a bandgap energy of $\sim$4.22 eV is presented in fig. 2.11(a) [15]. Here, absorption edge can be seen near the wavelength of 294 nm. E_g can be calculated from this spectrum by utilizing Tauc equation [17]:

$$\alpha h\nu = A(h\nu - E_g)^n \tag{2.6}$$

where, α and A are the absorption coefficient of the material, and a constant, respectively. hν is the incident radiation energy. Exponent *n* denotes the nature of transitions and takes the following values [18]:,

- n = 1/2 for direct allowed transitions
- n= 3/2 for direct forbidden transitions

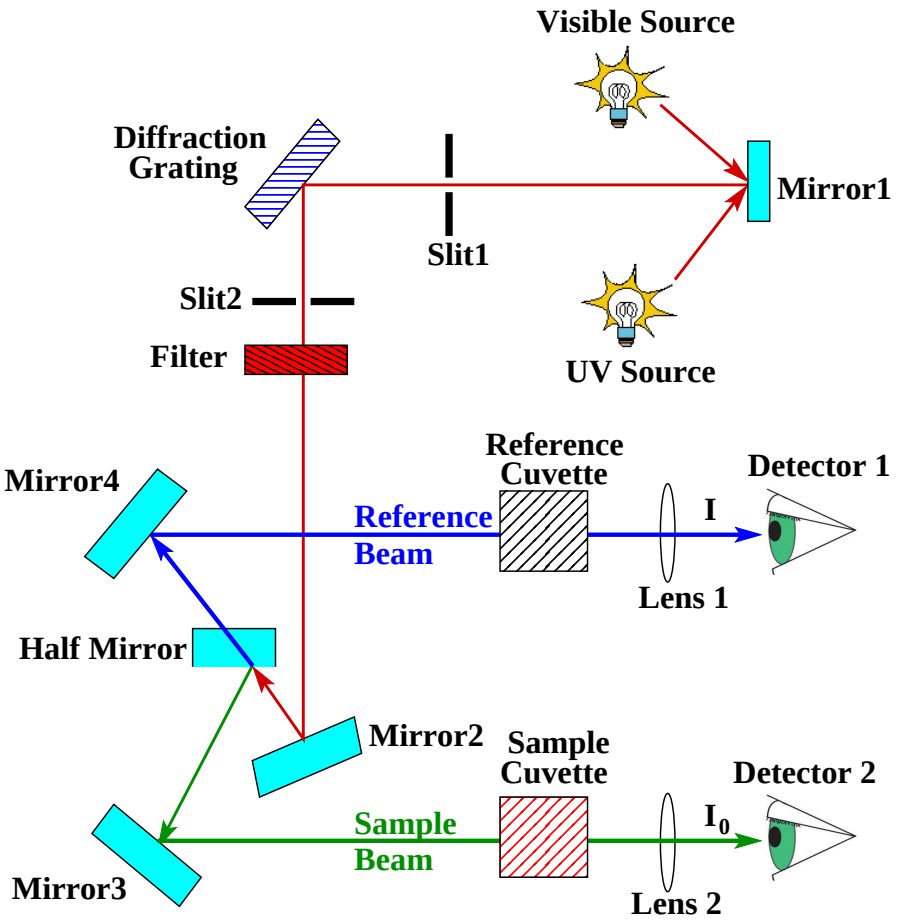

Figure 2.12: UV-Vis spectroscopy setup.

- n= 2 for indirect allowed transitions
- n= 3 for indirect forbidden transitions.

A Tauc plot is a convenient way of displaying the optical absorption spectrum of a material [17]. Here, the quantity hν is plotted on abscissa and $(\alpha h\nu)^{1/n}$ on the ordinate. The Tauc plot in 2.11(b), obtained by utilizing absorbance spectrum of 2.11(a) [15], displays a distinct linear regime which denotes the onset of absorption. Extrapolating this linear region to the abscissa provides the energy of the optical band gap of the material (i.e. E_g of 4.22 eV for ZnS).

In the present thesis, Shimadzu UV-Vis Spectrophotometer was utilized to perform the absorbance measurements. In a double beam spectrometer, a beam splitter splits the radiation, coming from the monochromator, into two beams which are passed simultaneously through the reference and the sample cell. The transmitted radiation is detected by the detectors and the difference in the signal, at all wavelengths, is suitably amplified and detected. The schematic of the spectrophotometer is shown in fig. 2.12. The set up consists of two light sources. Deuterium

arc discharge lamp is capable of generating high intensity radiation in the UV region (∼190-380 nm range) and tungsten-halogen lamp, can emit radiation in the visible range (∼380-900 nm). During scanning, between the UV and visible regions, the lamps get swapped automatically by the system. A SiO_2 coated reflecting optical system with holographic grating monochromator (1440 Lines/mm UV/Vis blazed at 240 nm) disperses the required wavelength from continuous light source. The spectral bandpass is then determined by the monochromator slit width or by the array-element width in array-detector spectrometers. Spectrometer designs and optical components are optimized to reject stray light, which is one of the limiting factors in quantitative absorbance measurements. The detector is the photomultiplier tube which show good efficiency in the full UV/Vis range. The maximum resolution in the measurement offered by this system is ≤ 0.17 nm.

2.2.4 X-ray Diffraction(XRD) :

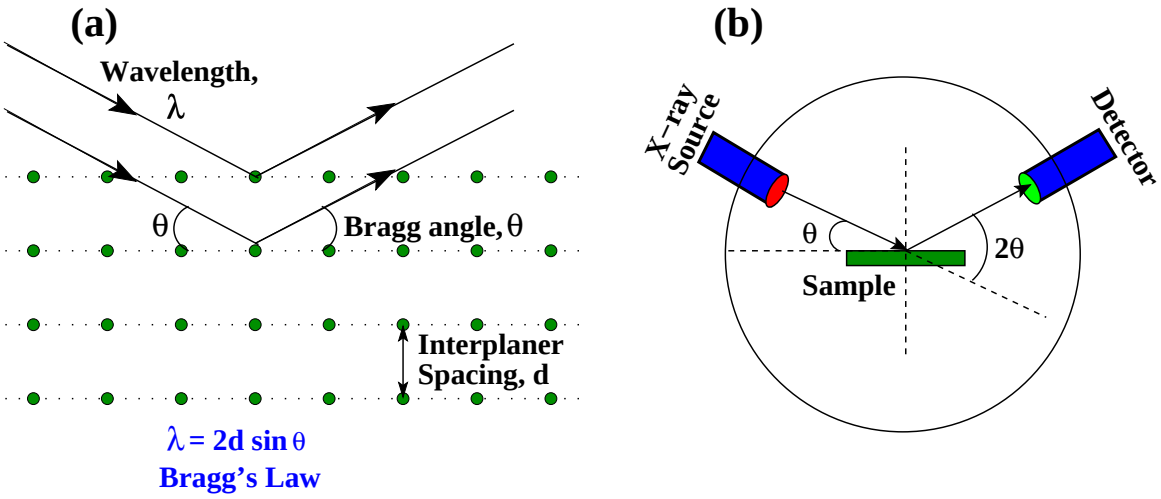

Figure 2.13: (a) Bragg's reflection in single crystal and (b) X-ray diffractometer setup.

X-Ray Diffraction (XRD) is a powerful analytical technique which is extensively used for identification of crystalline material, analysis of its unit cell dimensions and its phase determination.The method is based on the principle of Braggs Law which states that constructive interference takes place whenever the differences in the total path length, travelled by the incident photon, is equal to an integral multiple of incident wavelength [19], i.e.

$$n\lambda = 2dsin\theta \tag{2.7}$$

where λ is the wavelength of the incident photon, θ is the incident angle as shown in figure (fig. 2.13(a)), n is an integer and *d* is the inter-planar spacing of the crystalline sample. Detection of diffracted X-rays, after interaction of incident X-rays with sample, is performed by X-ray detector. The process is repeated as the sample is scanned through a range of 2θ angles. This allows for the production of all possible diffraction directions (or diffraction pattern) of the crystalline sample, due to its interaction with incident X-rays (of specific wavelength λ). For identification of the crystal or its specific phase, the diffraction peaks are converted to respective d-spacing and compared with standard reference data.

In this thesis, an X-ray diffractometer from Bruker has been utilized for performing XRD measurements. X-ray diffractometer primarily consists of three basic parts which are an X-ray source, a goniometer, and an X-ray detector. The source provides CuKα X-rays (λ=1.5415 $\mathring{A}$) which are collimated and directed onto the sample. The geometry of an X-ray diffractometer is such that the sample rotates by an angle θ while the X-ray detector rotates at an angle of 2θ. A goniometer is used to maintain the angle and rotate the sample. The sample rotates in the path of the collimated X-ray beam at an angle θ. The X-ray detector is mounted on an arm to collect the diffracted X-rays and rotate at an angle of 2θ (fig. 2.13(b)). The intensity of the diffracted X-rays (from sample) is recorded as the sample and the detector are rotated. Constructive interference occurs whenever the geometry of the incident X-rays impinging the sample satisfies the Bragg condition. This condition produces a peak in intensity profile related to the specific lattice spacing, d, in the crystal. Detector processes the signal to produce a count rate which is then output to a computer. The specific peak positions and their relative intensity provide the characteristic designation of the crystal structure of the sample.

2.2.5 Photoluminescence(PL) Spectroscopy :

Photoluminescence (PL) is light emission from any material by photo-excitation, after the absorption of photons. During photo-excitation, some states get populated and subsequently, many relaxation processes occur in which other (than excitation energy) photons are re-radiated. Time periods between absorption and emission process vary and can range from femtoseconds to milliseconds. A feature in the PL spectrum provides information on the transition energy

that gets utilized for populating the excited state. The PL spectroscopy is a powerful non-destructive technique for material characterization as well as for measuring the purity and crystalline quality of semiconductors. It is also extensively utilized for estimating the amount of disorder present in a semiconductor. During a typical PL experiment on a semiconductor, it is excited with photons of energy larger than the bandgap of the material. Subsequently, upon the absorption of photons, electrons and holes respectively get created, with finite momenta, in the conduction and valence bands. Finally, with energy and momentum relaxation towards the band gap minimum, PL is observed when electrons and holes recombine. In the present thesis, Horiba Jobin-Yvon system, with He-Cd laser (325 nm) as an excitation source, has been used for the PL measurements at room temperature.

2.2.6 Superconducting quantum interference device (SQUID) :

A superconducting quantum interference device (SQUID) is a very high sensitive magnetometer used to measure extremely subtle magnetic fields, based on superconducting loops containing Josephson junctions.

The entire SQUID instrument consists of six basic components:

1. Temperature Control system.
2. Magnetic field control system.
3. Motion control system.
4. SQUID detection system.
5. Chamber atmosphere control system.
6. Cryogen monitoring system.

Liquid helium is required for the operation of SQUID. Liquid helium cools the superconducting solenoid (magnet) providing magnetic field to the instrument and its associated components like superconducting electrical leads, quick switch etc. Liquid helium also cools the superconducting quantum interference as well as the magnetic shield and detection coils, inductively coupled to the SQUID. The superconducting quantum interference provides the instrument's sensitivity to magnetic moments. The sample, loaded in the sample chamber, gets cooled to 1.8 K via drawing the cold helium gas in the space surrounding the chamber, by means of vacuum pumps.

The vertical magnetic field in the SQUID VSM is generated by a superconducting Niobium

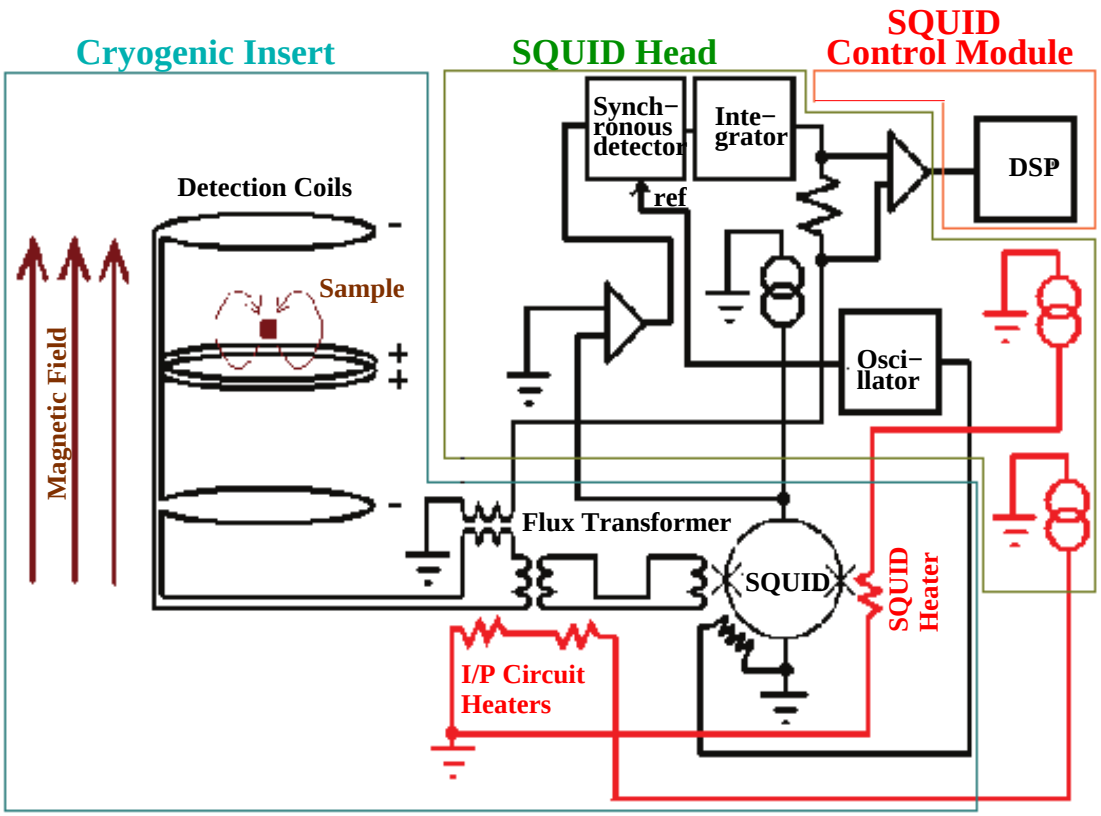

Figure 2.14: Example of SQUID detection diagram.

Titanium (NbTi) solenoid. Current is supplied by the magnet controller via a set of permanent current leads. The motion control system moves the sample within the detection coils with the help of VSM motor. A precision optical encoder reads the position of motor armature, with an accuracy of 0.01 mm, and fed to the motor control module and in a feedback loop. This provides precise sample positioning and vibration.

The SQUID detection system is composed of following sub units (fig. 2.14):

1. A set of superconducting detection coils, inductively coupled to a magnetically-shielded SQUID
2. A SQUID head that biases the SQUID, provides feedback control and signal amplification.
3. A CAN-based SQUID control module with a digital signal processor (DSP) which performs synchronous AC detection.

In the standard measurement, the instrument positions the sample at the center of the detection coil set, where the SQUID signal peaks. The sample vibrates at 14 Hz frequency and

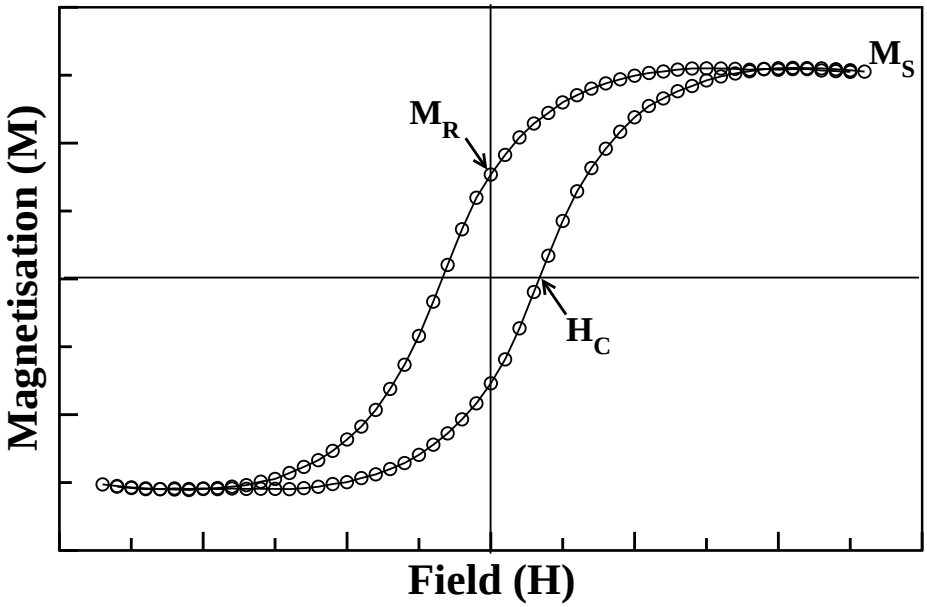

Figure 2.15: Example magnetisation loop for ferromagnetic material.

generates a 28 Hz SQUID signal (magnetic moment) at the input to the SQUID control module.

The magnetic properties of a material can be analysed from the magnetic field vs moment measurements. For this purpose, the magnetic field is scanned and corresponding magnetic moment detected by the SQUID is recorded in the form of a M-H curve. All ferromagnetic materials exhibit magnetic hysteresis loop, when subjected to an external magnetic field. Fig. 2.15 shows the typical hysteresis loop obtained by a ferromagnet. As the external field increases, the magnetization of the sample also increase till it reaches a saturation value, called saturation magnetisation (M_S). Thereafter, even if the field is completely removed, the sample still retains some of its magnetization, known as remanence or M_R. If the external field is now reversed, the magnetization slowly drops, until it is completely demagnetized, at a value for the external field corresponding to the coercive field or coercivity (H_C).

The magnetic measurements reported in the thesis have been performed on Quantum design SQUID VSM [20]. The instrument was operated in a temperature range of 2 K to 300 K and a magnetic field range of -70 to +70 kOe. The sensitivity of the instrument is 10^{-8} emu.

2.2.7 Transmission Electron Microscopy (TEM) :

The transmission electron microscopy (TEM) is a powerful technique allowing imaging with chemical specificity of crystalline nanomaterials with atomic resolution. Investigations of crystal structures, orientations, estimates of chemical compositions of constituent phases, formation of alloys etc. are routinely performed. Methods of analysis include diffraction pattern analysis, atomic contrast imaging, X-ray emission, electron-energy loss spectroscopy etc. In the microscope, a high energy beam of electrons is transmitted through an ultra thin, $\sim$50 to $\sim$100 nm, specimen. The electrons interact with the specimen and an image is formed from this interaction. This image can be focussed and magnified several orders of magnitude. The higher resolution in TEM compared to optical microscope is due to the smaller de Brogile wavelength of electrons compared to visible light.

In the present thesis, high resolution transmission electron microscopy (HRTEM) from JEOL has been used. The system is equipped with a LaB_6 electron gun. System has a point-to-point resolution of 0.19 nm, and a lattice resolution of 0.14 nm with 200 keV electron energy. Nanostructures studied here, were first dispersed in acetone and then put on the amorphous carbon-coated copper grid. The images were recorded using GATAN ccd camera.

2.2.8 Field Emission Scanning Electron Microscopy (SEM) :

A Field Emission Scanning Electron Microscope (FESEM) consists of an electron gun and a demagnification system, fitted inside an electron column. The demagnification system, equipped with electromagnetic lenses focuses a beam of electrons to a nanometer size on the sample. Electron and x-ray detectors are also mounted inside the sample chamber. A computer interface is used to couple the detectors to display highly magnified image of the surface. During imaging, the energetic electrons undergo series of elastic and inelastic scattering events inside a material. These interactions produce different signals like backscattered electrons, characteristic x-rays, secondary electron etc. The secondary electrons are used for topographical imaging with high contrast and better resolution whereas x-ray signal is used for the energy dispersive analysis.

In the present thesis, a Carl Zeiss-make FESEM microscope having Schottky thermal field emitter electron source, with a probe current up to 100 nA and acceleration voltages from

0.02 to 30 kV was used. This electron source offers resolutions of 1.2 and 2.2 nm at acceleration voltages of 15kV and 1.0kV, respectively. The system's magnification is in the range 10-100,000 times, and produces three dimensional image of the surface morphology. The system is also equipped with 5-axis motion stage : X: 0 to 125mm, Y: 0 to 125mm, Z: 0 to 50mm, rotation up to 360° and tilt from -10° to 90°.

2.3 Metal Oxides: Crystal structure and properties

Distinctive feature of metal oxides compared to their corresponding metals is the high degree of ionic bonding in oxides. In an ideal ionic crystal, complete charge transfer between adjacent atoms leads to stable configurations. Cations and anions, thus produced, induce strong electrostatic interaction among the ions. These forces are long-ranged, having 1/r dependence, which allow the ions to interact beyond the nearest neighbours. In a crystal, the ions are arranged in a fashion that they maximize the contact with oppositely charged and minimize repulsion with the similarly charged. Thus, the crystal structure is determined by the coordination number and the relative sizes of the involved species [21–23]. The crystal structure of metal oxides is highly sensitive to changes in the environment, like presence of defects, which give rise to significant modifications in both, bulk and surface [24–26]. Oxygen vacancy is the most studied point defect on metal oxide surfaces. Removal of a neutral oxygen atom leads to creation of oxygen vacancy [25, 26] which can in principle reduce the coordination of the surrounding cations by donating one or more electrons to it. These electrons can occupy the vacancy site or can populate the metallic electron levels of surrounding unsaturated metal atoms [21]. In the present thesis, rutile TiO_2 (110) and wurtzite ZnO (0001) single crystals, commercially purchased from MaTeck have been investigated. Studies of hydrothermally grown NiO nanostructures are also presented.

2.3.1 Titania (TiO_2) :

Titanium is the ninth most abundant element in the Earths crust as it is present in many silicate and oxide minerals, but in small percentage. However, bulk TiO_2 does not exist in the nature [27,28]. Titanium dioxide displays wide range of promising properties including high refractive

index, durability, strength, chemically inert nature, bio-compatibility, non-toxicity etc. These properties enhance its utilization in many applications including heterogeneous catalysis [29–32], photocatalyst [33] for waste water treatment [34], in biocompatible implants [35, 36], in solar cells for the production of hydrogen and electrical energy [33, 37], gas sensor [21, 38], as an optical coating [39], etc. Sterilisation of surfaces by UV irradiation, which remain so for long time after irradiation, renders it exceptional for bio related and medical applications [34, 40]. Titanium dioxide is also widely used as sunblock in sunscreen creams, as it scatters the light without irritating the skin [41], and for cleaning air in space [42].

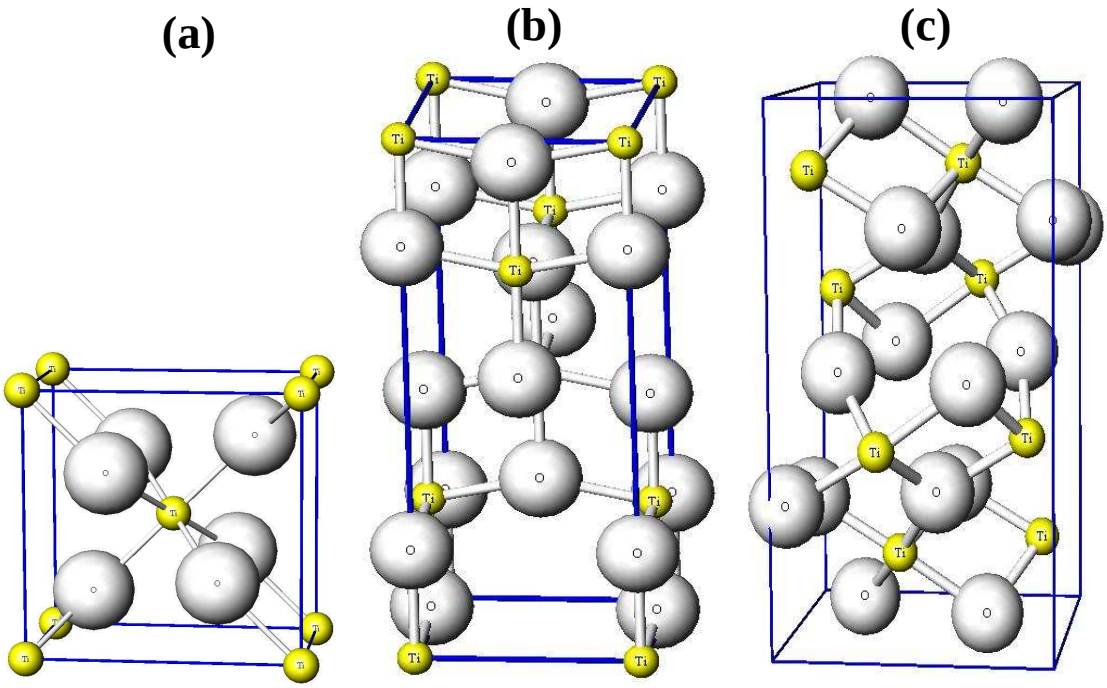

Figure 2.16: Crystal structures of TiO_2: (a) rutile, (b) anatase and (c) brookite. Grey (big) and yellow (small) spheres represent the oxygen and titanium atoms, respectively (from ref [43]).

Titanium dioxide mainly exists in three polymorph phases which are rutile (tetragonal, fig. 2.16(a)), anatase (tetragonal, fig. 2.16(b)) and brookite (orthorhombic, fig. 2.16(c)) [44]. Out of all these phases, rutile and anatase have been widely studied for their photo-activity [29–33, 44]. Variations in their phases can be understood in terms of octahedral (TiO_6^{2-}) differing by the distortion and connectivity of the octahedral chains. Navrotsky et al. [45] had reported the stability of the different TiO_2 crystal structures in the following order: rutile $>$ brookite (+0.7 kJmol^{-1}) [46] $>$ anatase (+2.6 kJmol^{-1}) [47] with an error of $\pm$ 0.4 k J mol^{-1}.

The crystal structures for all the three phases of TiO_2 are shown in fig. 2.16. Their respective

crystal parameters and physical characteristic are presented in table 2.1.

Table 2.1: Lattice parameters of TiO_2

	Rutile ([48, 49])	Anatase ([49–51])	Brookite ([49–51])
Z[a]	2	4	8
a($\mathring{A}$)	4.587	3.781	9.174
b($\mathring{A}$)	4.587	3.781	5.449
c($\mathring{A}$)	2.954	9.515	5.138
Volume[b]	31.21	33.98	32.17
Formula Wt.	79.89	79.89	79.89
Crys. System	Tetragonal	Tetragonal	Orthorhombic
Point Group	4/mmm	4/mmm	mmm
Space Group	$P4_2/mnm$	$I4_1/amd$	Pbca
Bandgap (eV)	3.2	3	2.96

a, b, c are the lattice parameters of the unit cell
[a] Z is the number of asymmetric units in the unit cell
[b] Volume is in $\mathring{A}^3$ per TiO_2 formula unit.

2.3.2 Zinc Oxide (ZnO) :

Zinc Oxide (ZnO) is a wide-bandgap semiconductor of group II-VI. It is n-type due to the native doping of oxygen vacancies or zinc interstitials [52]. ZnO has many exciting properties like good transparency, high electron mobility, wide bandgap and strong room-temperature luminescence, etc. As a result, it can be used in variety of applications related to transparent electrodes in liquid crystal display, energy-saving or heat-protecting windows, in electronics as thin-film transistors and light-emitting diodes, etc. Zinc oxide mainly crystallizes in two forms, hexagonal wurtzite [53] and cubic zincblende structures. The wurtzite is most commonly found structure as it is stable at ambient conditions. The Zincblende form is achieved by growing ZnO on substrates having cubic lattice structure. In both cases, the zinc and oxide centers are tetrahedral, the most characteristic geometry for Zn(II). ZnO converts to the rocksalt structure at relatively high pressures of about 10 GPa [52]. The important structure parameters of ZnO are presented in Table 2.2. Unit cell structures for ZnO are shown in fig. 2.17.

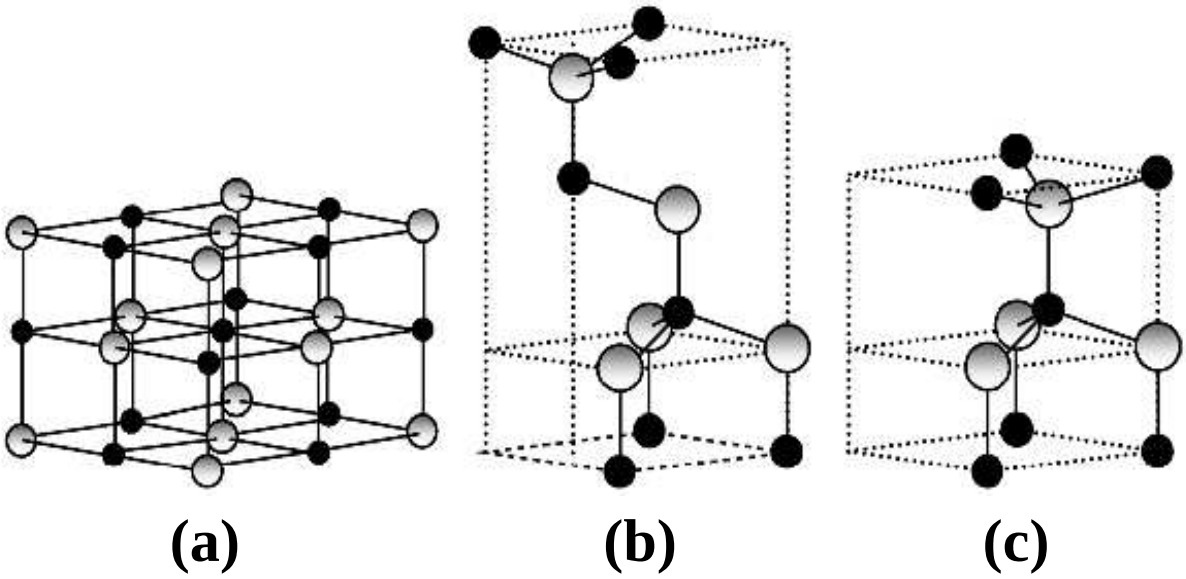

Figure 2.17: Crystal structures of ZnO :(a) cubic rocksalt (b) cubic zinc blende and (c) hexagonal wurtzite. Shaded gray and black spheres denote O and Zn atoms, respectively. (from ref [54])

Table 2.2: Lattice parameters of ZnO crystal

	Wurtzite ([54, 55])	Rockslat ([54, 55])	Zinc Blende ([54, 55])
a($\mathring{A}$)	3.258	4.271	4.62
b($\mathring{A}$)	3.258	3.258	3.258
c($\mathring{A}$)	5.220	3.258	3.258
Volume[a]	23.81	19.60	24.551
Crys. System	Hexagonal	Cubic	Cubic
Point Group	6mm	4/m -32/m	$\bar{4}$3m
Space Group	P63mc	Fm3m	F$\bar{4}$3m
Bandgap (eV)	3.4	4.27	2.7

a, b, c are the lattice parameters of the unit cell
[a] Volume is in $\mathring{A}^3$ per ZnO formula unit.

2.3.3 Nickel oxide (NiO) :

Nickel oxide (NiO) is a versatile wide band gap semiconducting material. It adopts the NaCl structure, with octahedral Ni(II) and O^{2-} sites. The commonly known crystal structure of NiO is the cubic rock salt structure with lattice spacing of 4.177 $\mathring{A}$. In its pure state, NiO is an insulator, however, due to the defects and Ni^{2+} vacancies NiO displays semi-conductive properties. It demonstrates a variety of unique optical, magnetic, chemical and electrical properties.

These enhance its potential for usage in applications related to sensors, battery electrode, electrochromic film, magnetic data storage material, ceramic material, catalyst etc [56, 57]. Nickel oxide has Fm3m space group symmetry and bandgap of 4.3 eV. The unit cell, cubic rock salt crystal structure, of NiO is shown in fig. 2.18.

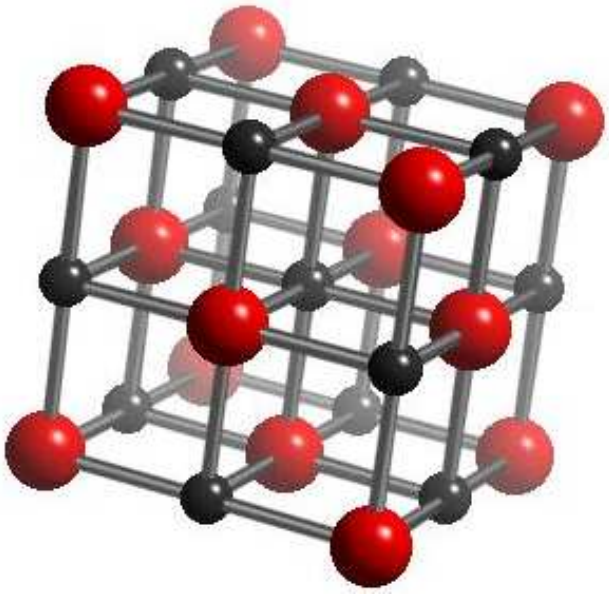

Figure 2.18: Cubic rock salt crystal structure, of NiO. Shaded red and black spheres denote O and Ni atoms, respectively. (from ref [58])

Bibliography

[1] D. Kanjilal, G. O. Rodrigues, U. K. Rao, C. P. Safvan, and A. Roy, Ind. Jour. Pure Appl. Phys. **39**, 25 (2001).

[2] R. Geller, Electron Cyclotron Resonance Ion Sources and ECR Plasmas (IOP, Bristol, 1996).

[3] A. G. Drentje, Rev. Sci. Instrum. **74**, 2631 (2003).

[4] K. Byrappa, and M. Yoshimura, Handbook of Hydrothermal Technology (Norwich, New York: Noyes Publications, 2001), Chapter 2: History of Hydrothermal Technology.

[5] R. A. Laudise, Chem. Eng. News, **65**, 30 (1987).

[6] X. Xia, Y. Zhang, D. Chao, C. Guan, Y. Zhang, L. Li, X. Ge, I. M. Bacho, J. Tu, and H. J. Fan, Nanoscale **6**, 5008 (2014).

[7] A. Einstein, Ann. Phys. **31**, 132 (1905).

[8] K. Siegbahn, and K. I. Edvarson, Al, Nuclear Physics **1**, 137 (1956).

[9] K. Siegbahn, Electron Spectroscopy for Atoms, Molecules and Condensed Matter, Nobel Lecture, December 8 (1981).

[10] R. W. Paynter, Surf. Inte. anal. **3**, 186 (1981).

[11] G. Binning, and H. Rohrer, Helv. Phys. Acta **55**, 726 (1982).

[12] G. Binning, H. Rohrer, C. Gerber, and E.Weibel, Phys. Rev. Lett. **50**, 120 (1983).

[13] G. Binnig, C. F. Quate, and C. Gerber, Phys. Rev. Lett. **56**, 930 (1986).

[14] B. Lambart, Annalen der Physik und Chemie **86**, 78 (1852).

[15] N. Soltani, E. Saion, M. Z. Hussein, M. Erfani, A.Abedini, G. Bahmanrokh, M. Navasery, and P. Vaziri, Int. J. Mol. Sci.**13**, 12242 (2012).

[16] M. Hoffman, S. Martin, W. Choi, and D. Bahnemann, Chem. Rev. **95**, 69 (1995).

[17] J. Tauc, Materials Research Bulletin **3**, 37 (1968).

[18] E. A. Davis, and N. F. Mott, Philosophical Magazine A **22**, 903 (1970).

[19] W. L. Bragg, Nature **90**, 410 (1912).

[20] Magnetic Property Measurement System SQUID VSM Users Manual, Part Number 1500-100, C0

[21] V. E. Henrich, and P. A. Cox, Cambridge University Press, Cambridge (1996).

[22] F. A. Cotton, G. Wilkinson, and P. L. Gaus, Basic Inorganic Chemistry, 3 ed. (John Wiley and Sons Ltd., Chichester, New York) (1995).

[23] S. Elliott, The Physics And Chemistry Of Solids (John Wiley and Sons Ltd., Chichester, New York) (1998).

[24] X. Chen, and S. S. Mao, Chem. Rev. **107**, 2891 (2007).

[25] S. Majumder, D. Paramanik, V. Solanki, B. P. Bag, and S. Varma, Appl. Phys. Lett. **98**, 053105 (2011).

[26] V. Solanki, S. Majumder, I. Mishra, P. Dash, C. Singh, D. Kanjilal, and S. Varma, J. Appl. Phys. **115**, 124306 (2014).

[27] M. Winter, WebElements: The Periodic Table on the http://www.webelements.com/webelements/scholar/elements/titanium/history.html.

[28] D. C. Cronemeyer, Phys. Rev. **113**, 1222 (1956).

[29] M. Haruta, N. Yamada, T. Kobayashi, and S. Iijima, J. Catal. **115**, 301 (1989).

[30] C. R. Henry, Surf. Sci. Rep. **31**, 235 (1998).

[31] M. Haruta, CATTECH **6**, 102 (2002).

[32] C. C. Chusuei, X. Lai, K. Luo, and D. Goodman, Topics Catal. **14**, 71 (2001).

[33] M. Gratzel, Nature **414**, 338 (2001).

[34] N. Serpone, and E. Pelizzetti, Photocatalysis - Fundamentals and Applications, (John Wiley Sons, New York (1989).

[35] B. Kasemo, and J. Gold, Adv. Dent. Res. **13**, 8 (1999).

[36] S. Majumder, I. Mishra, U. Subudhi, and S. Varma, Appl. Phys. Lett. **103**, 063103 (2013).

[37] A. Fujishima, T. N. Rao, and A. D. Tryk, J. Photochem. Photobiol. C: Photochem. Rev. **1**, 1 (2000).

[38] W. Gopel, G. Rocker, and R. Feierabend, Phys. Rev. B **28**, 3427 (1983).

[39] H. K. Pulker, G. Paesold, and E. Ritter, Appl. Opt. **15**, 2986 (1976).

[40] A. Heller, Acc. Chem. Res. **28**, 503 (1995).

[41] U. Gesenhues, and T. Rentschler, J. sol. sta. chem. **143**, 210 (1999).

[42] NASA, National Aeronautics and Space Administration, http://www.nasa.gov..

[43] http://www.geocities.jp/ohba_lab_ob_page/structure6.html.

[44] M. Addamo, M. Bellardita, A. Di Paola, and L. Palmisano, Chem. Commun. 4943 (2006).

[45] A. Navrotsky, Chem. Phys. Chem. **12**, 2207 (2011).

[46] S. Chen, and A. Navrotsky, Am. Mineral. **95**, 112 (2010).

[47] A. A. Levchenko, G. Li, J. Boerio-Goates, B. F. Woodfield, and A. Navrotsky, Chem. Mater. **18**, 6324 (2006).

[48] R. J. Swope, J. R. Smyth, and A. C Larson, Am. Mineral. **80**, 448 (1995).

[49] V. Swamy, J. D. Gale, L. S. Dubrovinsky, J. Phy. Chem. Sol. **62**, 887 (2001).

[50] M. Horn, C. F. Schwerdtfeger, and E. P. Meagher, Z.Kristallogr. **136**, 273 (1972).

[51] E. P. Meagher, and G. A Lager, Can. Mineral. **17**, 77 (1979).

[52] U. $\ddot{O}$zg$\ddot{u}$r, Y. I. Alivov, C. Liu, A. Teke, M. A. Reshchikov, S. Dogan, V. Avrutin, S. J. Cho, and H. Morkoc, J. Appl. Phys. **98**, 041301 (2005).

[53] J. L. G. Fierro, Zinc Oxide: Fundamentals, Materials and Device Technology. Hadis Morkoc and Umit Ozgur, WILEY-VCH Verlag GmbH and Co. KGaA, Weinheim.

[54] U. $\ddot{O}$zg$\ddot{u}$r, Ya. I. Alivov, C. Liu, A. Teke, M. A. Reshchikov, S. Dogan, V. Avrutin, S. J. Cho, and H. Morkoc, J. Appl. Phy. **98**, 041301 (2005).

[55] Zinc Oxide: Fundamentals, Materials and Device Technology. Hadis Morkoc and Umit Ozgur, WILEY-VCH Verlag GmbH and Co. KGaA, Weinheim.

[56] D. S. Jeong, R. Thomas, R. S. Katiyar, J. F. Scott, H. Kohlstedt, A. Petraru, and C. S. Hwang, Rep. Prog. Phys. **75**, 076502 (2012).

[57] P. Horaka, V. Bejsovec, V. Lavrentiev, J. Vacik, M. Vrnata, and J. Khun, Nanocon (2013).

[58] www.webelements.com/compounds/nickel/nickel_oxide.html

Chapter 3

Enhanced anomalous Photo-absorption from TiO_2 nanostructures

3.1 Introduction :

Titanium dioxide (TiO_2) is a wide band gap semiconductor which displays promising properties in a variety of applications like photocatalysis, water splitting, photovoltaic cells, self-cleaning surfaces, dye-sensitized solar cells, environmental remediation [1–3] as well as in bioimplants due to its biocompatible nature [4]. With enormous potential in engineering and technology, the performance of TiO_2-based devices is affected not only by its electronic structure, but also by surface characteristics at nano-scale, as well as number of defects. The bandgap of TiO_2 is in UV regime and for photovoltaic related applications, an enhanced absorbance, especially in the visible regime for increased solar spectrum utilization, becomes important. Defects, here, can play a crucial role by controlling the carrier recombination processes [5].

Enormous research efforts are being undertaken for enhancing photo absorbance in TiO_2 through techniques of doping [6–8], dye sensitization [9] as well as synthesis into nanocrystals [7] and thin films [10]. Many of these methods involve chemical modification of the material with organic dyes being chemically unstable and dopant incorporation usually demanding high temperature treatments for substitutional incorporation. Photo-absorption and bandgap modifications in nanostructured TiO_2 are also currently active areas of research but usually their fabrication route and formation involve several stages [11]. In this respect, nano- scale structures, fabricated by ion beam sputtering technique, hold definite promise as the surface structures can be produced in a single technological step. Moreover, with controlled parameters, the surfaces can spontaneously develop self assembled closed packed nanostructures and display a variety of patterns as has been demonstrated on several surfaces [12–14]. Compe-

tition between the erosive processes, guided by curvature dependent sputtering, and diffusion dominated surface smoothening [15] as well as incompressible nature of the solid mass flow inside amorphous layers [16–19] controls the evolution of the nanostructures and their patterns on the surfaces .

This chapter discusses the fabrication of two dimensional rutile TiO_2 nanostructures through ion beam sputtering of TiO_2 (110) surfaces. The studies, here, have been performed as a function of ion fluence with the surfaces displaying patterns of nanostructures. The results show that the photo- absorption response depends, in a complex fashion, on the size of nanostructures. Contrary to the expectation, not the smallest sized nanostructures, but the smallest nanostructures conjugated with the largest oxygen vacancy states, display highest photo- absorbance. The systematic studies presented here display a composite role of nanostructure size and oxygen vacancies for enhanced photo absorption response accompanied with decreased recombination of charge carriers. By tuning the parameters to enhance vacancy creation towards critical concentration, facilitating charge separation process, combined with small nanostructure size in the absence of any dopant material, as exhibited here, can lead to significant impact in heterogeneous photocatalysis process of TiO_2 based devices.

3.2 Experimental :

Rutile TiO_2 single crystals (commercially purchased from MaTecK) have been irradiated with 60 keV Ar^+ ions at an incident angle of 60°, with respect to surface normal, at room temperature. The Ar ion beam, with a flux of 1.8 $\times 10^{14}$ ions/cm^2·s, was taken from an ECR source. The TiO_2 crystals were irradiated at a variety of fluences varying from 5×10^{15} to 5×10^{17}ions/cm^2. The surface morphology of the pristine and ion irradiated samples has been investigated by Scanning Probe Microscope (SPM), Nanoscope V (from Bruker), in tapping mode (vertical and horizontal resolutions are 0.01 nm and 1 nm, respectively). Core level studies have been undertaken on a VG X-ray photoelectron Spectroscopy (XPS) system having an instrumental resolution of 0.9 eV. The XPS system, operated under UHV conditions, has a dual Mg-Al anode and a Hemispherical analyzer. The spectra reported here have been obtained with Mg Kα radiation at a pass energy of 20 eV. The emission angle of the photoelectrons was kept at 30° with respect to the surface normal. Optical (UV-Vis) absorption and Photoluminescence (PL) studies were performed using a Shimadzu Spectrophotometer and a Horiba Jobin-Yvon system

(with 325 nm He-Cd laser excitation source), respectively.

3.3 Results and Discussions :

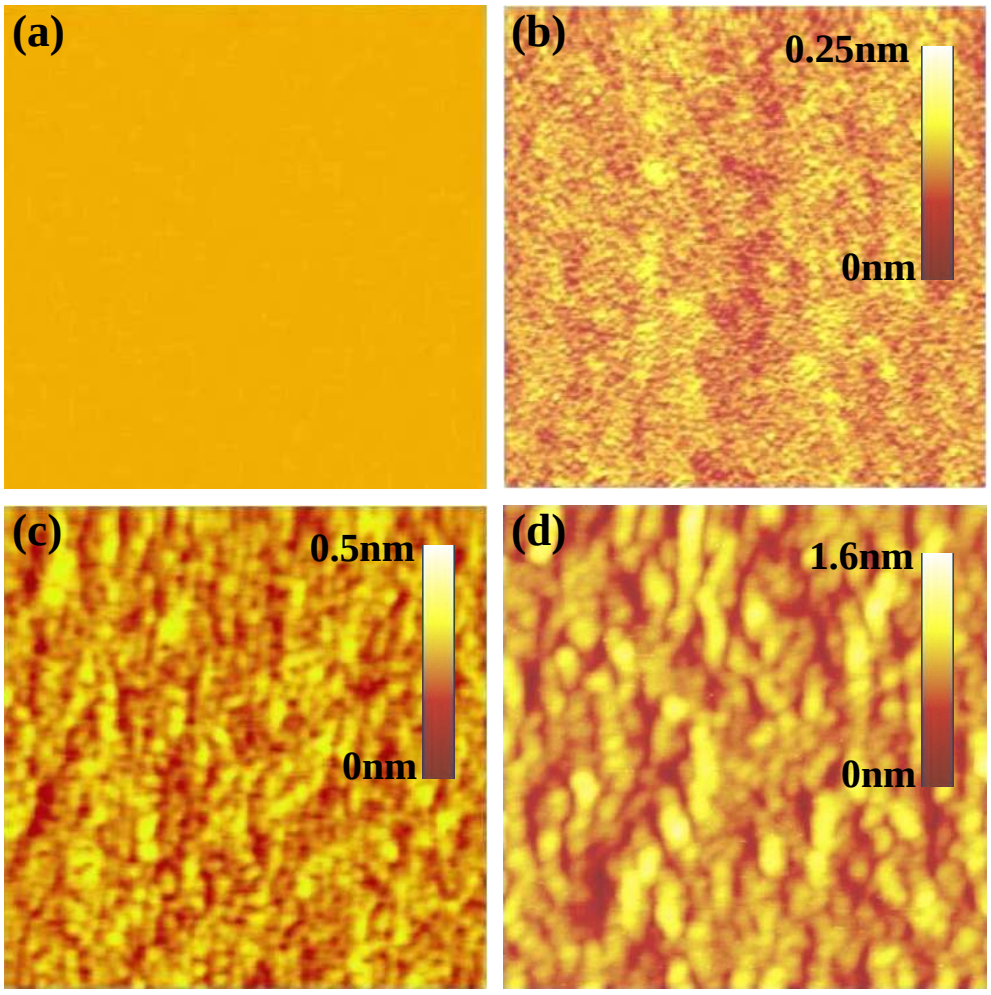

Figure 3.1: SPM images (500 x 500 nm^2) of (a) pristine TiO_2(110) and after irradiation with fluences of (b) 5×10^{15}, (c) 1×10^{16} and (d) 1×10^{17} ions/cm^2.

Evolution of the surface morphology of TiO_2 (110) surfaces, after ion irradiation, is displayed in fig. 3.1. Although the pristine sample displays a smooth surface morphology, it gets decorated with a large density ($\sim$30 x 10^{11} cm^{-2}) of 2-dimensional nanostructures, having diameter of $\sim$5 nm and height of $\sim$0.15 nm, after an irradiation with a fluence of 5×10^{15} ions/cm^2(see fig. 3.1 (b)). At this stage, there are no visible correlations among the nanostructures. For crystalline substrates, the main effect of the ion impact is to produce adatom and vacancy clusters [20]. At higher fluences (fig. 3.1 (c, d)), growth of nanostructures, formation

of clusters of nanostructures along with the development of some wave like ripple patterns are observed. Figure 3.2 displays high resolution SPM images from these surfaces irradiated at high fluences. These images demonstrate nanostructures to be very distinct and well defined structures at these fluences.

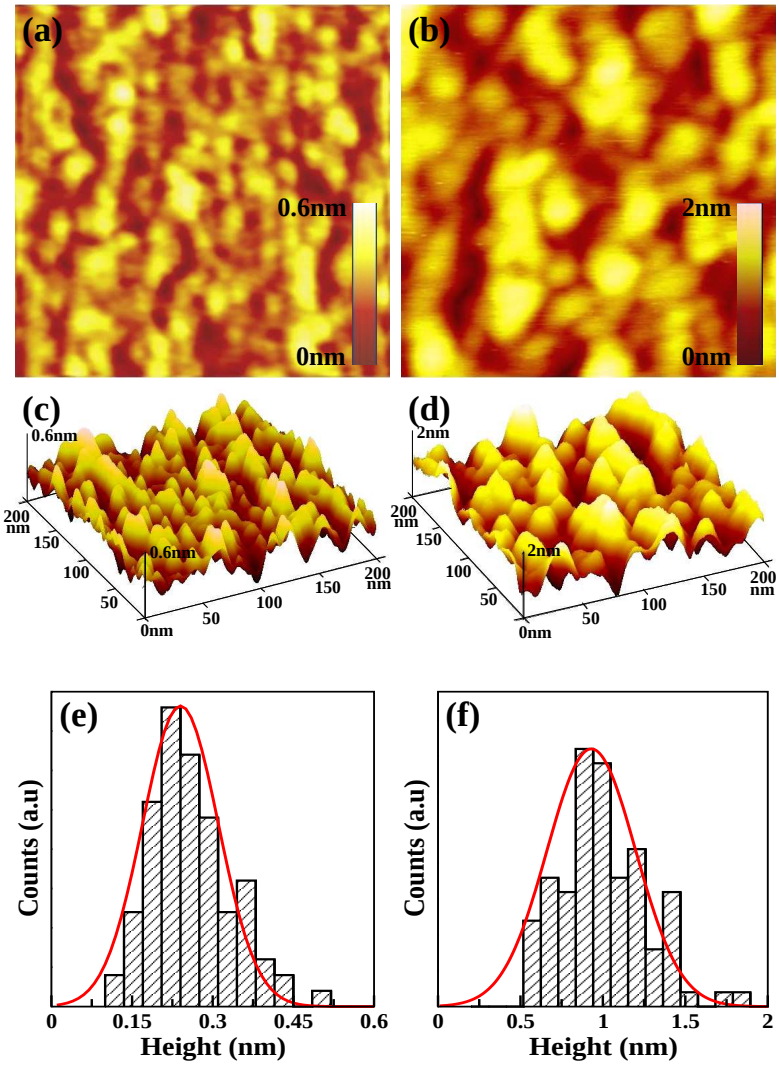

Figure 3.2: High Resolution SPM images (200 x 200 nm^2) in 2-dimensional for TiO_2(110) after irradiation with fluences of (a) 1×10^{16} and (b) 1×10^{17} ions/cm^2. 3-dimensional SPM images (200 x 200 nm^2) after irradiation with fluences of (c) 1×10^{16} and (d) 1×10^{17} ions/cm^2. The height distribution for nanostructures after irradiation with fluences of (e) 1×10^{16} and (f) 1×10^{17} ions/cm^2.

The regular patterns, during ion beam sputtering, are produced through surface instability, which can be created through the existence of an energy barrier for diffusing atom at the step edges along with the curvature dependant sputtering. Anisotropic surface diffusion of adatoms

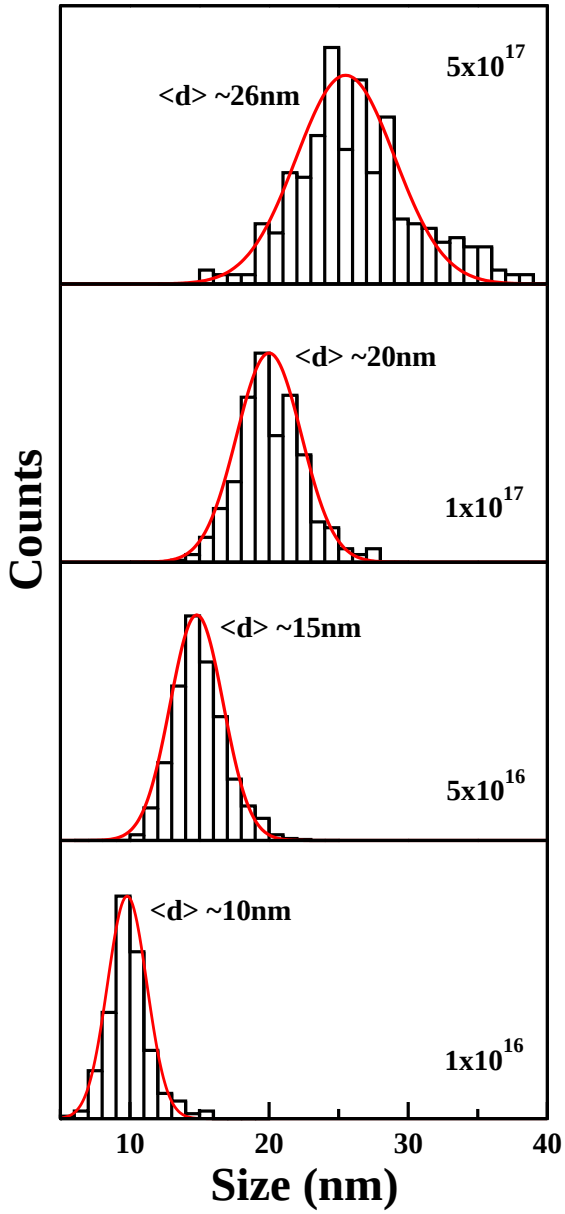

Figure 3.3: The lateral diameter distribution of 2-dimensional nanostructures on TiO_2(110) surfaces after irradiation at various fluences. Mean lateral diameter, $\langle d \rangle$, of nanostructures and respective fluences are indicated.

and vacancies as well as the ion beam related erosion can be responsible for the nanostructured patterns observed here. Activation of the terrace diffusion barrier and Ehrlich Schwoebel barrier may create surface instability [20] leading to ripple formation. Coarsening of the nanostructures becomes active through the processes of diffusion. Clusters however form by the coalescence of adatom nanostructures. The diffusion process is also governed by inter-layer mass transport processes. The lateral- diameter distribution of the 2d nanostructures, on ion- irradiated TiO_2

surfaces, is displayed in fig. 3.3. Although the distribution broadens with fluence, a consistent increase in the average lateral diameter, $\langle d \rangle$, for nanostructures is observed. Furthermore, these nanostructures are effectively 2- dimensional in nature with their average heights, $\langle h \rangle$, being 0.15, 0.27, 0.5, 0.9, 4.0 nm for the fluences of 5×10^{15}, 1×10^{16}, 5×10^{16}, 1×10^{17} and 5×10^{17} ions/cm^2, respectively. Thus, $\frac{\langle d \rangle}{\langle h \rangle}$ ratio, for these nanostructures, is observed to be 20-40 at all the fluences except the highest fluence (5×10^{17} ions/cm^2), where this ratio is observed to be about 7.

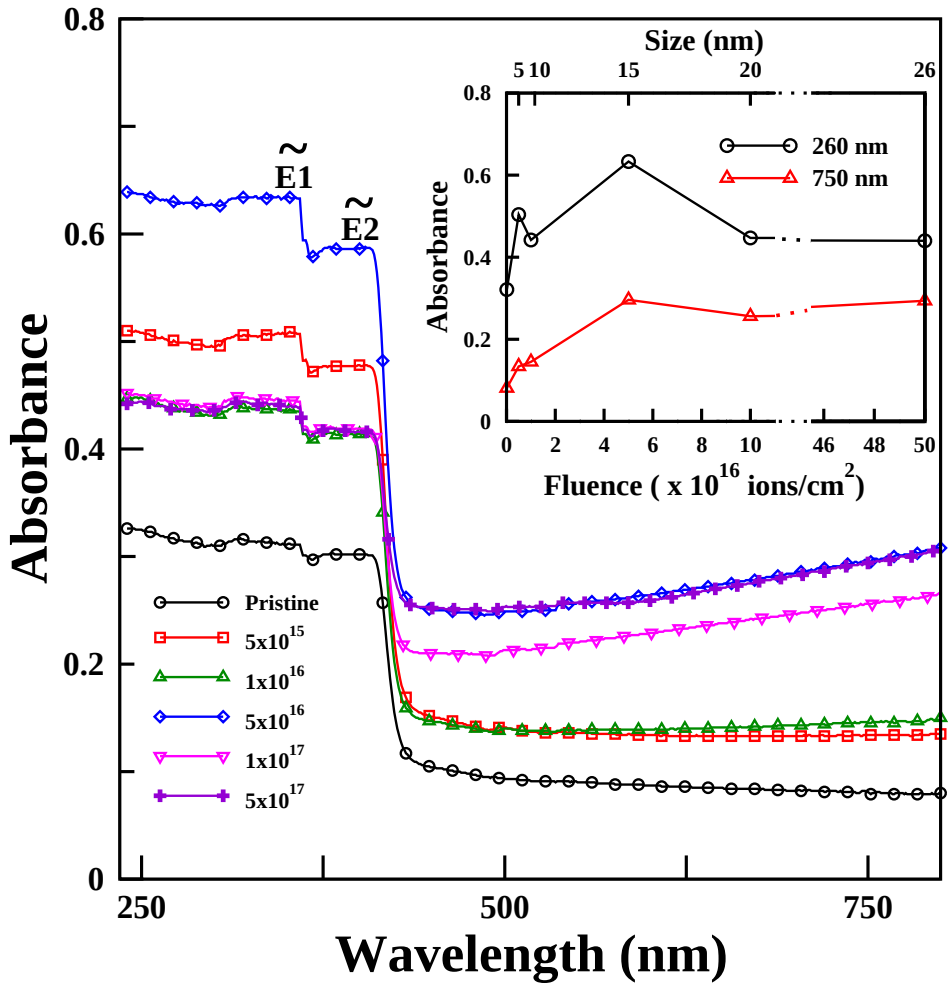

Figure 3.4: UV-Vis absorption spectra are shown for pristine TiO_2(110) as well as after its irradiation at various fluences. Inset shows the photo- absorbance measured at two specific wavelengths, in UV(260 nm) regime (○) and Visible(750 nm) regime (△), as a function of ion fluence (bottom scale) as well as nanostructure size (top scale).

Optical absorption spectra from ion irradiated and pristine TiO_2 surfaces are shown in fig. 3.4 and display two absorption band edges, $\tilde{E}1$ and $\tilde{E}2$, with the former being related

to the TiO_2 bandgap transition [21, 22], from O(2p) derived valence band to Ti(3d) derived conduction band, and the later to transition due to the oxygen vacancy states [14, 23]. A significant intensification of absorbance, compared to pristine, is demonstrated at all the fluences. Fabrication of 2-dimensional nanostructures, after ion sputtering, on the TiO_2 surfaces, is the primary reason for this increase [24, 25]. Surprisingly, the maximally absorbing response is generated by $\langle d \rangle$ ∼15 nm ($\langle h \rangle$ ∼0.5 nm) nanostructures created at fluence of 5×10^{16} ions/cm^2.

The inset of fig. 3.4 shows the variation in the photo-absorption intensity, at two different (representative) energies. For both, UV(260 nm) as well as Visible(750 nm) regimes, an enhancement of absorption at all fluences, compared to the pristine, can be observed. Although the behaviour of absorbance is overall similar in both the regimes, the overall absorbance is higher in UV region, as expected for TiO_2.

Here, an anomalous fact is also noticed in that the largest absorption is displayed by the $\langle d \rangle \sim 15$ nm ($\langle h \rangle \sim 0.5$ nm) nanostructures created at the fluence of 5×10^{16} ions/cm^2 in both UV as well as Visible(Vis) regimes (see fig. 3.4 and its inset). Smaller nanostructures fabricated at lower fluences would be, conventionally, expected to be candidates to exhibit highest absorbance due to their higher surface area. Surprisingly, however, the smaller TiO_2 nanostructures with $\langle d \rangle$ of 5 nm($\langle h \rangle \sim 0.15$nm) and 10 nm ($\langle h \rangle \sim 0.27$ nm) , created here, respectively, at the fluences of 5×10^{15} and 1×10^{16} ions/cm^2, display significantly lower photo-absorbance. With the highest absorption response observed here for nanostructures with $\langle d \rangle$ ∼15 nm and $\langle h \rangle \sim 0.5$ nm, results presented here reflect a complex dependence of photo- absorption on the size of nanostructures.

Core level XPS spectra, of Ti(2p) region, are shown in fig. 3.5, for pristine as well as ion irradiated TiO_2 surfaces. For the pristine surface, two prominent features representing the $Ti2p_{3/2}$ and $Ti2p_{1/2}$ states are observed at 458.4 and 464.1 eV, respectively (fig. 3.5(a)). Both these components are associated with the Ti^{4+} state of the pristine sample. In the lower binding energy regions of each of these features, two very weak Ti^{3+} and Ti^{2+} components, representing the existence of very small traces of oxygen vacancies on the pristine TiO_2 surface, are observed (see fig. 3.5(a)). The intensities of both these features, Ti^{3+} and Ti^{2+}, however become appreciable at higher fluences, suggesting creation of significant oxygen vacancies with the formation of species like Ti_2O_3 and TiO [26, 27].

The ion sputtering of the multi-component surface, as discussed in our earlier studies [4, 14, 28], can cause preferential sputtering of TiO_2 surface and formation of oxygen vacancy, with

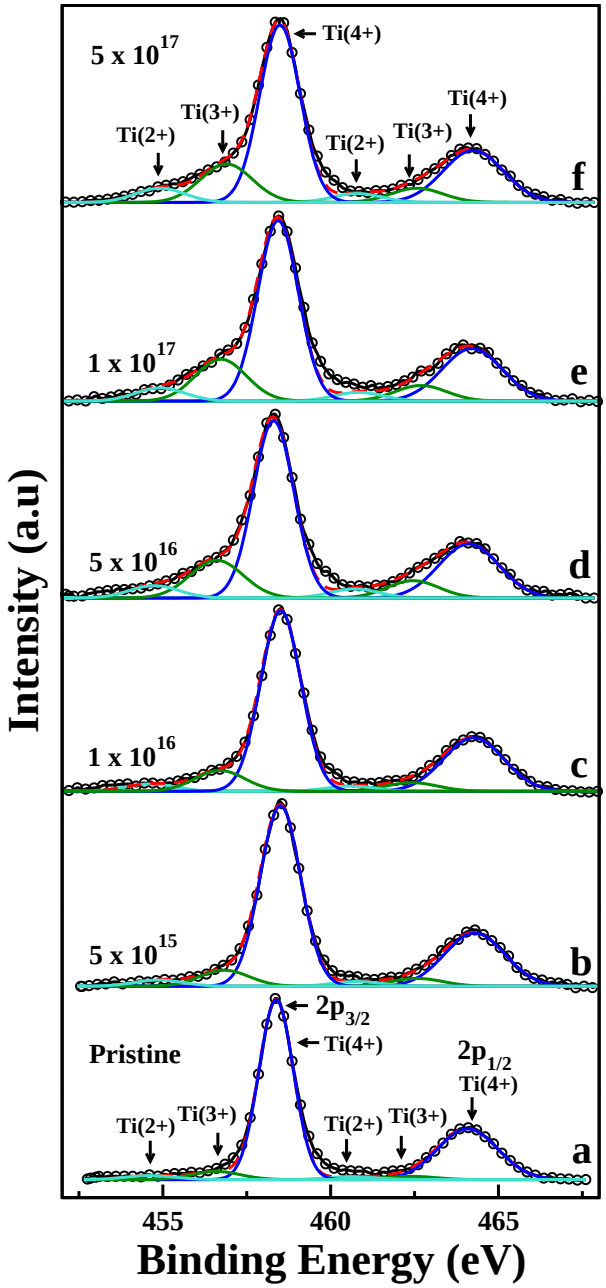

Figure 3.5: XPS of Ti(2p) core level for pristine TiO_2(110) as well as after ion irradiation at various fluences. Peak fitted components for Ti^{4+}, Ti^{3+} and Ti^{2+} states are also shown.

the two associated electrons getting transferred to the empty 3d orbitals of the neighboring Ti atom forming two Ti^{3+} sites. Ti-rich zones, thus formed, can promote nucleation of self assembled nanodots; in a fashion similar to the scenario presented for the creation of In -rich nano clusters on InP surfaces after ion irradiation [12, 29]. Photoelectron intensity in XPS exhibits an exponentially decaying behaviour as a function of depth and for the kinetic energies

of relevance, here, the mean free path for the photo-electrons (probing depth) is about 1 nm. With $\langle h \rangle$ of nanostructures being $\leq$ 1nm for most of the fluences, XPS results here can be attributed to be from the nanostructures. For the tallest 2d nanostructure ($\langle h \rangle \sim$ 4nm) created at the fluence of 5×10^{17} ions/cm^2, also, the XPS signal is predominantly from the nanostructure.

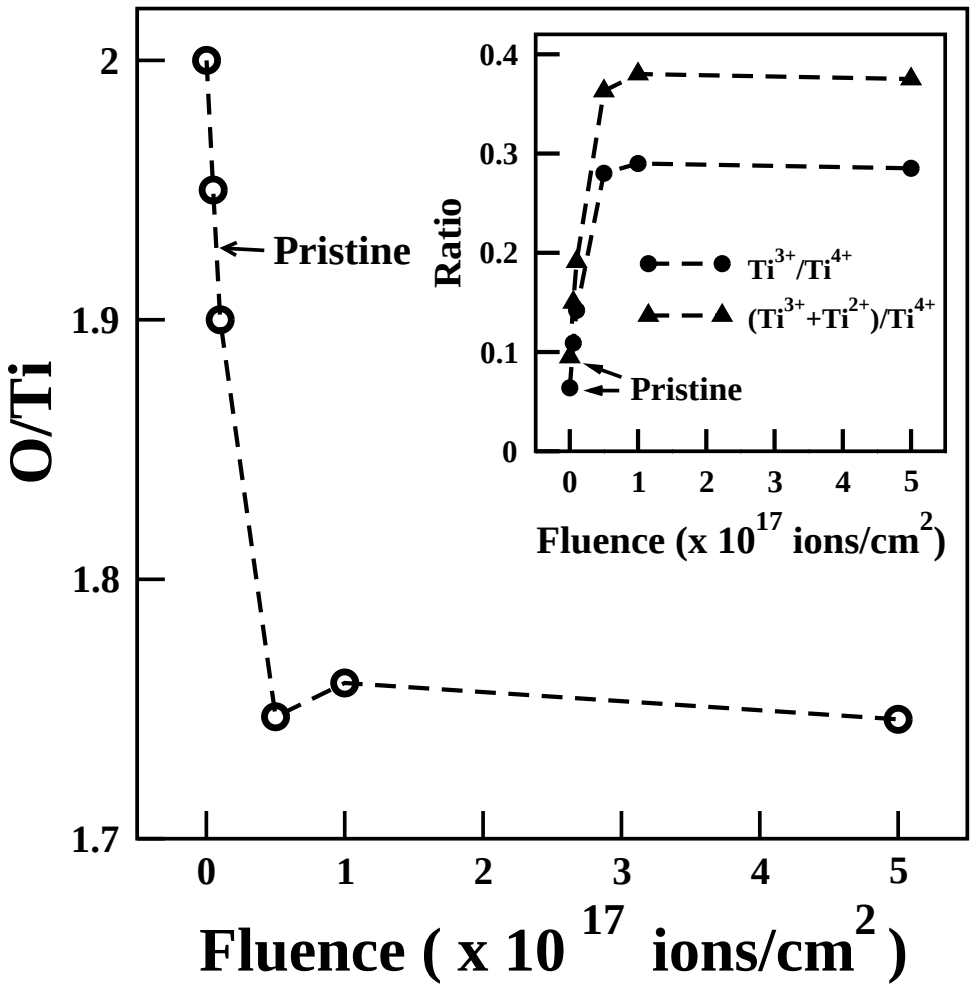

Figure 3.6: Intensity ratio of O(2p) to Ti(2p) states is shown as a function of ion fluence. Inset displays the intensity ratio of Ti^{3+} to Ti^{4+} states as well as intensity ratio of Ti^{3+}+Ti^{2+} to Ti^{4+} states as a function of ion fluence.

Figure 3.6 displays the ratio of the total oxygen to Ti species on the pristine as well as ion irradiated TiO_2 surfaces. A drastic decrease in the (O/Ti) ratio up to the fluence of 5×10^{16} ions/cm^2 is accompanied by a saturation at higher fluences. Remarkably, during this saturation regime, the nanostructures are continuing to grow (fig. 3.1-3.3). This growth, however, is not accompanied by any further creation of oxygen vacancies (Ti^{3+}) which appear to also saturate at 5×10^{16} ions/cm^2. The inset of fig. 3.6 displays the ratio of intensities of Ti^{3+} to Ti^{4+} states

(using results of fig. 3.5); as well as the ratio of combined oxygen vacancy states, Ti^{3+} and Ti^{2+}, to Ti^{4+} as a function of ion fluence. Interestingly, a drastic increase, in both these ratios, is observed up to the fluence of 5×10^{16} ions/cm^2 but a saturation beyond that. Once saturation occurs, surfaces consist of nearly 40% oxygen vacancies (Ti^{3+}, Ti^{2+}) with 30% of them being Ti^{3+} type states (inset fig. 3.6). The present study is the first study that investigates the behavior of the vacancy (Ti^{3+} and Ti^{2+}) states as a function of ion fluence. Remarkably, the saturation of vacancy states, at high fluences (as seen in fig. 3.6) is a very interesting result which provides a critical limit for enhancing the photocatalytic activity of ion sputtered materials. Furthermore, the results display that ion irradiation, of the TiO_2, promotes the formation of Ti rich zones on the surface, as depicted by lower than pristine O/Ti ratios. These Ti-rich regions essentially become the nucleation centers for the development of the 2- dimensional nanostructures observed in fig.3.1 and 3.2.

Tauc plots shown in fig. 3.7, have been generated using absorbance data (of fig. 3.4) and display bandgap energies, E1 and E2 (related to TiO_2 band gap $\tilde{E}1$ and oxygen vacancy-related band edge $\tilde{E}2$, respectively), for the pristine as well as ion irradiated samples. The direct band gap E1 of 3.18eV, seen here for pristine TiO_2, is slightly higher than the value 3.06 eV reported in literature [22]. After ion irradiation, although E2 (seen at 2.91 eV) does not vary much, the direct band gap (E1) displays a significant variation with fluence (as shown in the inset of fig. 3.7). For all the fluences, E1, is observed to be higher than that for pristine TiO_2, with the largest bandgap, being 3.30 eV, at the fluence of 5×10^{16} ions/cm^2. The blue shift in E1 as observed here, after ion irradiation of TiO_2, can be explained by quantum confinement effects, which according to thermodynamic studies are pronounced for nanostructures of sizes smaller than ~ 27 nm [30,31]. Moreover, the two smallest nanostructures ($\langle d\rangle$ of 5 and 10 nm) exhibit higher $\frac{\langle d\rangle}{\langle h\rangle}$ ratio, compared to those formed at higher fluence, and thus show lower E1 as suggested by the shape dependence studies of TiO_2 nanostructures [32].

For understanding the anomalous behavior of photo- absorption where $\langle d\rangle \sim 15$ nm (with $\langle h\rangle \sim 0.5$ nm) sized nanostructures, and not smaller nanostructures, display highest absorption response (in fig. 3.4), the results of fig. 3.6 become very significant. It is discovered that at the fluence of 5×10^{16} ions/cm^2, the nanostructures created (with $\langle d\rangle \sim 15$ nm, $\langle h\rangle \sim 0.5$ nm), though not smallest, are associated with largest number of, Ti^{3+} and Ti^{2+} type, oxygen vacancies. Although the vacancy states saturate, at higher fluence, the nanostructure size also increase leading to lower absorbance. Similar effect is delineated by smaller sized nanostruc-

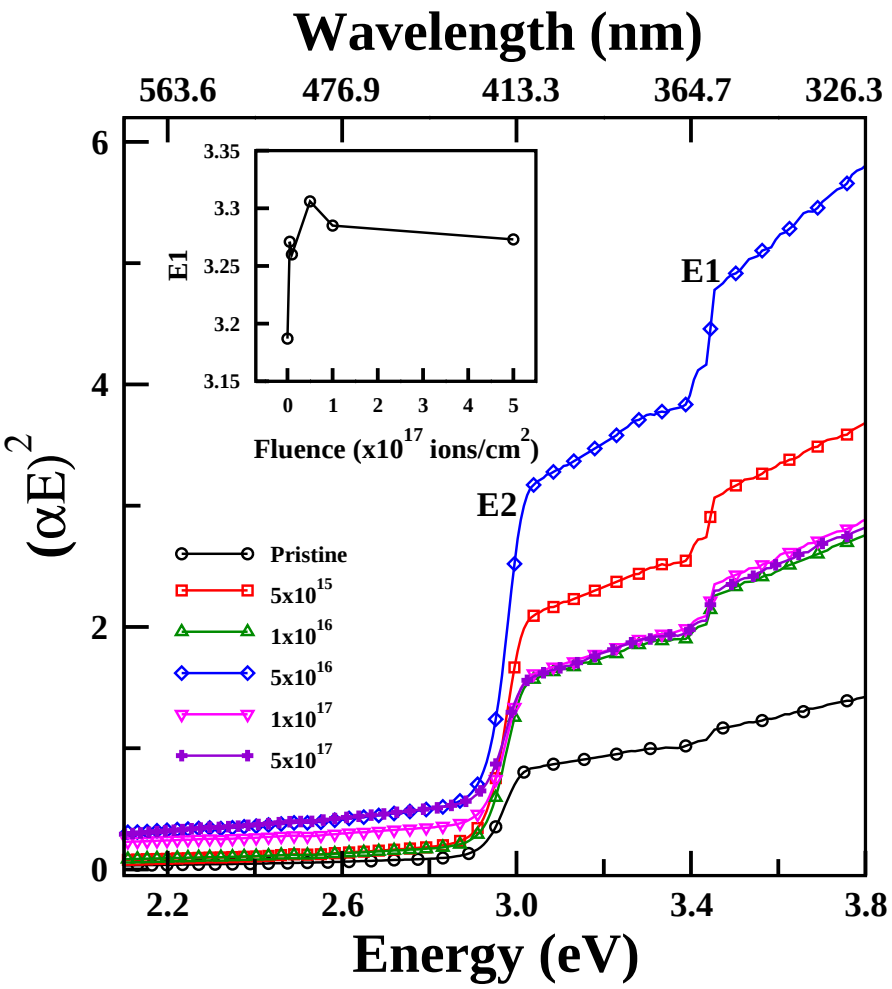

Figure 3.7: Tauc plots are shown for pristine TiO_2(110) as well as after ion irradiation at various fluences. α is the absorption coefficient and E is the photon energy. Inset shows the variation in direct bandgap, E1, as a function of fluence.

ture, at lower fluences, where vacancy states decrease. The results reflect that the conjugation of smallest nano-structures with highest vacancy distribution (observed at $\langle d \rangle \sim 15$ nm, $\langle h \rangle \sim 0.5$ nm) is essential for achieving high absorbance characteristics. Consequently, largest photo-absorption scenario is achieved through a competition between the nanostructure-size and oxygen vacancy sites on it.

Figure 3.8 shows room temperature PL spectra for the pristine as well as ion irradiated TiO_2. Two prominent bands associated with the TiO_2 bandgap emission in the UV region (3.02 eV) and oxygen vacancy related states in the visible region (2.38 eV) are observed [33]. Shallow trap states associated with oxygen vacancies are observed at 2.29 and 2.02 eV [33,34]. Interestingly, a lowering of overall PL intensity for ion irradiated TiO_2, compared to pristine, is

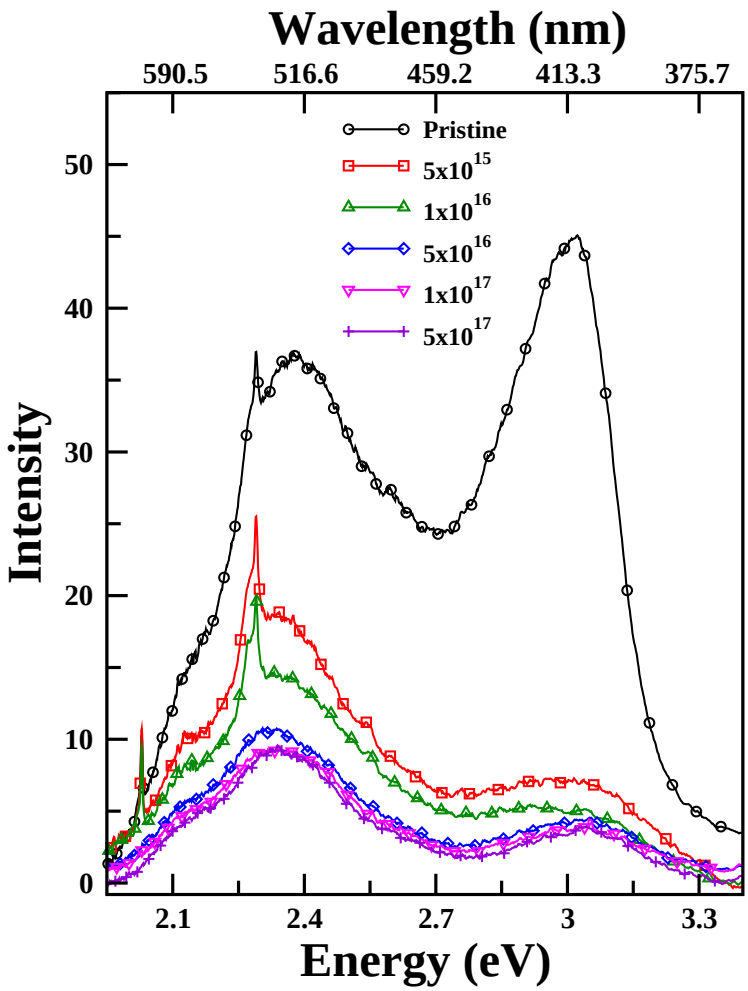

Figure 3.8: Room temperature Photoluminescence spectra for pristine TiO_2(110) as well as after ion irradiation at various fluences.

observed at all fluences suggesting a decrease in the recombination of charge carriers [35, 36] with increasing fluence. This reduction in PL intensity can be attributed to the formation of nanostructures and trapping of charge carriers by the surface Oxygen vacancies which facilitate the charge separation process [35].

Several reports have shown that the surface vacancies can act as adsorption sites where the charge transfer to adsorbed species can prevent the electron - hole recombination [35]. Bulk defects, however, always act as trapping centers leading to e-h recombination [35]. The oxygen vacancies (Ti^{3+} and Ti^{2+}) play a crucial role in the photocatalytic reaction on the TiO_2 surface. The decrease in the PL intensity with ion fluence, as observed in fig. 3.8, reflects towards a decreased e-h recombination process with charge transfer to the surface Oxygen vacancies [36]. In a photocatalytic reaction, the photoexcited electrons and holes are quickly trapped by charge

trapping centers or trap states located near the surface, before being transferred to adsorbed molecules at the interface [14, 35]. These states become the active sites for the capture of photo- induced charge carriers, essentially inhibiting their recombination process. Presence of enhanced vacancy states on the nanostructures can be further utilized to reduce the mean free path of the charge carriers, which gets easily captured at the site. Thus, the presence of oxygen vacancy states effectively decreases the probability of recombination resulting in promotion of light absorbance. The ion irradiation, thus, leads to the fabrication of nanostructures which with their large surface area become potential centers of enhanced light absorbance. Large numbers of oxygen vacancies, created during irradiation, however, are also essential for enhancing the photo- absorbance through the capture of charge carriers prohibiting their recombination.

3.4 Conclusion :

In this chapter, the photo- absorbance response of 2-dimensional nanostructures, created via ion irradiation of TiO_2, has been investigated. Although the nanostructures grow in size, the vacancy states display a critical fluence beyond which they saturate. In an anomalous fashion, the highest absorbing behavior is delineated by nanostructures of $\langle d \rangle \sim 15$ nm (with $\langle h \rangle \sim 0.5$ nm) and not the smaller nanostructures with larger surface areas. With the detailed quantitative investigation of oxygen vacancy states, it is observed that competition between the size of nanostructures and the number of vacancy states controls the photo- absorption properties. The complex relationship between these factors is responsible for the anomalous absorption response, observed here, which can have extensive implications in the area of TiO_2 based photocatalytic devices.

Bibliography

[1] A. Fujishima, and K. Honda, Nature **238**, 37 (1972).

[2] K. Hashimoto, H. Irie, and A.Fujishima, Jpn. J. Appl. Phys. **44**, 8269 (2005).

[3] B. O' Regan, and M. Gratzel, Nature **353**, 737 (1991).

[4] S. Majumder, I. Mishra, U. Subudhi, and S. Varma, Appl. Phy. Lett. **103**, 063103 (2013).

[5] V. E. Henrich, G. Dresselhaus, and H. J. Zeiger, Phy. Rev. Lett. **36**, 1335 (1976).

[6] R. Asahi, T. Morikawa, T. Ohwaki, K. Aoki, and Y. Taga, Science **293**, 269 (2001).

[7] J. Wang, D. N. Tafen, J. P. Lewis, Z. Hong, A. Manivannan, M. Zhi, M. Li, and N. Wu, J. Am. Chem. Soc. **131**, 12290 (2009).

[8] Y. Chen, S. Zhang, Y. Yu, H. Wu, S. Wang, B. Zhu, W. Huang, and S. Wu, J. Dispersion Sci. Technol. **29**, 245 (2008).

[9] N. G. Park, J. van de Lagemaat, and A. J. Frank, J. Phys. Chem. B **104**, 8989 (2000).

[10] S. Tanemura, L. Miao, W. Wunderlich, M. Tanemura, Y. Mori, S. Toh, and K. Kaneko, Sci. Tech. Adv. Mat. **6**, 11 (2005).

[11] W. Wang, B. Gu, L. Liang, W. A. Hamilton, and D. J. Wesolowski, J. Phys. Chem. **108**, 14789, (2004).

[12] F. Frost, A. Schindler, and F. Bigl, Phys. Rev. Lett. **85**, 4116 (2000).

[13] S. Fascko, T. Dekorsy, C. Koerdt, C. Trappe, H. Kurz, A. Vogt, and H. L. Hartnagel, Science **285**, 1551 (1999).

[14] S. Majumder, D. Paramanik, V. Solanki, B. P. Bag, and Shikha Varma, Appl. Phys. Lett. **98**, 053105 (2011).

[15] R. M. Bradley, and J. M. E. Harper, J. Vac. Sci. Technol. A **6**, 2390 (1988).

[16] M. Castro, and R. Cuerno, Appl. Surf. Sci. **258**, 4171 (2012).

[17] M. Castro, R. Gago, L. Vazquez, J. M. Garcia, and R. Cuerno, Phys. Rev. B. **86**, 214107 (2012).

[18] T. Kumar, A. Kumar, D. C. Agarwal, N. P. Lalla, and D. Kanjilal, Nan. Res. Lett. **8**, 336 (2013).

[19] T. Kumar, A. Kumar, N. Lalla, S. Hooda, S. Ojha, S. Verma, and D. Kanjilal, Appl. Surf. Sci. **283**, 417 (2013).

[20] U. Valbusa, C. Boragno, and F. B. de Mongeot, J. Phys. Cond. Mat. **14**, 8153 (2002).

[21] A. K. Rumaiz, J. C. Woicik, E. Cockayne, H. Y. Lin, G. H. Jaffari, and S. I. Shah, Appl. Phys. Lett. **95**, 262111 (2009).

[22] J. Pascual, J. Camassel, and H. Mathieu, Phys. Rev. B. **18**, 5606 (1978).

[23] B. Santara, P. K. Giri, K. Imakita, and M. Fujii, J. Phys. Chem. C **117**, 23402 (2013).

[24] H. Fredriksson, T. Pakizeh, M. Kall, B. Kasemo, and D. Chakarov, J. opt. A : Pure Appl. Opt. **11**, 114022 (2009).

[25] E. G. Goh, X. Xu, and P. G. McCormic, Scripta Materialia **78**, 49 (2014).

[26] S. D. Yoon, Y. Chen, A. Yang, T. L. Goodrich, X. Zuo, D. A. Arena, K. Ziemer, C. Vittoria, and V. G. Harris, J. Phys. Cond. Mat. **18**, L355 (2006).

[27] H. Y. Jeong, J. Y. Lee, S. Y. Choi, and J. W. Kim, Appl. Phys. Lett. **95**, 162108 (2009).

[28] S. Majumder, D. Paramanik, V. Solanki, I. Mishra, D. K. Avasthi, D. Kanjilal, and S. Varma, Appl. Surf. Sci. **258**, 4122 (2012); V. Solanki, S. Majumder, I. Mishra, S. R. Joshi, D. Kanjilal, and S. Varma, Rad. Eff. Def. Solids. **168**, 518 (2013).

[29] D. Paramanik, S. N. Sahu, and S. Varma, J. Phys. D: Appl. Phys. **41**, 125308 (2008).

[30] N. Satoh, T. Nakashima, K. Kamikura, and K. Yamamoto, Nature Nanotech. **3**, 106 (2008).

[31] H. Peng, and J. Li, J. Phys. Chem. C **112**, 20241 (2008).

[32] G. Guisbiers, O. V. Overschelde, and M. Wautelet. Appl. Phys. Lett. **92**, 103121 (2008).

[33] M. Yang, W. Liu, J. L. Sun, and J. L. Zhu, Appl. Phys. Lett. **100**, 043106 (2012).

[34] C. Fabrega, T. Andreu, F.Guell, J. D. Prades, S. Estrade, J. M. Rebled, F. Peiro, and J. R. Morante, Nanotechnology **22**, 235403 (2011).

[35] X. Pan, M. Q. Yang, X. Fu, N. Zhang, and Y. J. Xu, Nanoscale **5**, 3601 (2013).

[36] M. Luo, K. Cheng, W. Weng, C. Song, P. Du, G. Shen, G. Xu, and G. Han, J. Phys. D: Appl. Phys. **42**, 105414 (2009).

Chapter 4

Room Temperature Superparamagnetism in Rutile TiO_2 Quantum Dots Produced via ECR Sputtering

4.1 Introduction :

Titanium dioxide (TiO_2) is a wide band gap semiconductor and displays potential for applications in variety of areas like photovoltaic cells, self-cleaning surfaces, photocatalysis, water splitting, dye-sensitized solar cells [1, 2]. The discovery of room temperature ferromagnetism (FM) in Co-doped anatase TiO_2 thin films [3] provides an excellent stage for utilizing it in oxide based dilute magnetic semiconductor (DMS) technology. This interest has been further reinforced and accentuated by the observation of room temperature FM in undoped TiO_2 [4]. Significant work has been performed to investigate the nature of room temperature FM in doped and undoped TiO_2, for its potential technological applications in spintronics and multiferrroics [3, 5, 6]. Existence of oxygen vacancies and nano-dimensions greatly affect the nature of magnetism and the performance of the oxide based semiconductor devices [4, 6, 7]. Increased surface area associated with nanostructures (NS) significantly control the magnetic nature and properties of the nanophase materials, as compared with their bulk [7]. Specifically, the multi-domain wall structure of bulk crystalline material gets replaced by single domain structure characteristics of nano particles which can lead to new phenomena like superparamagnetism (SPM), spin canting (disordered spin configuration) etc. [6, 7]. The induction of SPM due to the fabrication of smaller sized NS (Quantum dot) has been demonstrated in a variety of materials like Fe_3O_4 [7], Co doped TiO_2 [6, 8], $Cd_{1-x}Cr(II)_xSe$ [9] $BaFe_{12-2x}Ti_xCo_xO_{19}$ [10] etc..

TiO_2 nanostructures have been created by a variety of routes and processes like sol-gel, hydrothermal, solvothermal, direct oxidation, chemical vapor deposition (CVD), physical vapor deposition (PVD), electro deposition, microwave method etc. [11]. Ion beam irradiation technique is an attractive technique for fabricating nanostructures since via this technique self assembled nanostructures are created in a single step process [12–14]. Here, the creation of nanostructures is effectively controlled through a competition between the curvature dependent radiation sputtering that roughens the surface and a variety of smoothening mechanisms.

This chapter discusses the fabrication of self-assembled nanodots on rutile TiO_2(110) surfaces via ion beam sputtering technique. A reduction in optical reflectance as well as a widening of bandgap has been observed for nanodot patterned TiO_2 surfaces. Here we have also investigated the evolution of magnetic behavior of nanostructured surfaces. Interestingly, the surfaces decorated with smallest ($\sim$5 nm) nanostructures, display superparamagnetic (SPM) character. Such SPM behavior has never been earlier observed for undoped oxide semiconductors. Creation of single domain magnetic quantum dots is expected to produce this behavior. Larger TiO_2 nanostructures, created at higher ion fluences, are of ferromagnetic nature. The modification in magnetic behavior has been achieved here in the absence of any doping.

4.2 Experimental :

Rutile TiO_2(110) single crystals (commercially purchased from MaTecK) have been sputtered at room temperature (RT) by utilizing Ar^+ ion beam from Electron Cyclotron Resonance source. Ions having energy and flux of 60 keV and 1.8×10^{14} ions/cm^{2}sec, respectively, were utilized to irradiate TiO_2 surfaces. The irradiation fluences were varied from 5×10^{15} to 5×10^{17} $ions/cm^2$ and the angle of incident was chosen to be 60° from the surface normal. All the experimental parameters as well as irradiation fluences utilized in this chapter are same as those used in chapter 3. Atomic Force Microscope (AFM), Nanoscope V (from Bruker), was utilized in tapping mode to investigate the morphological changes after irradiation. Optical reflectance was measured using UV-Vis Spectrophotometer from Shimadzu and for magnetic measurements, Superconducting Quantum Interference Device (SQUID - VSM) from Quantum Design was utilized.

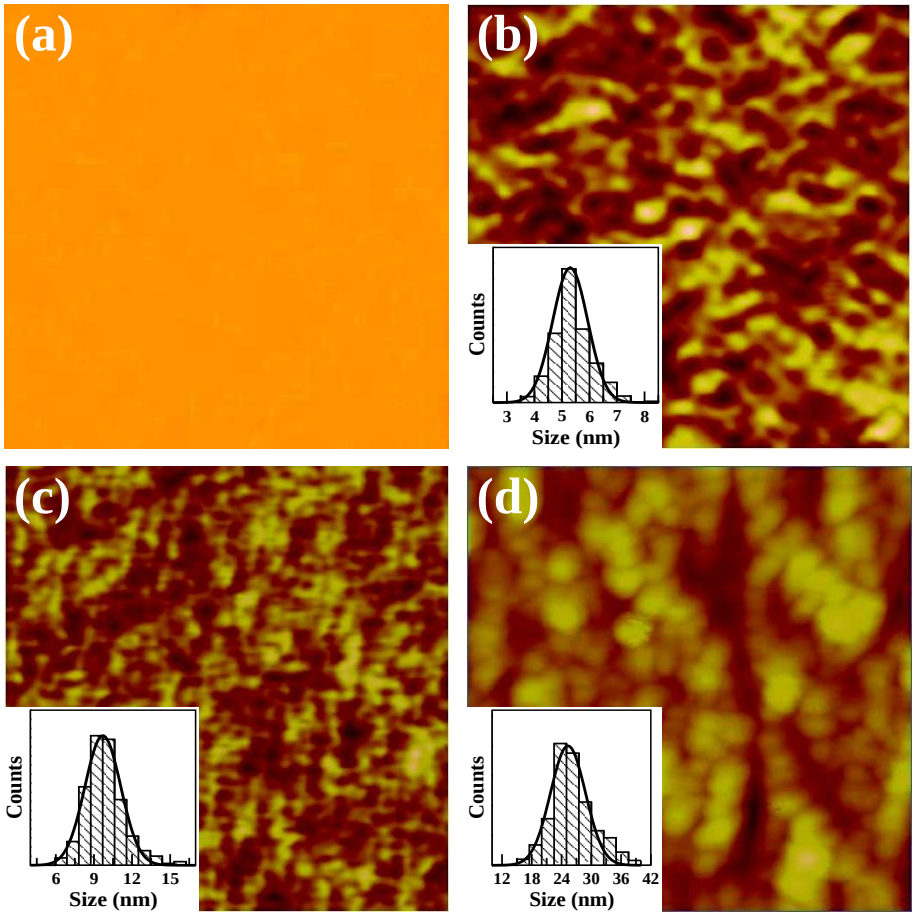

Figure 4.1: AFM images from (a) pristine and surface sputtered with fluence of (b) 5×10^{15}, (c) 1×10^{16} and (d) $5\times10^{17} ions/cm^2$. Images of (a) and (b) are $100 \times 100\ nm^2$ in size whereas images in (c) and (d) are $500 \times 500\ nm^2$ in size. Insets show the size (diameter) distribution of the nanostructures formed after ion irradiation.

4.3 Results and Discussions :

AFM images from pristine and ion irradiated TiO_2 surfaces are shown in fig. 4.1 which depict an evolution of nanostructured surfaces as a function of fluence. The surfaces sputtered with a fluence of $5 \times 10^{15}\ ions/cm^2$ display presence of ∼5 nm sized nanostructures (fig. 4.1 (b)). The NS dimensions are observed to be ∼10 and ∼25 nm for irradiation fluences of 1×10^{16} and $5 \times 10^{17}\ ions/cm^2$, respectively. The size (diameter) distribution for the nanostructures, created on ion-irradiated TiO_2 surfaces, are also presented in fig. 4.1.

Figure 4.2 (a) shows the optical reflectance spectra from pristine and ion irradiated TiO_2 surfaces. It displays two absorption band edges $\tilde{E}1$, related to direct bandgap transition [12,15] and $\tilde{E}2$, due to oxygen vacancy related transitions [12]. A significant decrease of reflectance,

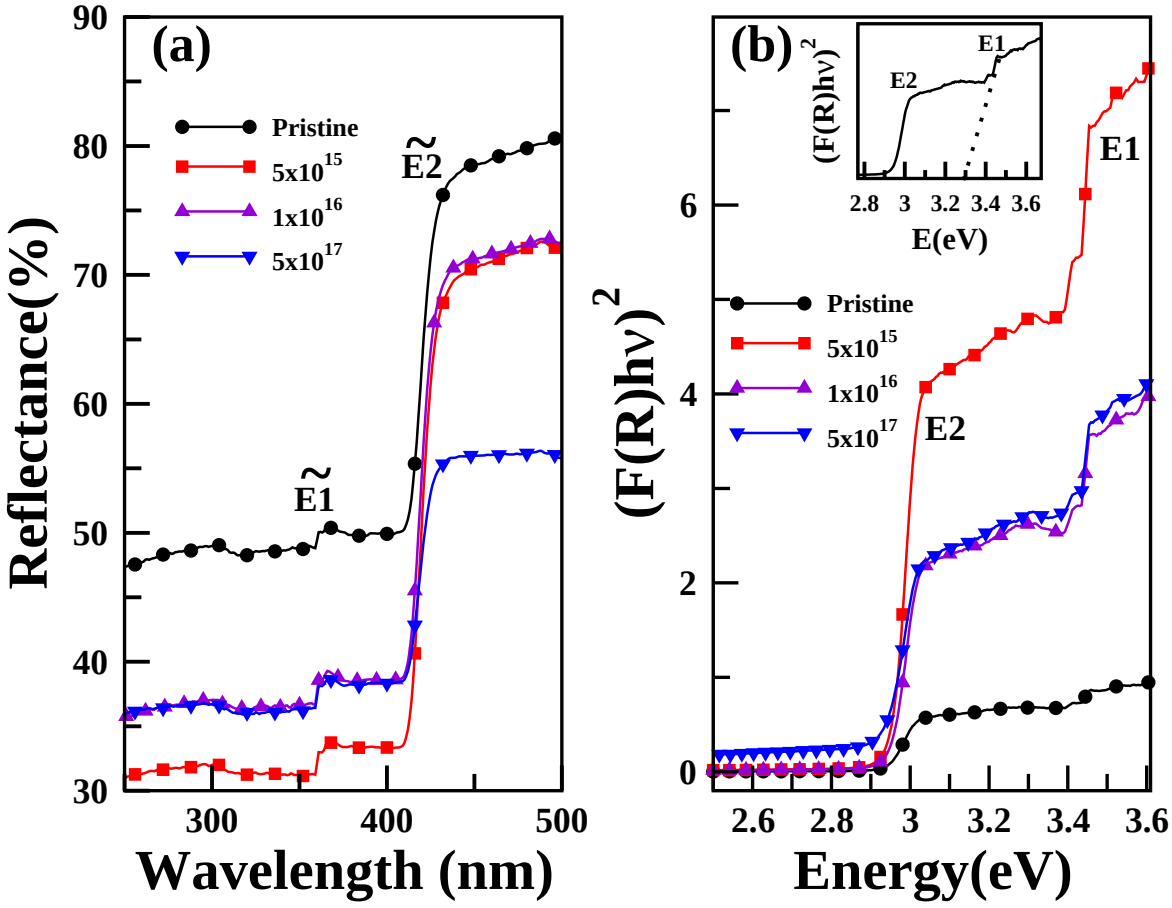

Figure 4.2: Reflectance spectra (a) and transformed Kubelka Munk Function (b) from pristine and surfaces nano patterned at various fluences. Inset in (b) shows the KMF from pristine surface.

compared to pristine surface, is demonstrated for the nanostructured TiO_2 surfaces. Formation of TiO_2 nanostructures, with large surface area having enhanced absorption characteristics [14], may be responsible for this observations.

Kubelka Munk function(KMF) defined as $F(R) = (1-R)^2/2R$ for a given reflectance, R, provides important information about electronic transitions and bandgap energies [16]. This function can be utilized to relate incident photon energy ($h\nu$) and the optical bandgap energy (E_g) via $[F(R)h\nu]^{1/n} = A(h\nu - E_g)$ and is shown in fig. 4.2 (b) for pristine as well as nanostructured TiO_2 surfaces. Here, A is the transition probability constant and n is an index which is $1/2$ for direct transition. Pristine surface displays a direct band edge $E1$ and a defect related edge $E2$ at $3.30\ eV$ and $2.95\ eV$, respectively. The value E1 is slightly higher than the value ($3.06\ eV$) reported in literature [15]. After irradiation, a significant widening, 70 meV, in E1,

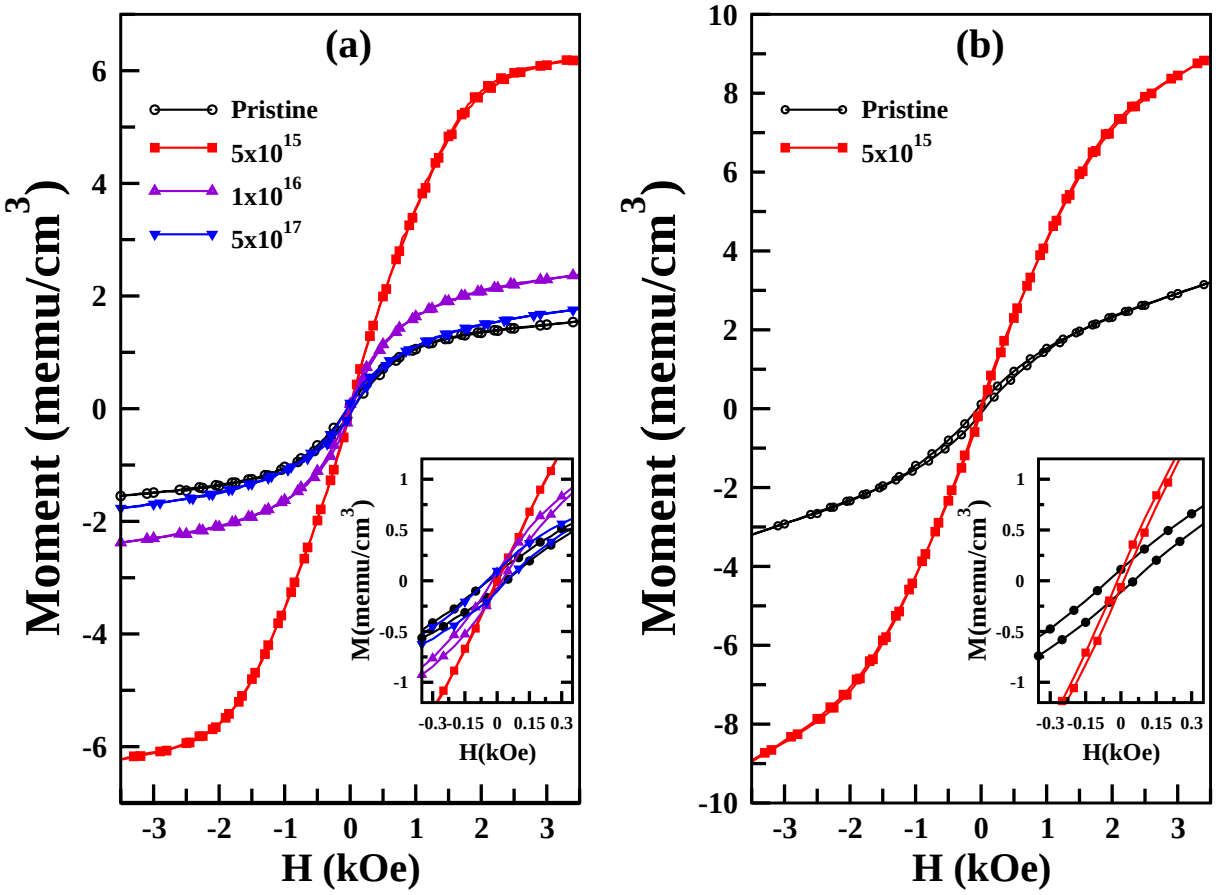

Figure 4.3: Field-dependent magnetization curve measured at (a) RT and (b) 20K from pristine and surfaces nano patterned at various fluences. Insets shows magnified view of hysteresis loops near zero applied field.

compared to pristine surface, has been observed for surfaces patterned with NS of size $\sim 5\ nm$ (see fig. 4.2). This widening can be explained by quantum confinement effect which according to thermodynamic calculations can be pronounced for TiO_2 nanostructures of sizes smaller than ~27 nm [17]. Surfaces irradiated at larger fluences, 1×10^{16} and $5 \times 10^{17}\ ions/cm^2$, also demonstrate some widening in E1 (55 and 45meV, respectively). It is, however, much smaller due to the fabrication of bigger nanostructures (10 and 25nm, respectively) at these fluences.

As measured Field-dependent magnetization (M-H) results, at RT and 20K, are presented in fig. 4.3 and table 4.1 for pristine and nanostructured surfaces. The pristine surface displays ferromagnetic behavior at 300 K with M_S of $1.52\ memu/cm^3$, M_R of $0.06\ memu/cm^3$ and H_C of $39\ Oe$. Presence of oxygen vacancies, V_o, can affect the magnetic nature of the materials [4, 6, 7]. Presence of small amount of V_o on pristine TiO_2, as shown by Solanki et. al. [14], can be responsible for the observation of mild ferromagnetic behavior here [4]. Interestingly,

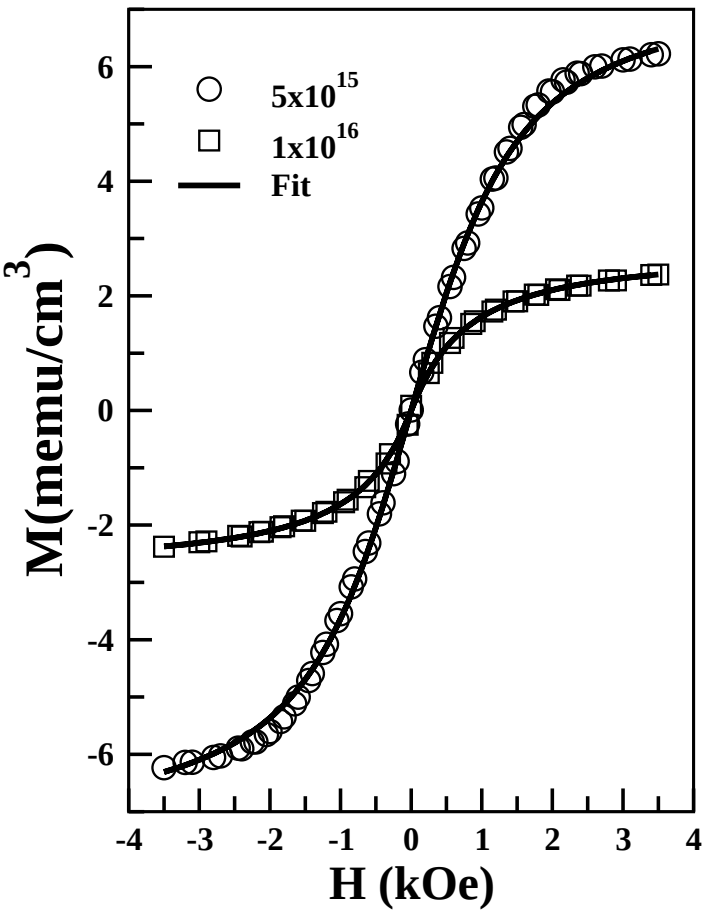

Figure 4.4: M(H) from 5 (5×10^{15}) and 10 nm (1×10^{16}) nanostructures on patterned surfaces. Langevin function fitting, using eq. 4.1, is shown for both (5 and 10 nm) nanostructures.

for surfaces patterned with small ($\sim$5 nm) nanostructures, a large M_S of $6.34\ memu/cm^3$ is observed. In addition, very small values of M_R($0.01\ memu/cm^3$) and H_C ($0.5\ Oe$) indicate presence of superparamagnetic (SPM) character. Such behavior is expected from single domain magnetic quantum dots [9]. Though SPM in Co-doped TiO_2 has been observed earlier [6, 8], there are no studies in literature exhibiting SPM, in TiO_2, in absence of any doping. For larger nanostructures, created at higher fluences, lower M_S but larger M_R and H_C are observed. Similar variations, with NS size, have been observed earlier [6, 10, 18]. Even though the nanostructure sizes (10 and 25 nm), at this stage, are smaller than quantum confinement limit (27 nm) for TiO_2 [17], high H_C suggests ferromagnetic character. Lower thermal fluctuations [7] are responsible for the higher magnetic moments and coercivity observed at 20K.

The magnetization curve for spherical single domain superparamagnetic quantum dots can be described [19] by a weighted sum of Langevin function ($L(x)$) :

Table 4.1: Sizes and magnetic properties of the nanostructures.

fluence (ions/cm^2)	Size (nm)	M_S $(memu/cm^3)$		M_R $(memu/cm^3)$		H_C (Oe)	
		300 K	20 K	300 K	20 K	300 K	20 K
Pristine	–	1.52	2.96	0.06	0.11	39	54
5×10^{15}	5	6.34	8.98	0.01	0.08	0.5	15
1×10^{16}	10	2.37	–	0.08	–	21	–
5×10^{17}	25	1.8	–	0.10	–	46	–

$$M(H) = \int_0^\infty f(y)[\mu L(x)]dy. \tag{4.1}$$

The Langevin function is given by $L(x) = coth(x) - 1/x$ where x = μH/k$_B$T, k$_B$ is the Boltzmann constant, μ (= M$_S$V) is the magnetic moment, V is the volume and M$_S$ is the saturation magnetization of the nanoparticle. For a particle with diameter, D, and median diameter distribution, D_0, the log-normal particle size distribution function has been given by chantrell et al. [20]:

$$f(y) = \frac{1}{\sqrt{2\pi}y\sigma} \exp\left[-\frac{(\ln y)^2}{2\sigma^2}\right] \tag{4.2}$$

where y is the reduced diameter (D/D$_o$), σ is the standard deviation of $\ln y$ and $\langle$D$\rangle$ (= D$_o$ exp($\frac{\sigma^2}{2}$)) is the average particle diameter.

Equation 4.1 has been utilized to fit RT magnetization curve from surfaces patterned with $\sim$5 nm and $\sim$10 nm sized nanostructures and the results are displayed in fig. 4.4. Langevin function fittings suggest formation of single magnetic domain to be $\sim$3.97 nm in diameter, for 5 nm sized nanostructures, whereas the domain size is $\sim$ 8.65 nm, for 10 nm sized nanostructures which may have single or multi-domain character. These nanostructures, fabricated by ion beam technique, thus probably contain $\sim$1nm thick magnetically inert layer on the surface. Existence of such inert layer can be expected on very small nanostructures [7]. The estimated values of magnetic moment, μ, using eq. 4.1, are found to be 0.022 μ_B and 0.085 μ_B for 3.97 and 8.65 nm sized domains, respectively. The stronger exchange coupling between nanodots, due to electronic delocalization by strong oxygen 2p-orbitals overlap, might lead to the lower value of μ for the closely spaced smaller sized nanostructures [21, 22].

4.4 Conclusion :

In this chapter, nanopatterns have been created on TiO_2(110) surfaces through ion beam irradiation. These nanostructured surfaces display a widening of semiconducting band gap along with reduced optical reflectance. Investigation of the magnetic properties indicate superparamagnetic behavior at RT from surfaces decorated with smallest, $\sim$5nm nanostructures. The results from Langevin function fitting indicate that this SPM occurs due to quantum confinement effect related to single magnetic domain of $\sim$3.97nm. SPM behavior, obtained in the absence of any doping here, has never been observed earlier for TiO_2 nanostructures. For larger nanostructures, a ferromagnetic behavior is observed. These results can have potential for spintronics devices.

Bibliography

[1] A. Fujishima, and K. Honda, Nature **238**, 37 (1972).

[2] K. Hashimoto, H. Irie, and A. Fujishima, Jpn. J. Appl. Phys. **44**, 8269 (2005).

[3] Y. Matsumoto, M. Murakami, T. Shono, T. Hasegawa, T. Fukumura, M. Kawasaki, P. Ahmet, T. Chikyow, S. Y. Koshihara, and H. Koinuma, Science **291**, 854 (2001).

[4] K. Bapna, R. J. Choudhary, S. K. Pandey, D. M. Phase, S. K. Sharma, and M. Knobel, Appl. Phys. Lett. **99**, 112502 (2011).

[5] N. H. Hong, W. Prellier, J. Sakai, and A. Hassini, Appl. Phys. Lett. **84**, 2850 (2004).

[6] S. R. Shinde, S. B. Ogale, J. S. Higgins, H. Zheng, A. J. Millis, V. N. Kulkarni, R. Ramesh, R. L. Greene, and T. Venkatesan, Phys. Rev. Lett. **92**, 166601 (2004).

[7] D. Caruntu, G. Caruntu, and C. J. OConnor, J. Phys. D: Appl. Phys. **40**, 5801 (2007).

[8] D. H. Kim, J. S. Yang, Y. S. Kim, D. W. Kim, T. W. Noh, S. D. Bu, Y. W. Kim, Y. D. Park, S. J. Pearton, Y. Jo, and J. G. Park, Appl. Phys. Lett. **83**, 4574 (2003).

[9] W. Zheng, P. Kumar, A. Washington, Z. Wang, N. S. Dalal, G. F. Strouse, and K. Singh, J. Am. Chem. Soc. **134**, 2172 (2012).

[10] O. Kubo, T. Ido, H. Yokoyama, and Y. Koike, J. Appl. Phys. **57**, 4280 (1985).

[11] X. Chen, and S. S. Mao, Chem. Rev. **107**, 2891 (2007).

[12] S. Majumder, D. Paramanik, V. Solanki, B. P. Bag, and S. Varma, Appl. Phys. Lett. **98**, 053105 (2011).

[13] F. Frost, A. Schindler, and F. Bigl, Phys. Rev. Lett. **85**, 4116 (2000).

[14] V. Solanki, S. Majumder, I. Mishra, P. Dash, C. Singh, D. Kanjilal, and S. Varma, J. Appl. Phys. **115**, 124306 (2014).

[15] J. Pascual, J. Camassel, and H. Mathieu, Phys. Rev. B, **18**, 5606 (1978).

[16] J. H. Im, J. Chung, S. J. Kim, and N. G. Park, Nanoscale Res. Lett. **7**, 353 (2012).

[17] N. Satoh, T. Nakashima, K. Kamikura, and K. Yamamoto, Nat. Nano. **3**, 106 (2008).

[18] X. Xu, C. Xu, J. Dai, J. Hu, F. Li, and S. Zhang, J. Phys. Chem. C, **116**, 8813 (2012).

[19] S. K. Suh, K. Yuet, D. K. Hwang, K. W. Bong, P. S. Doyle, and T. A. Hatton, J. Am. Chem. Soc. **134**, 7337 (2012).

[20] R. W. Chantrell, J. Popplewell, and S. Charles, IEEE Trans. Mag. **14**, 975 (1978).

[21] J. L. Moran-Lopez, Rev. Mexi. de Fisica S, **53**, 37 (2007).

[22] X. Wei, R. Skomski, B. Balamurugan, Z. G. Sun, S. Ducharme, and D. J. Sellmyer, J. Appl. Phys. **105**, 07C517 (2009).

Chapter 5

Photo-absorbance Properties of Constrained Nanostructures on Rutile TiO_2(110) Surfaces

5.1 Introduction :

Titanium dioxide expresses a variety of intriguing and fascinating properties. In addition to the distinct appeal of this material as a model oxide system for fundamental investigations, its applications as photovoltaic, photocatalyst, gas sensor and bio compatible material are very attractive [1–4]. Photo- induced surface reactivity and splitting of water by photoactivated TiO_2 have spurred several stimulating activities. Interest in TiO_2 as a photo- reactive material gets however limited owing to its wide bandgap (3.2 eV for anatase and 3.0 eV for rutile phase), restricting its applications primarily to UV regime. Enhancing the photo -absorption response, by utilizing UV as well as visible regions of solar spectrum, is an important research areas with exciting technological implications. Nanostructures and surfaces of TiO_2 have been actively investigated in this direction [5, 6] through a variety of routes like doping and dye sensitization [7, 8]. However, substitutional incorporation of dopants usually requires high temperature annealing treatments whereas organic dye can be unstable causing material modification. In this respect, nanostructuring of surfaces, through ion beams, has commanded compelling attention due to the technological simplicity it presents for achieving self organized structures through mostly single step processes [9–11].

Morphology of nanostructures on surfaces manifests intriguing control in several domains having implications in optics, electronics, magnetism etc. [12]. Dissociation and catalytic properties reveal, several orders of, modification on ion beam patterned metals [13] where specif-

ically tuned parameters have capability of producing distinct nano-dimensional organization. On oxide surfaces, like TiO_2, ion beam patterning also produces surface- vacancies which hold promise for becoming photoactive sites [14].

In this chapter we have investigated the evolution of the constrained nanostructures which have been fabricated on TiO_2(110) surfaces by ion beam irradiation method. The nanostructures are anisotropic in size, constrained in $[1\bar{1}0]$ but elongated in [001] crystallographic direction of the crystal. Anisotropic kinetic effects caused by diffusion of vacancy states as well as itinerant Ti on the surface, created during irradiation, predominantly contribute to the preferential growth of nanostructures. Surprisingly, photo- absorption intensity from these constrained nanostructures demonstrates a distinct behavior which exponentially decreases with the length of the nanostructures in [001] direction. These are intriguing results with implications in tailoring nano- systems, through self assembly, with tuned photo-catalytic properties.

5.2 Experimental :

TiO_2(110) single crystals (commercially purchased from MaTecK) have been irradiated with 60 keV Ar^+ ions (flux = 1.8×10^{14} ions/cm^2.sec) from Electron Cyclotron Resonance (ECR) source. Irradiations were done using ion fluences of 6×10^{17} to 1×10^{19} ions/cm^2 at room temperature. The incident angle of the ion beam was always chosen to be 60° with respect to the surface normal while the azimuthal orientation, i.e. the angle between the projection of ion beam and the [001] surface direction, was either 0° or 90°. All the experimental parameters utilized in this chapter are same as those used in chapter 3 and 4. Here, we have utilized higher Ar ion fluence. The morphology and core level electronic structure of surfaces have been investigated using scanning probe (Nanoscope V from Bruker) microscopy (SPM) and X-ray photoelectron spectroscopy (XPS) from VG-Microtech, respectively. XPS studies were performed under UHV condition with Mg Kα radiation. For angle resolved x-ray photoemission spectroscopy (ARXPS), photoelectron emission angle (γ), defined as the angle between photoelectron spectrometer axis and the surface normal, has been varied from 0° to 75°. The system resolution was 0.9 eV. The optical absorption and structural properties were investigated using Shimadzu UV-Vis spectrophotometer and X-ray diffraction (XRD) setup from Bruker (having CuK_α source), respectively.

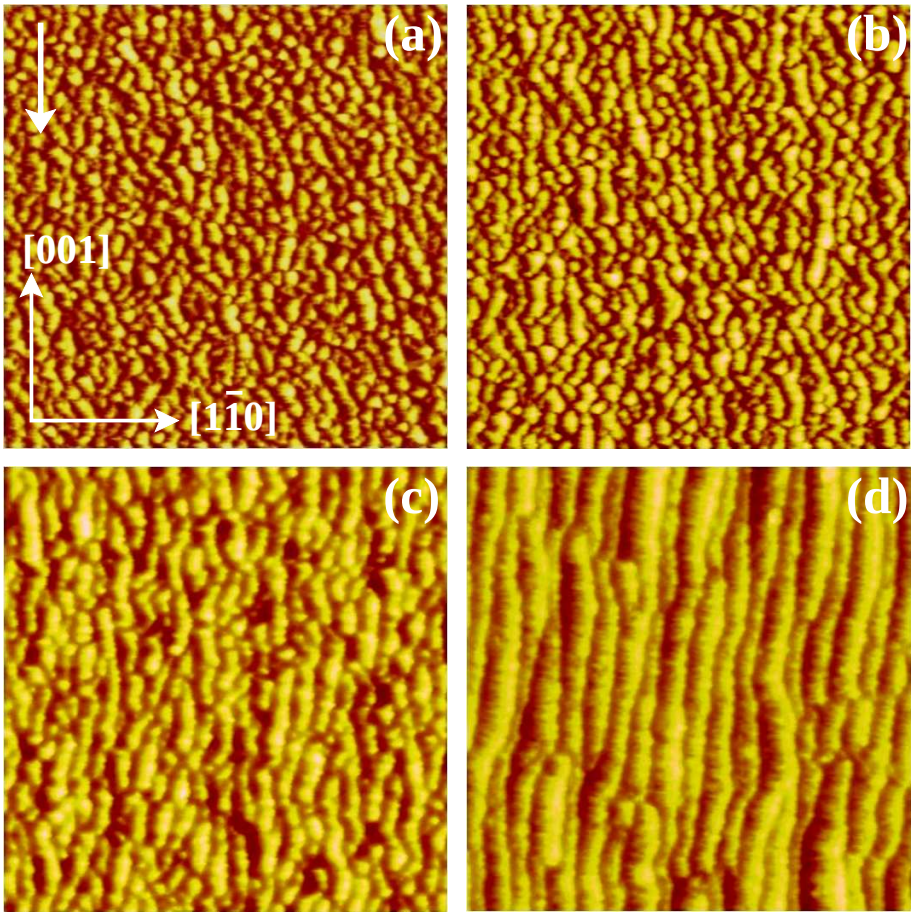

Figure 5.1: SPM images ($5 \times 5\ \mu m^2$) after ion irradiation of TiO_2 at fluences of (a) $6\times\ 10^{17}$, (b) $1\times\ 10^{18}$, (c) $5\times\ 10^{18}$ and (d) $1\times\ 10^{19}$ ions/cm^2. Ion beam projection direction (arrow on top) is along [001] for all images here. Crystallographic axes of the surface are shown.

5.3 Results and Discussions :

Figure 5.1 shows SPM images from TiO_2(110) surface after it was ion irradiated at several fluences. During irradiation, Ar ion beam was incident on the sample at an azimuthal orientation of 0° i.e., parallel to [001] direction. After irradiation at low fluence, formation of nanostructures is observed (fig. 5.1(a)). These nanostructures are slightly elongated in the [001] direction i.e., along the ion beam projection. Evolution of the nanostructures, at increasing ion fluence, enhances this anisotropy further. At fluence of 5×10^{18} ions/cm^2, the nanostructures are quite elongated in [001] displaying aspect ratio as high as 5.7:1 ([001]/1$\bar{1}$0]). For highest fluence of 1×10^{19}ions/cm^2, a well developed ripple pattern, with the crests running along the [001]

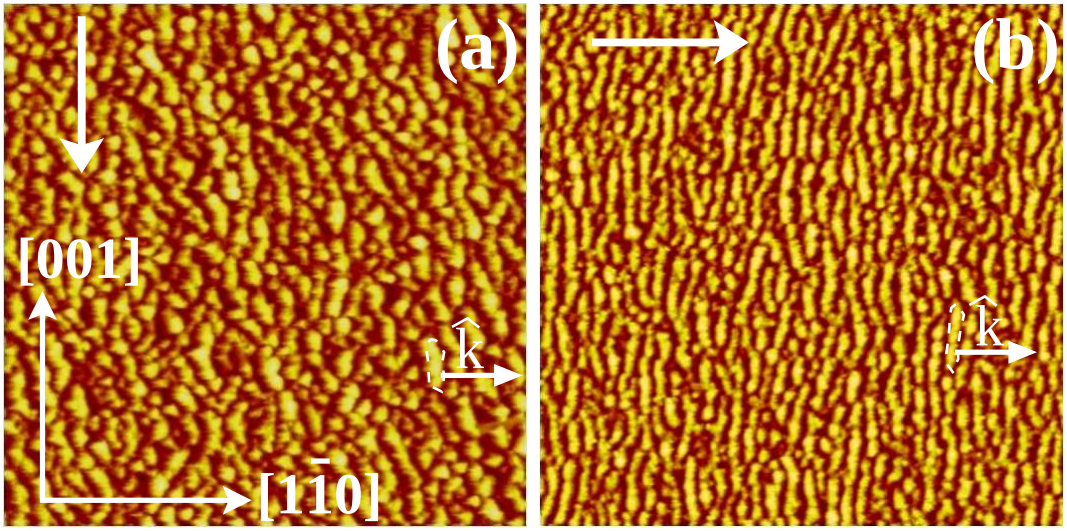

Figure 5.2: SPM images ($5 \times 5\ \mu m^2$) from TiO_2 surfaces irradiated with fluence of 6×10^{17} ions/cm^2. Ion irradiation is along (a) [001] direction and (b) along [1$\bar{1}$0]. Ion beam projection directions are shown on top. In (a) with wave vector, $\hat{k}$, being perpendicular to ion beam direction, the nanostructures are in *perpendicular* mode and in (b) nanostructures are in *parallel* mode.

direction, are observed having a wavelength, or a period, of about 300 nm. A quantitative comparison of nanostructures is presented in table 5.1 which reflects a relatively small increase in size along [1$\bar{1}$0] direction but a significant growth in [001] direction with increasing fluences. For instance, at all the fluences studied here, with ion irradiation along [001] direction, the length along [1$\bar{1}$0] increases by only 3.7 times (from 60 to 220 nm) whereas along [001] it increases by a factor more than 62.5 (from 160 nm to $> 10\mu m$). The nanostructures thus appear constrained along [1$\bar{1}$0] but display significant growth in [001] direction.

In order to assess the role of ion beam direction in the formation of anisotropic nanostructures, the irradiation was also performed with ion beam direction parallel to [1$\bar{1}$0] crystallographic axis for a fluence of 6×10^{17} ions/cm^2 and the results are shown in fig. 5.2(b). Surprisingly not only the nanostructures are still elongated along [001] direction, their anisotropy has further increased with length in [001] becoming longer and size along [1$\bar{1}$0] reducing (table 5.1).

Understanding of spontaneous formation of nanoscale patterns by ion irradiation has been based on the Bradley Harper (BH) model [15] developed under the framework by Sigmund [16] where sputter yield from the trough of a surface modulation is higher than crest. Competing process, encompassing roughening, smoothening [15], solid mass flow [17–19], promoted by

diffusion mechanism regulate the self organization on the surface. With varying ion incidence angles, BH model proposes ripples to be oriented in *parallel* mode (their wave vector, $\hat{k}$, parallel to ion beam direction) below a critical angle and in *perpendicular* mode ($\hat{k}$ perpendicular to ion beam) for grazing incidence geometry. Extensions of BH model further show that under oblique ion incidence (as in present case with incident ions oriented 60° from normal) ripples on Si(111) surfaces can be rotated by 90° with varying fluence; oriented in *parallel* or *perpendicular* mode at low and high fluences, respectively [20]. In variance with both these studies here we visualize, at the same fluence and incidence angle, both perpendicular and parallel modes (in fig. 5.2) by changing ion irradiation direction from being along [001] to $[1\bar{1}0]$. Preferential sputtering of oxide surfaces, like TiO_2, during ion irradiation can induce a variety of vacancy states, as discussed below, which can be active and mobile on the surface. With nanostructures always elongated along [001] direction (in both fig. 5.2(a),(b)) significant diffusive processes of the mobile species seem to be dominating the mechanism of self organization on TiO_2 surfaces. Under this scenario, the size- asymmetricity of the nanostructures will be expected to be controlled by the energetics of the diffusion barriers. Room temperature DFT calculation show, predominantly, transient Ti-O to be the mobile species diffusing with energy barriers of 0.71 and 2.20 eV along [001] and$[1\bar{1}0]$ directions, respectively [21]. The size- anisotropy (2.6) for perpendicular mode nanostructures (see fig. 5.2(a), table 5.1) is surprisingly similar to the anisotropy of these diffusion barriers (3.01) implying compelling role of diffusive currents of mobile species. The anisotropy for the nanostructures in parallel mode configuration (fig. 5.2(b)) is however distinctly higher, suggesting inclusion of erosive mechanisms as well through probably erosion of side edge (with size along $[1\bar{1}0]$ reducing) and inclusion of these eroded species along [001] leading to their elongation (see table 5.1). This is in contrast to grazing incidence ion irradiation of TiO_2 [21], at room temperature, where diffusion primarily is considered to be the dominant mechanism for ripple formation on surfaces. Constrained nanostructures, displaying perpendicular modes in present study, delineate small size- asymmetricity for low fluences (fig. 5.1 (b),(c), table 5.1) which, as discussed above, can be accounted by anisotropic diffusion alone in the high symmetry directions of TiO_2 lattice. Nevertheless, enhanced size- anisotropies at higher fluences (fig. 5.1(d), (e)) require erosive action of ion beams also for self organization on surface. From this analysis, it can be concluded that the presence of asymmetric nature in nanostructure size, as evidenced here, is primarily the result of kinetic effects and not the result of ion beam direction.

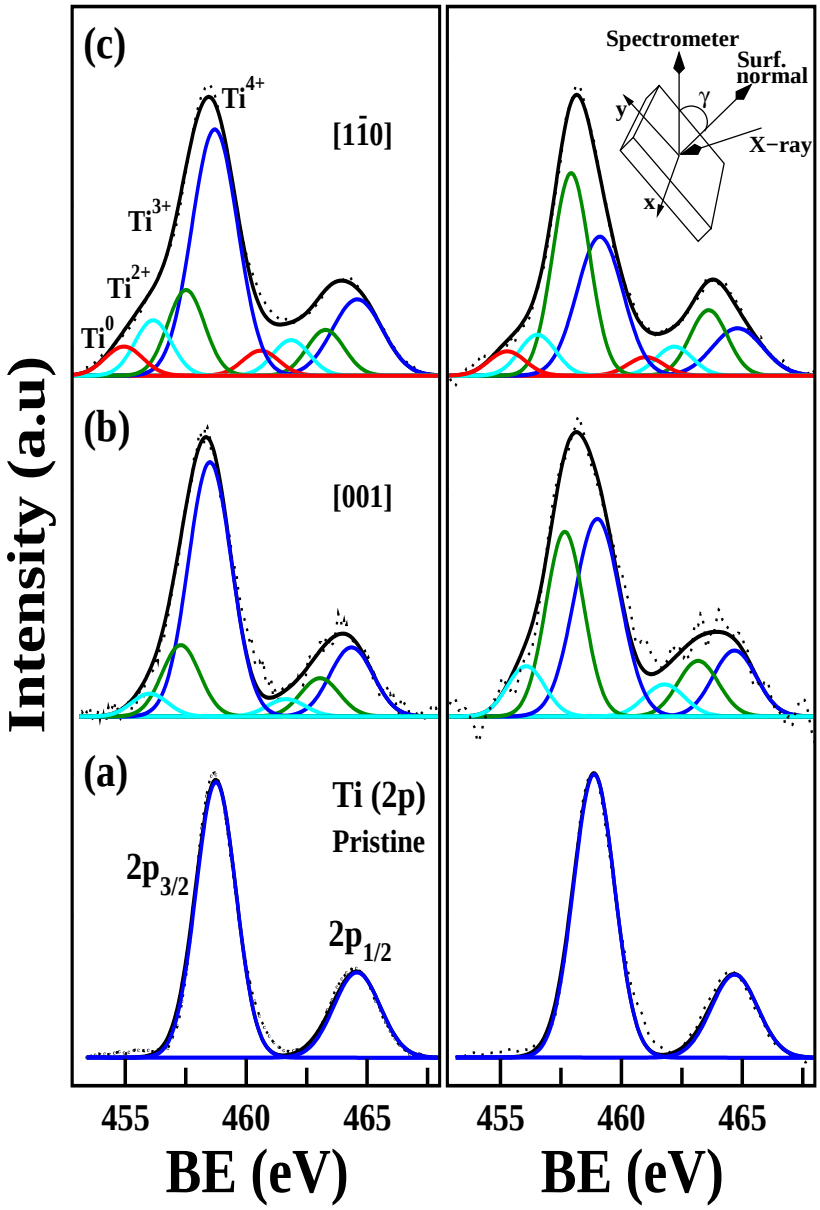

Figure 5.3: Ti-2p core-level XPS spectra from (a) pristine TiO_2 surface and after irradiating TiO_2 for a fluence of $6\times$ 10^{17}ions/cm^2 with ion beam irradiation direction along (b) [001] or (c) [1$\bar{1}$0]. Left and right panels show respectively for γ = 0° and γ = 75° (see inset for γ).

In fig. 5.3 ARXPS spectra are displayed at two photoelectron emission angles (γ), 0° and 75°, with latter supplying accurate surface sensitive information (within top few Å) and former furnishing results from surface to about 1 nm below. This behavior arises from the exponential dependence of signal on depth. The surface sensitivity in ARXPS is a result of shorter attenuation length of electrons from sample. The left panel in fig. 5.3 shows the spectra for γ at 0°. The XPS spectrum from pristine TiO_2(110) sample displays Ti2p features, $2p_{3/2}$ and

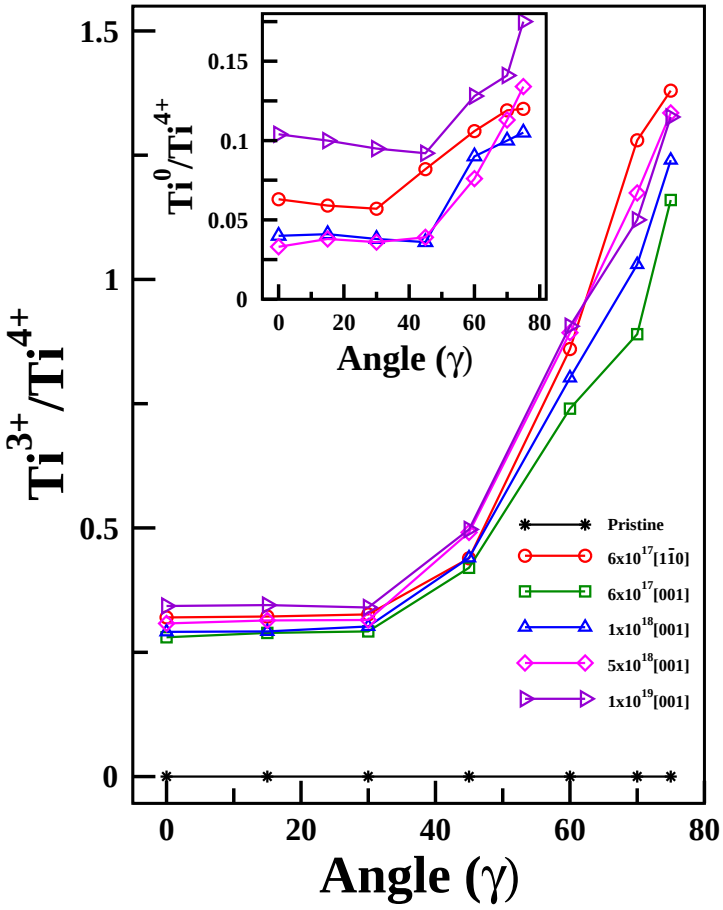

Figure 5.4: Intensity ratio of Ti^{3+}/Ti^{4+} and Ti^{0}/Ti^{4+} (inset) are shown as a function of photo-electron emission angle (γ). Direction of ion irradiation is in square bracket.

$2p_{1/2}$, at binding energies (BE) of 458.8 and 464.6 eV, respectively. These features reflect the Ti^{4+} coordinated sites on rutile surface [4, 11, 22–24]. XPS spectra from samples irradiated at 6×10^{17} ions/cm^2 are also presented (in fig. 5.3) for two cases: when ion irradiation was performed along [001] or along [1$\bar{1}$0]. In addition to Ti^{4+} components (at γ =0°), weak components of Ti^{3+} and Ti^{2+} are also observed (fig. 5.3(b),(c) left panel). Creation of oxygen vacancies with the formation of Ti_2O_3 and TiO, [25, 26] on the surface during irradiation, are responsible for these lower BE features [27]. Furthermore, a small Ti^0 features is also observed but only for samples where ion irradiation was done along [1$\bar{1}$0] crystallographic direction. The surface sensitive XPS spectra (γ =75°) show diminished Ti^{4+} but higher oxygen vacancy states (fig. 5.3(b),(c) right panel) after irradiation.

Explorations of oxygen vacancy states with ARXPS are shown in fig. 5.4. These results have been computed by considering the XPS areas of respective component features (similar

Table 5.1: The results of quantitative analysis of size and anisotropy of nanostructures

fluence (ions/cm^2)	Irradiation along	Size of NS (nm)		Anisotropy [001]/[1$\bar{1}$0]
		along [110]	along [001]	
6×10^{17}	[1$\bar{1}$0]	40±7	280±56	7.0
6×10^{17}	[001]	60±10	160±29	2.6
1×10^{18}	[001]	85±23	230±42	2.7
5×10^{18}	[001]	140±25	800±177	5.7
1×10^{19}	[001]	220±34	$>$ 10000±1200	$>$ 45

to those in fig. 5.3). For pristine sample, no angular variation for Ti^{3+}/Ti^{4+} ratio is observed, as expected. In contrast, after irradiation along [001] with any fluence, there is a drastic enhancement in this ratio at high emission angles, corresponding to increased presence of Ti^{3+} in near- surface regions. Focusing on the this region (i.e. $\gamma \sim 75°$), the ratio nearly increases with fluence up to 5×10^{18} ions/cm^2 and saturates beyond. Furthermore interestingly, comparing the irradiation at the fluence of 6×10^{17} ions/cm^2, performed with ion beam along [001] and [1$\bar{1}$0] directions, the latter shows slightly higher Ti^{3+}/Ti^{4+} ratio (fig. 5.4). Moreover, the Ti^0 component is only present when irradiation is done along [1$\bar{1}$0] direction at this fluence (not along [001] direction as seen fig. 5.3(b),(c)). The angular variation of Ti^0/Ti^{4+} ratio suggests the surface regions (γ =75°) to be having about 10% of Ti^0 species (fig. 5.4 inset). For sample irradiated with highest fluence of 1×10^{19} ions/cm^2, largest Ti^0/Ti^{4+} ratio (17%) can be delineated. These Ti^0 species are also mobile as itinerant atoms on the TiO_2 lattice and are characterized by energy diffusion barriers of 1.14 and 2.79 eV along [001] and [1$\bar{1}$0] directions, respectively [21]. Thus, mobile vacancy states (Ti^{3+}, Ti^{2+}) as well as itinerant Ti (Ti^0), created during ion irradiation of TiO_2, diffuse actively but anisotropically on surface and play crucial role in the generation of size- anisotropic nanostructures.

The photo-absorption response in the visible and UV regimes, from the TiO_2 surfaces with constrained nanostructures, is illustrated in fig. 5.5. Distinct and remarkable increase in absorption intensity, in comparison to pristine, is measured for all samples and has been achieved, in absence of any dopant, by the contribution from nano-dimensional anisotropic nanostructures in association with oxygen vacancy states. Presence of vacancy states control the exciton recombination properties by enhancing the mean free path of the charges [28]. Two band edges at $\tilde{E}1$ and $\tilde{E}2$ (in fig. 5.5) are associated with the TiO_2 bandgap transition [24, 29], from O(2p) valence band to Ti(3d) conduction band, and oxygen vacancy states (Ti^{3+}, Ti^{2+}), respectively [11].

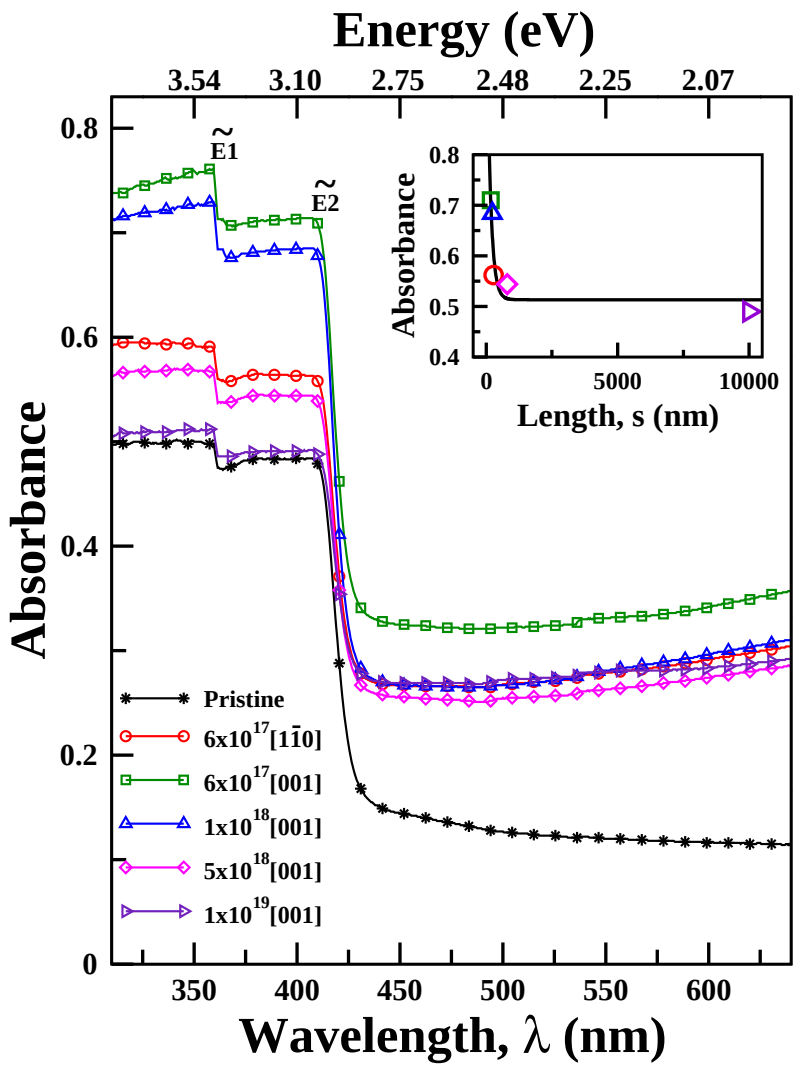

Figure 5.5: UV-Vis photo-absorption spectra for pristine TiO_2 as well as after it is irradiated at various fluences. Direction of ion irradiation is in square bracket. Inset shows behavior of photo-absorption (at λ=400 nm) with nanostructure length (s) along [001]. The line is fit to the data using exponential decay $Ae^{-\eta s} + B$ ($\eta = 0.007\ nm^{-1}$).

Signatures of dimensional dependence of photo- absorbance are astutely indicated by the constrained nanostructures fabricated at same fluence (see fig. 5.2) but under two different ion beam directions viz [001] and [1$\bar{1}$0]. Systematic higher photo- absorbance for the former, with smaller nanostructure-length along [001], suggests distinctive role for this dimension. Further assertion is derived from fig. 5.5(inset) where absorbance (for λ =400nm) at each fluence is presented as a function of nanostructure-length (s) along [001] crystallographic direction, for all samples (see table 5.1). An exponential decay function of form $Ae^{-\eta s} + B$, where A,B and η are fitting parameters, displays good agreement with the measured data.

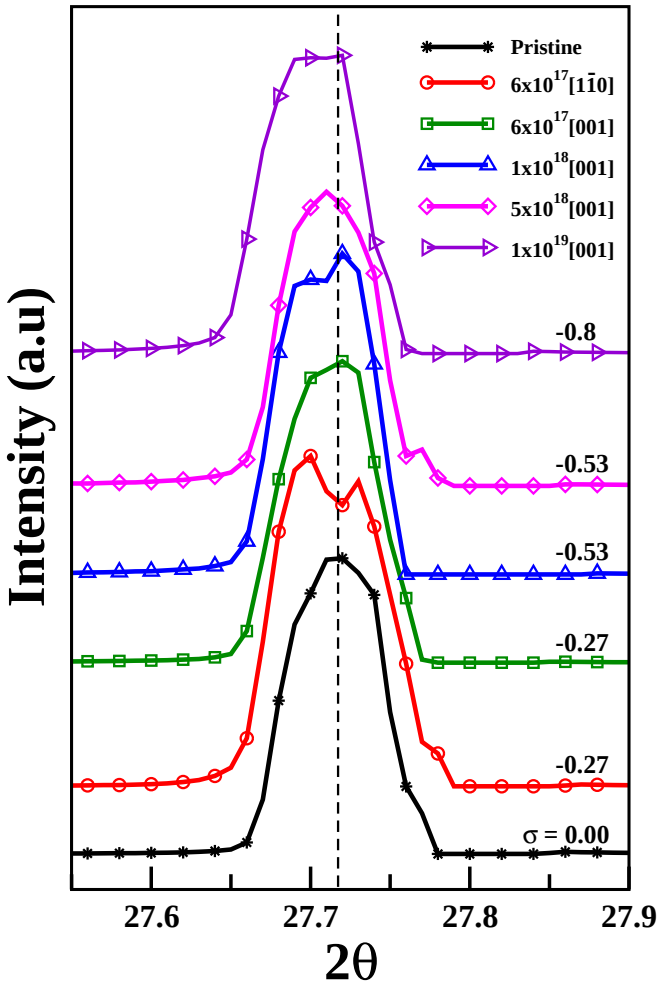

Figure 5.6: (110) XRD feature for pristine TiO_2 as well as after irradiation at various fluences. Direction of ion irradiation is in square bracket. Stress (σ) calculated for each fluence is mentioned.

Influence of surface stress in kinetic instability, which dominates nanostructure formation characteristics, can also drive the self organization. A tensile stress (σ) on the surfaces, that nearly increases with fluence is demonstrated by XRD investigations(fig. 5.6). Presence of vacancy induced states, which are also mobile and diffusing, are characterized with increased inter-planar spacing compared to bulk TiO_2 crystal, leading to the tensile nature of stress exhibited in fig. 5.6.

5.4 Conclusion :

In this chapter, photo-absorption properties of constrained nanostructures with size-anisotropy have been investigated. Anisotropic diffusive current of mobile species like oxygen vacancies

and itinerant Ti, which are produced upon irradiation of TiO_2, crucially regulate the self organization and elongation of the nanostructures. Enhanced photo-absorption response, observed here in the absence of any doping, surprisingly demonstrates an exponentially decaying dependence on the nanostructure- length in fast diffusion direction, along [001]. This behavior leads to fascinating photo-absorption properties of self assembled TiO_2 nanostructures.

Bibliography

[1] A. Fujishima, and K. Honda, Nature **238**, 37 (1972).

[2] K. Hashimoto, H. Irie, and A. Fujishima, Jpn. J. Appl. Phys. **44**, 8269 (2005).

[3] B. O' Regan, and M. Gratzel, Nature **353**, 737 (1991).

[4] S. Majumder, I. Mishra, U. Subudhi, and Shikha Varma, Appl. Phy. Lett. **103**, 063103 (2013).

[5] J. Wang, D. N. Tafen, J. P. Lewis, Z. Hong, A. Manivannan, M. Zhi, M. Li, and N. Wu, J. Am. Chem. Soc. **131**, 12290 (2009).

[6] J. Tao, T. Luttrell, and M. Batzill, Nature Chemistry **3**, 296 (2011).

[7] R. Asahi, T. Morikawa, T. Ohwaki, K. Aoki, and Y. Taga, Science **293**, 269 (2001).

[8] N. G. Park, J. van de Lagemaat, and A. J. Frank, J. Phys. Chem. B **104**, 8989 (2000).

[9] F. Frost, A. Schindler, and F. Bigl, Phys. Rev. Lett. **85**, 4116 (2000).

[10] S. Facsko, T. Dekorsy, C. Koerdt, C. Trappe, H. Kurz, A. Vogt, and H. L. Hartnagel, Science **285**, 1551 (1999).

[11] S. Majumder, D. Paramanik, V. Solanki, B. P. Bag, and Shikha Varma, Appl. Phys. Lett. **98**, 053105 (2011).

[12] S. Majumder, D. Paramanik, A. Gupta, and Shikha Varma, Appl. Surf. Sci. **256**, 513 (2009).

[13] F. Buatier de Mongeot, A. Toma, A. Molle, S. Lizzit, L. Petaccia, and A. Baraldi, Phy. Rev. Lett. **97**, 056103 (2006).

[14] P. M. Kumar, S. Badrinarayanan, and M. Sastry, Thin. Sol. Films **358**, 122 (2000).

[15] R. M. Bradley, and J. M. E. Harper, J. Vac. Sci. Technol. A **6**, 2390 (1988)

[16] P. Sigmund, J. Mat. Sci. **8**, 1545 (1973).

[17] M. Castro, R. Gago, L. Vazquez, J. Munoz-Garcia, and R. Cuerno, Phys. Rev. B. **86**, 214107 (2012).

[18] T. Kumar, A. Kumar, D. C. Agarwal, N. P. Lalla, and D. Kanjilal, Nanoscale Res. Lett. **8**, 336 (2013).

[19] T. Kumar, A. Kumar, N. P. Lalla, S. Hooda, S. Ojha, S. Verma, and D. Kanjilal, Appl. Surf. Sci. **283**, 417 (2013).

[20] Ari-David Brown, Jonah Erlebacher, W. L. Chan, and E. Chason, Phys. Rev. Lett. **95**, 056101 (2005).

[21] M. Kolmer, A. A. Zebari, M. Goryl, F. Buatier de Mongeot, F. Zasada, W. Piskorz, P. Pietrzyk, Z. Sojka, F. Kork, and M. Szymonski, Phys. Rev. B **88**, 195427 (2013).

[22] S. Majumder, D. Paramanik, V. Solanki, I. Mishra, D. K. Avasthi, D. Kanjilal, and S. Varma, Appl. Surf. Sci. **258**, 4122 (2012); V. Solanki, S. Majumder, I. Mishra, S. R. Joshi, D. Kanjilal, and S. Varma, Rad. Eff. Def. Solids. **168**, 518 (2013).

[23] Vanaraj Solanki, Subrata Majumder, Indrani Mishra, P. Dash, C. Singh, D. Kanjilal, and Shikha Varma, Jour. Appl. Phy. **115**, 124306 (2014).

[24] A. K. Rumaiz, J. C. Woicik, E. Cockayne, H. Y. Lin, G. H. Jaffari, and S. I. Shah, Appl. Phys. Lett. **95**, 262111 (2009).

[25] S. D. Yoon, Y. Chen, A. Yang, T. L. Goodrich, X. Zuo, D. A. Arena, K. Ziemer, C. Vittoria, and V. G. Harris, J. Phys. Cond. Mat. **18**, L355 (2006).

[26] H. Y. Jeong, J. Y. Lee, S. Y. Choi, and J. W. Kim, Appl. Phys. Lett. **95**, 162108 (2009).

[27] V. E. Henrich, G. Dresselhaus, and H. J. Zeiger, Phys. Rev. Lett. **36**, 1335 (1976).

[28] X. Pan, M. Q. Yang, X. Fu, N. Zhang, and Y. J. Xu, Nanoscale **5**, 3601 (2013).

[29] J. Pascual, J. Camassel, and H. Mathieu, Phys. Rev. B. **18**, 5606 (1978).

Chapter 6

Enhanced Photo- absorption from ZnO(0001) Nanostructures fabricated by Atom Beam Sputtering

6.1 Introduction :

Zinc Oxide (ZnO) is an attractive material presenting many impressive physical properties. Nano dimensional ZnO, with modified electronic and optical properties, have also received considerable attention due to their wide range of applications as transparent conductive oxide (TCO), opto- electronic and piezo- electric device, gas and chemical sensor [1–3]. As a wide bandgap (3.37 eV) semiconductor with large exciton binding energy of 60 meV at room temperature, ZnO is an appealing candidate for photovoltaic applications. Interest in this system also stems from its high electron mobility, efficient charge transport and collection, good power conversion efficiency etc. [2]. With these characteristic properties, it is utilized in variety of photovoltaic applications, dye sensitized solar cell, hybrid solar cells, etc. [1, 2, 4]. Enhancing photo-absorption properties is, thus, an important necessity for improved performances in these fields [2]. With these objectives, a wide range of ZnO morphologies and dopants have been explored [1]. Modulating its bandgap with dopants or sensitizing with dye are active area of research where stability of incorporated material is of significant importance [1, 4, 5]. However, for substitutional incorporation of dopants in ZnO, usually a high temperature annealing treatment is required [5] and organic dye can be often unstable leading to material modification [4]. Thus, bandgap tailoring in dopant free conditions is an important domain of research that deserves attention.

Atom beam irradiation presents a simple methodology for fabrication of rich variety of

nano-dimensional patterns, in large area, through a single step process. Spontaneous pattern formation by ion irradiation is based on a Bradley Harper (BH) model [6] wherein curvature dependent erosion and surface smoothening regulate the nanoscale morphology on the surface. Systematic fabrication of such self assembled ensembles, with tuned properties, show many interesting behaviors and morphologies [7–11]. Furthermore for binary compounds, preferential sputtering of atoms, can generate vacancy states regulating and modifying many properties [8, 10].

The present study investigates the nanoscale patterns created on the ZnO(0001) surfaces during atom beam irradiation. The nanostructured surfaces display enhanced photo- absorption response compared to the pristine. Surprisingly, the bigger nanostructures demonstrate higher response. Development of photo- active, new phases as well as creation of oxygen vacancies and Zn interstitials, during atom beam irradiation, are responsible for these significant results which have been achieved here in absence of any dopant element and can have exceptional consequences for ZnO photovoltaics.

6.2 Experimental :

ZnO(0001) single crystals have been irradiated using 1.5 keV neutral Ar atom beam at room temperature under a vacuum of 7×10^{-7} Torr. Irradiations have been performed at two different incident angles, 15° and 32°, with respect to surface normal. Fluence of 1.2×10^{17} ions cm^{-2} and a flux $\sim 2 \times 10^{14}$ ions cm$^{-2} \cdot s^{-1}$ was used for irradiations. Scanning Probe Microscope (SPM) from Bruker (Nanoscope V) and XRD system, also from Bruker, (Cu Kα source, λ=0.15418 nm) were utilized to study the morphological and structural modifications, respectively. Optical absorption spectroscopy investigations were done using Shimadzu (UV-Vis) spectrometer. Angle resolved X-ray photoemission spectroscopy (ARXPS) was performed under UHV condition with Mg Kα radiation. The system resolution is 0.9 eV. Pass energy of 20 eV was used during XPS measurements. Photo- electron emission angle (γ), between photoelectron spectrometer axis and surface normal, was chosen to be 30°

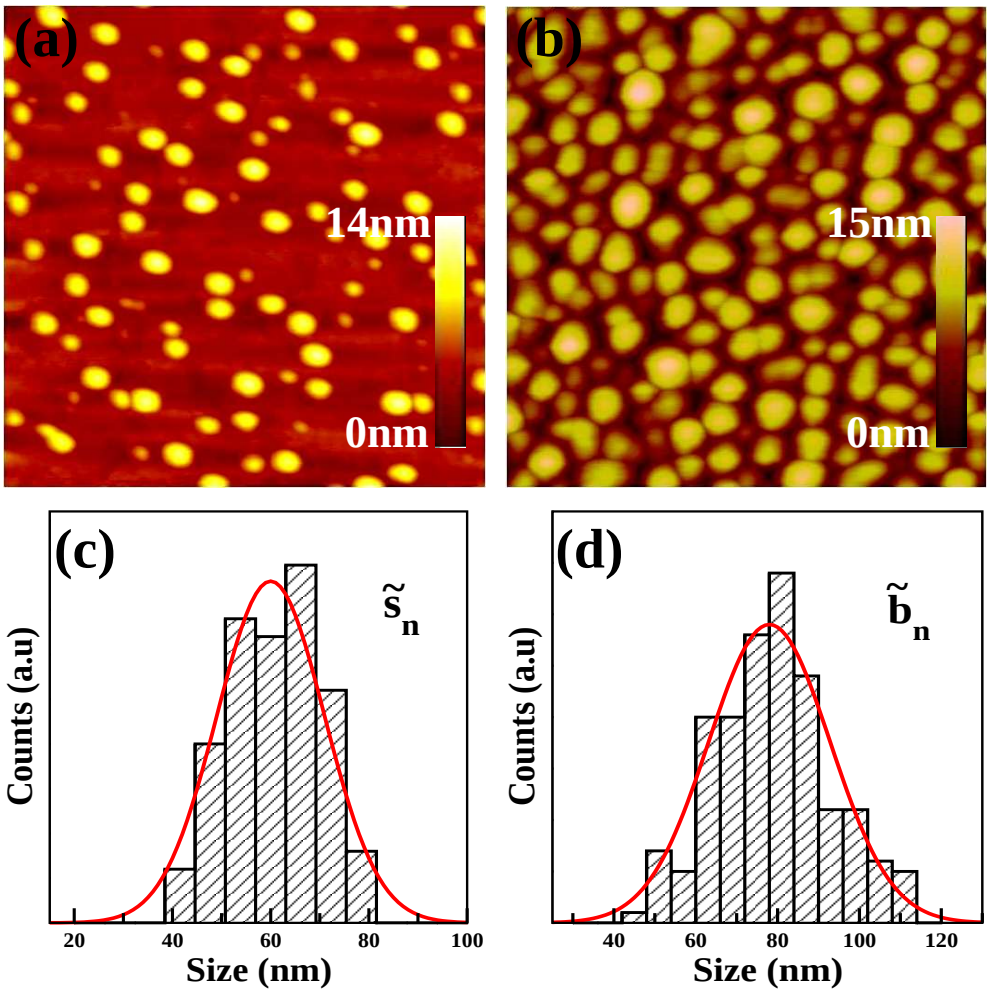

Figure 6.1: SPM images ($1 \times 1\ \mu m^2$) after atom beam sputtering of ZnO(0001) surfaces. Nanostructure (a) $\tilde{s}_n$ and (b) $\tilde{b}_n$ have been respectively created at incident angle of 32° and 15° from surface normal. Respective size distributions of nanostructures are shown for (c) $\tilde{s_n}$ and (d) $\tilde{b_n}$.

6.3 Results and Discussions :

The morphology of atom beam sputtered ZnO(0001) surfaces after irradiation, for both the incident angles, is shown in figure 6.1. Both the surfaces appear to be decorated by nanostructures. However, the surfaces irradiated at higher incident angle (32°) display smaller sized nanostructures, $\tilde{s}_n$, in fig. 6.1 (a) with a density of 8.5 x 10^6 cm^{-2}. An array of denser (2 x 10^{10} cm^{-2}) and bigger nanostructures, $\tilde{b}_n$, is observed in fig. 6.1 (b) on the surfaces irradiated at smaller (15°) irradiation angle. The size distributions presented in fig. 6.1 show average dimensions for $\tilde{s}_n$ and $\tilde{b}_n$ to be 60 and 78 nm, respectively. The rms roughness of the surfaces also increase after atom beam irradiation and is respectively observed to be 1.7 and 2.9 nm (for pristine being

0.5 nm). The surface morphology, upon atom beam sputtering, is controlled through competition between the erosive and diffusive processes [6]. This leads to the spontaneous formation of nano- dimensional patterns on the surface, as observed in fig. 6.1.

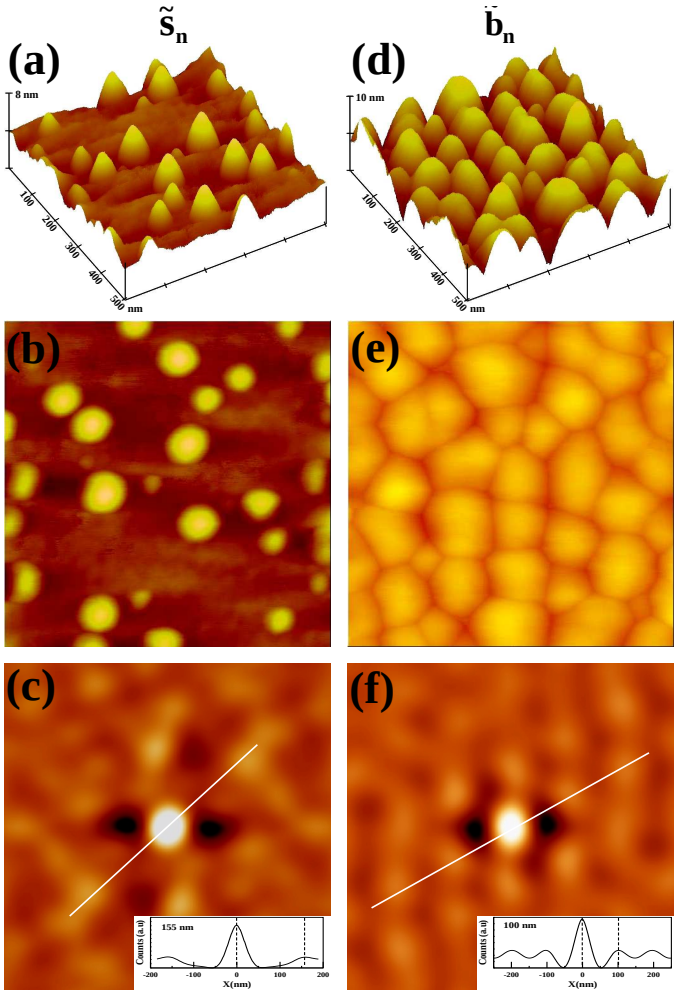

Figure 6.2: Left panel shows SPM images ($500 \times 500\ nm^2$) for (a) 3- dim for $\tilde{s_n}$ (b) 2- dim for $\tilde{s_n}$ and (c) Fast Fourier Transform (FFT) for $\tilde{s_n}$. Right panel shows respective images for $\tilde{b_n}$.

High resolution two and three dimensional AFM images for $\tilde{s}_n$ and $\tilde{b}_n$ are shown in fig 6.2. Although, for the former few randomly distributed nanostructures are observed on the surface in fig. 6.2 (a, b), for the latter a dense close packed hexagonal distribution of nanostructures is observed (fig. 6.2 (d, e)). The Fast Fourier Transformation (FFT) images of these distributions, presented here for both nanostructures, also confirm this. Although no periodicity is observed in the distribution of $\tilde{s}_n$ (fig. 6.2 (c)), $\tilde{b}_n$ nanostructures demonstrate a long ranged periodic behaviour of nearly 100 nm wavelength (fig. 6.2 (f)).

Height-height correlation (HHC) studies are also efficient in providing insight in surface

evolution as well as details for periodicity on the surface. This analysis can provide the scaling parameters which are important for understanding the surface morphology and its growth. The HHC function for surface height, h(**r**), at position, **r**, is described as [12]:

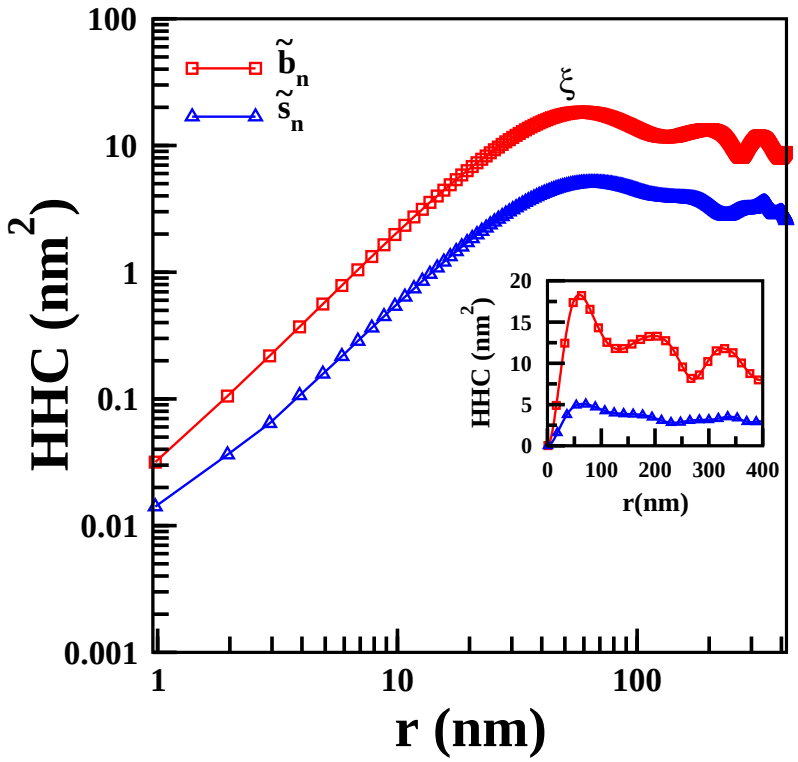

Figure 6.3: HHC for pristine ZnO and for nanostructured surfaces with $\tilde{s_n}$ and $\tilde{b_n}$. Inset shows HHC with *r* in linear scale.

$$G(\mathbf{r}) = N^{-1} \sum_{\mathbf{r}'} \langle [h(\mathbf{r}+\mathbf{r}') - h(\mathbf{r}')]^2 \rangle \tag{6.1}$$

Here $\mathbf{r}'$ is a constant and N is the total number of positions considered. According to the theory of kinetic roughening, the dynamic scaling hypothesis suggests HHC function to show the behavior of following type:

$$G(\mathbf{r}) = \begin{cases} \sim \mathbf{r}^{2\alpha}, & \text{for } \mathbf{r} << \xi. \\ 2w^2, & \text{for } \mathbf{r} >> \xi \end{cases} \tag{6.2}$$

where, α is the roughness exponent, ξ is the lateral correlation length and *w* is related to rms surface roughness. Both α and ξ are important scaling parameters providing insight in the surface evolution. The former relates to random fluctuations on the surface, at very short length scales, whereas the latter provides the length up to which the surface- height remains correlated.

Figure 6.3 presents HHC function for both the nanostructured surfaces. The rms surface roughness, w, for surfaces with $\tilde{s}_n$ and $\tilde{b}_n$ is respectively 1.5 and 2.5 nm (w for pristine is 0.6 nm) whereas ξ is 52 and 70 nm. Values of ξ reflect their approximate average sizes of

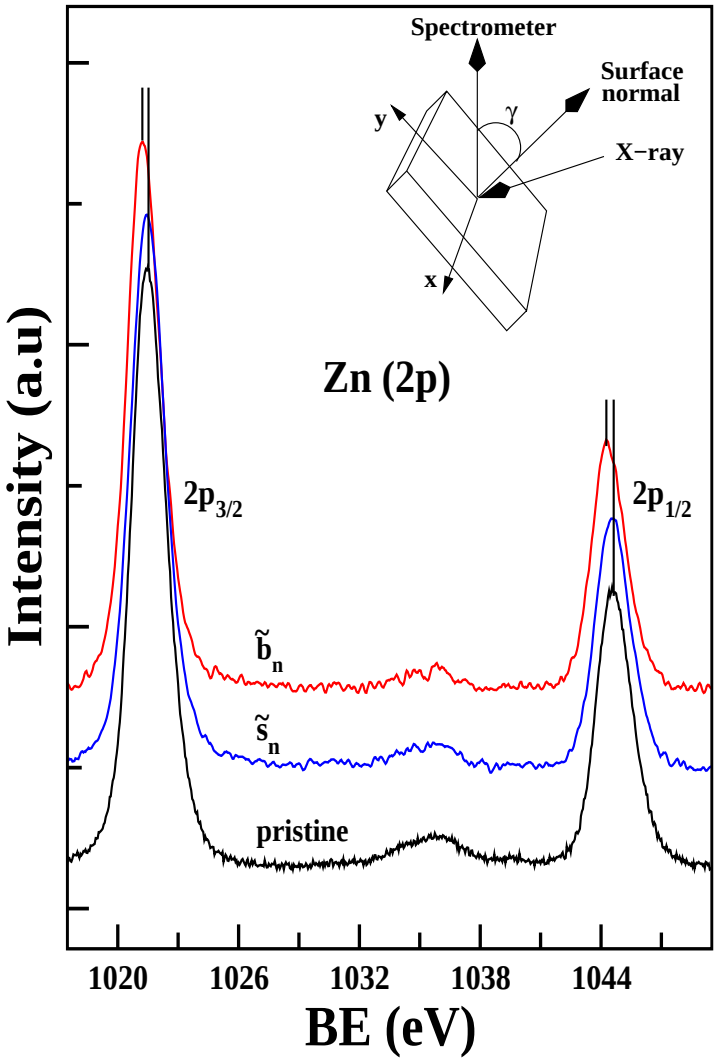

Figure 6.4: Zn-2p core-level XPS spectra (at γ = 30^0) for pristine ZnO and for nanostructured surfaces with $\tilde{s_n}$ and $\tilde{b_n}$. Inset shows geometry for ARXPS and photoelectron emission angle, γ.

nanostructure (see fig. 6.1). For both the nanostructured surfaces, α is measured to be 0.82. Same value of α will suggest that similar dynamics of surface evolution exists for both the cases of nanostructure formation. With α of 0.82, theory of kinetic roughening would indicate the surface evolution to be primarily through similar, nearly random growth processes. However, for $r \geq \xi$, periodic modulations (with periodicity of $\sim$100 nm) are observed only for surfaces with $\tilde{b}_n$ and not in the case of $\tilde{s}_n$ indicating that the surfaces decorated with $\tilde{b}_n$ develop a long

range periodicity (as seen in inset of fig. 6.3 with clear modulations in the linear scale) not demonstrated by smaller $\tilde{s}_n$ nanostructures. So interestingly, though the morphology of two nanostructured surfaces is similar at small r (as their α are similar), it is remarkably different at large separations and show different long range behavior.

In fig. 6.4, ARXPS spectra are displayed for photoelectron emission angle (γ) of 30° providing information from surface to about 1 nm below. This surface sensitivity is a result of shorter attenuation length of electrons from the sample. The spectrum from pristine ZnO(0001) displays Zn2p features, $2p_{3/2}$ and $2p_{1/2}$, at binding energies (BE) of 1021.5 and 1044.6 eV, respectively. These features reflect the Zn^{2+} coordinated sites on the surface [13]. XPS spectra from the the nanostructured surfaces with $\tilde{s}_n$ and $\tilde{b}_n$ are also presented here. The XPS spectrum from the surface with $\tilde{b}_n$, interestingly displays a shift, of both $2p_{3/2}$ and $2p_{1/2}$ features, by about 0.3 eV towards lower BE. This suggests presence of oxidation state less than +2 for Zn [14]. Preferential sputtering of oxygen atoms, during atom beam irradiation, can contribute to the creation of oxygen vacancy state, with the two electrons associated with Oxygen atom getting transferred to the empty 2p orbitals of the neighboring Zn atom and in turn creating Zn sites with oxidation states less than +2 (as seen in fig. 6.4). This also contributes to the formation of Zn-rich regions which promote the spontaneous nucleation and self assembly of nanodots. Similar nanoscale patterning have been earlier observed for TiO_2 [8] and InP [11, 15, 16] by ion beam sputtering technique. However, in the present investigation neutral atom beams are being utilized for fabrication of nanostructures on ZnO(0001).

Core level XPS spectra from O 1s region are presented in fig. 6.5 for the pristine as well as the nanostructured surfaces. The main component in the pristine at 530.2 eV can be attributed to O^{2-} ions present in stoichiometric wurtzite ZnO lattice [17] (fig. 6.5 (a)). The feature at 531.9 eV is due to the small number of oxygen vacancy states (V_o) present on the surface [17]. The intensity of the vacancy states is much higher on nanostructured surfaces and becomes significantly enhanced for surfaces with bigger, $\tilde{b}_n$, nanostructures (fig. 6.5 (c)). As a result, the ratio (R) of intensity for oxygen vacancy state w.r.t. O^{2-} state (see fig. 6.5) increases from 0.64 for pristine, to $\sim$0.87 and $\sim$7.41 for surfaces with $\tilde{s}_n$ and $\tilde{b}_n$, respectively. Enhancement of this ratio, R, or the oxygen- vacancy (V_o) contribution with irradiation of oxide surfaces is a consequence of preferential sputtering and has been earlier observed for systems like TiO_2 [8]. Preferential sputtering promotes increased sputtering of lighter atoms and hence can lead to the creation Zn sites, with less than +2 oxidation state, on the nanostructured surface as observed

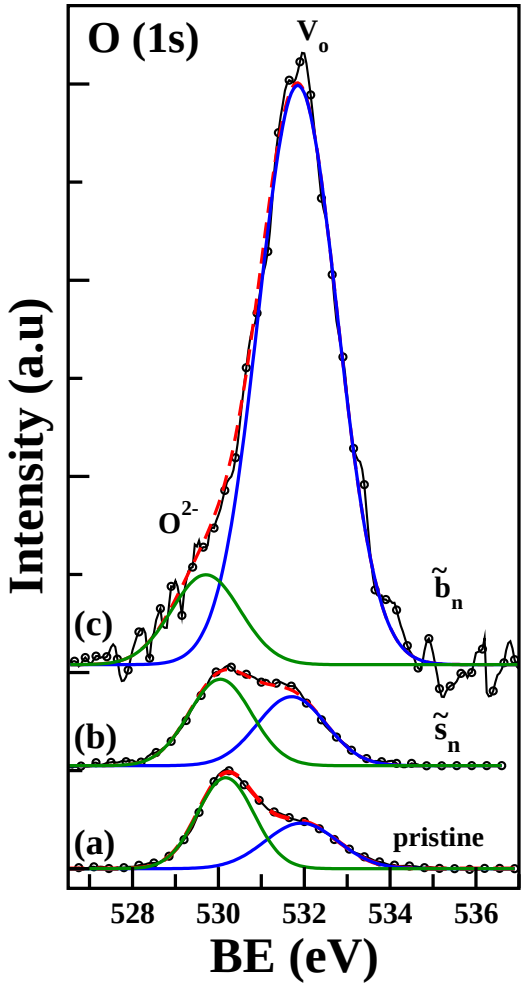

Figure 6.5: O-1s core-level XPS spectra (at γ = 30^0) from pristine ZnO and for nanostructured surfaces with $\tilde{s_n}$ and $\tilde{b_n}$.

by BE shifts for $\tilde{b}_n$ (in fig. 6.4). These BE shifts suggest increased metallic Zn regions on the surface. These metal rich zones contribute to the nucleation of nanostructures.

The X-ray diffraction (XRD) spectra from pristine as well as nanostructured surfaces are displayed in fig. 6.6. A strong (0002) feature accompanied by a very weak (0004) feature can be observed for the pristine surface (fig. 6.6 (a)) as well as for surface with $\tilde{s}_n$ (fig. 6.6 (b)). However, a drastic enhancement in (0004) feature, along with the development of two new weak features, $(11\bar{2}0)$ and $(21\bar{3}0)$ [18], has been noticed for the surface with $\tilde{b}_n$. Surprisingly, this shows a nearly 40 times increase in the (0004) feature. This can be attributed to the distinct growth of $\tilde{b}_n$ nanostructures along this direction [19]. Presence of new phases along $(11\bar{2}0)$ and $(21\bar{3}0)$ also indicates the growth of nanostructures along these directions as well.

Atom beam irradiation has also led to the production of stress in the inter- planar regions

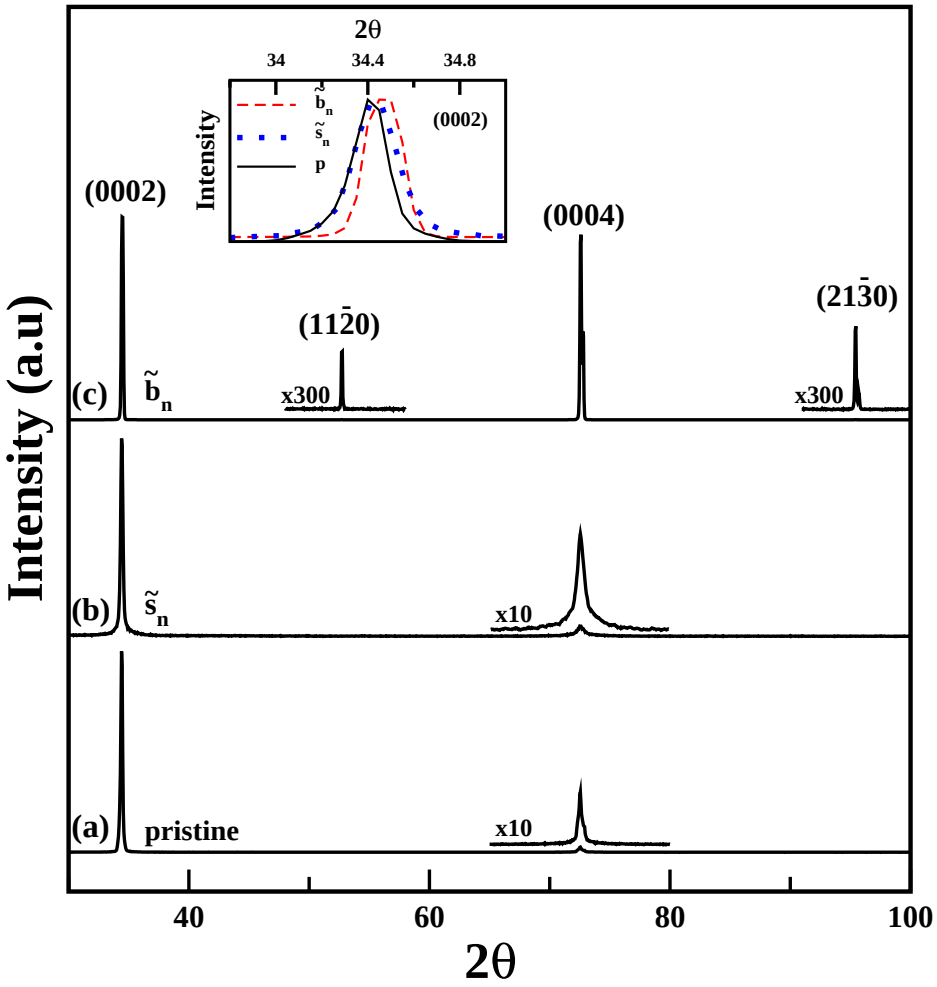

Figure 6.6: XRD spectra for pristine ZnO and for nanostructured surfaces with $\tilde{s_n}$ and $\tilde{b_n}$. Inset shows shifts in (0002) feature for $\tilde{s_n}$ and $\tilde{b_n}$ compared to pristine.

of ZnO lattice. This is delineated by the appearance of shifts in the (0002) feature, for both the samples in fig. 6.6(inset). For the samples with $\tilde{s}_n$ and $\tilde{b}_n$, the shifts are respectively 0.02° and 0.06° towards higher angles compared to pristine. The stress generated in the ZnO lattice, as suggested by angular blue shifts, is due to the reduction in the inter- planer spacings. The creation of oxygen vacancy sites as well as production of Zn metal rich regions, as shown by XPS results here, can produce these transformations in the ZnO lattice. The residual stress, σ, in a nanostructured surface can be estimated using [20]

$$\sigma = \left(2C_{13} - C_{33}\frac{C_{11}+C_{12}}{C_{13}}\right)\left(\frac{d_s - d_0}{d_0}\right) \tag{6.3}$$

where C_{ij} are elastic stiffness constants and d_0, d_s are the inter- planar spacings for the pristine

and the nanostructured surfaces. For the ZnO surfaces considered here, the lattice spacing for the pristine (d_0) is 2.6065 nm and it reduces (as calculated using shifts in fig. 6.6 inset) to 2.6050 and 2.6021 nm for surfaces with $\tilde{s}_n$ and $\tilde{b}_n$, respectively. With C_{ij} known for ZnO [21] (C_{11}= C_{33}=2.1 $\times$ 10^{11} N m^{-2}, C_{12}=1.2 $\times$ 10^{11} N m^{-2} and C_{13}=1.05 $\times$ 10^{11} N m^{-2}), the stress, for both the nanostructured surfaces created after the atom beam irradiation, have been calculated and are found to be 0.25 and 0.76 GPa for surfaces with $\tilde{s}_n$ and $\tilde{b}_n$, respectively. The stress is of compressive nature and the surfaces with $\tilde{b}_n$ demonstrate larger residual stress. This is a surprising result as this suggests that surfaces with larger ($\tilde{b}_n$) nanostructures demonstrate higher stress. However, these nanostructures have been fabricated by the process of atom beam irradiation. The results presented here show that the irradiation has led to much decrease in lattice spacing (for $\tilde{b}_n$ in fig. 6.6 inset) which in turn produces the large stress.

The photo- absorption response from the nanostructured surfaces is presented in fig. 6.7. The response from the pristine surface displays two band edges, $\widetilde{E1}$ and $\widetilde{E2}$, which are respectively associated with the direct band- gap and vacancy related band in ZnO [20, 22]. An enhanced photo absorption from both the nanostructured surfaces, compared to pristine, is demonstrated in fig. 6.7. However surprisingly, surfaces decorated with bigger nanostructures display higher photo- absorption characteristics.

Tauc plots, generated using absorbance data, are also shown in fig. 6.7(inset). For the pristine, ZnO- bandgap energy (E1) is observed at 3.35 eV, whereas the oxygen vacancy related defect- state (E2) is at 3.12 eV. The ZnO bandgap observed here is similar to that seen earlier for wurtzite ZnO [22]. The bandgap (E1) for nanostructured surfaces, however, is much reduced and appears at 3.29 and 3.26 eV for surfaces with $\tilde{s}_n$ and $\tilde{b}_n$, respectively (fig. 6.7 inset). Thus, for the ZnO surfaces with bigger, $\tilde{b}_n$, nanostructures a bandgap reduction of 0.09 eV is observed here. With the inclusion of dopant like N, a reduction of 0.13 eV has been earlier observed in wurtzite ZnO [23]. The bandgap narrowing, as observed in the present study, is more significant as this has been achieved in the absence of any dopant element. This bandgap narrowing can be attributed to the creation of Zn interstitials via preferential sputtering during irradiation. First principle studies and partial density of state calculations on TiO_2 have proposed a localized energy level about 0.1 eV below the conduction band minimum (CBM) due to interstitials on metal-rich surfaces [24] which leads to bandgap narrowing in this system [8]. Development of similar state, about 0.06-0.1 eV below CBM, in ZnO due to Zn interstitials has also been suggested [25, 26]. The bandgap narrowing by 0.06 and 0.09 eV, as seen in the present study

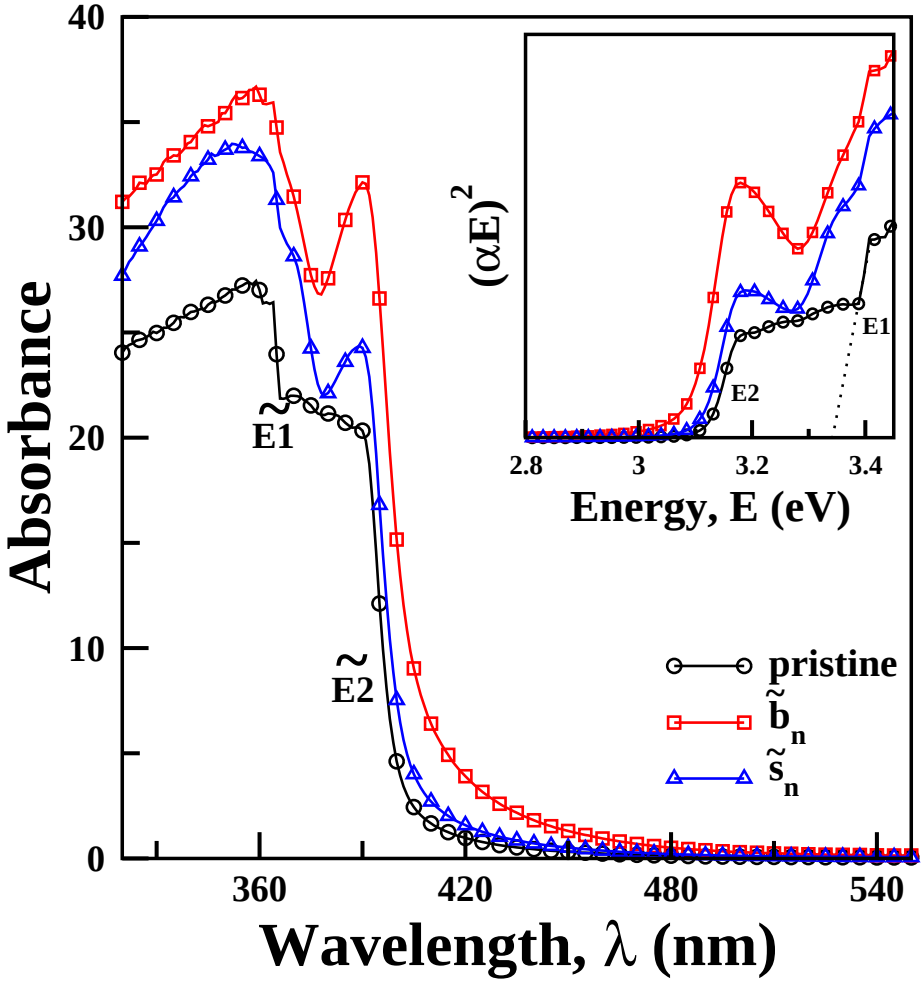

Figure 6.7: Photo- absorbance response for pristine ZnO and for nanostructured surfaces with $\tilde{s_n}$ and $\tilde{b_n}$. Inset shows respective Tauc plots (α is absorption coefficient and E is photon energy).

for ZnO surfaces with $\tilde{s}_n$ and $\tilde{b}_n$, respectively, is thus strongly induced by the Zn interstitials or Zn- rich zones that develop on ZnO surface upon irradiation.

6.4 Conclusion :

In conclusion, the photo- absorption properties of nanostructured surfaces, created by atom beam irradiation of ZnO(0001) have been investigated here. The bigger nanostructures demonstrating hexagonal closed packed ordering, with long ranged periodic behaviour and new crystalline phases, show higher photo- absorption response. The enhanced photo response is primarily related to the bandgap narrowing by 0.09 eV, which occurs due to the creation of Zn

interstitials during irradiation. These results are significant as they have been obtained in the absence of any dopant element.

Bibliography

[1] Z. L. Wang, J. Phys.: Condens. Matter **16**, R829 (2004).

[2] A. B. Djurisic A. M. C. Ng, and X. Y. Chen, Progress in Quantum Electronics **34**, 191 (2010).

[3] Z. L. Wang, and J. Song, Science **312**, 242 (2006).

[4] D. Pugliese, F. Bella, V. Cauda, A. Lamberti, A. Sacco, E. Tresso, and S. Bianco, Appl. Mater. Inter. **5**, 11288 (2013).

[5] R. Dogra , A. P. Byrne, and M. C. Ridgway, Opt. Mat. **31**, 1443 (2009).

[6] R. M. Bradley, and J. M. E. Harper, J. Vac. Sci. Technol. A **6**, 2390 (1988).

[7] S. Facsko, T. Dekorsy, C. Koerdt, C. Trappe, H. Kurz, A. Vogt, and H. L. Hartnagel, Science **285**, 1551 (1999).

[8] S. Majumder, D. Paramanik, V. Solanki, B. P. Bag, and Shikha Varma, Appl. Phys. Lett. **98**, 053105 (2011).

[9] S. Facsko, T. Bobek, A. Stahl, H. Kurz, and T. Dekorsy, Phys. Rev. B **69**, 153412 (2004).

[10] V. Solanki, S. Majumder, I. Mishra, P. Dash, C. Singh, D. Kanjilal, and S. Varma, J. Appl. Phys. **115**, 124306 (2014); ; V. Solanki, S. Majumder, I. Mishra, S. R. Joshi, D. Kanjilal, and S. Varma, Rad. Eff. Def. Solids. **168**, 518 (2013).

[11] D. Paramanik, S. R. Sahoo, S. Majumder, and S. Varma, Vacuum, **84**, 602 (2010).

[12] S. R. Joshi, T. Bagarti, and S. Varma, Surf. Sci. in press (2015).

[13] J. H. Zheng, Q. Jiang, and J. S. Lian, Appl. Surf. Sci. **257**, 5083 (2011).

[14] R. Gurwitz, R. Cohen, and I. Shalish, J. Appl. Phy. **115**, 033701 (2014).

[15] F. Frost, A. Schindler, and F. Bigl, Phys. Rev. Lett. **85**, 4116 (2000).

[16] D. Paramanik, S.N. Sahu, and Shikha Varma, Jour. Phys. D: Appl. Phys. **41**, 125308 (2008).

[17] H. Liu, F. Zeng, Y. Lin, G. Wang, and F. Pan, Appl. Phys. Lett. **102**, 181908 (2013).

[18] S. Mahmud, M. J. Abdullah, J. Chong, A. K. Mohamad, and M. Z. Zakari, J. Cry. Grow. **287**, 118 (2006).

[19] N. N. Jandow, F. K. Yam, S. M. Thahab, H. A. Hassan, and K. Ibrahim, Cur. Appl. Phys. **10**, 1452 (2010).

[20] B. C. Mohanty, Y. H. Jo, D. H. Yeon, I. J. Choi, and Y. S. Cho, Appl. Phys. Lett. **95**, 062103 (2009).

[21] H. H. C. Lai, T. Basheer, V. L. Kuznetsov, R. G. Egdell, R. M. J. Jacobs, M. Pepper, and P. P. Edwards, J. Appl. Phys. **112**, 083708 (2012).

[22] J. Oliva, L. P. Mayen, E. D. la Rosa, L. A. Diaz-Torres, A. T. Castro, and P. Salas, J. Phys. D: Appl. Phys. **47**, 015104 (2014).

[23] S. Shet, K. S. Ahn, T. Deutsch, H. Wang, R. Nuggehalli, Y. Yan, J. Turner, and M. Al-Jassim, J. Mater. Res. **25**, 69 (2010).

[24] E. Cho, S. Han, H. S. Ahn, K. R. Lee, S. K. Kim, and C. S. Hwang, Phys. Rev. B, **73**, 193202 (2006).

[25] K. Bandopadhyay, and J. Mitra, RSC Adv. **5**, 23540 (2015)

[26] F. Oba, A. Togo, and I. Tanaka, Phys. Rev. B. **77**, 245202 (2008).

Chapter 7

Nanoscale Resistive Switching behaviour and Photo-absorption response from NiO nanoflakes

7.1 Introduction :

Nickle oxide (NiO) is a wide bandgap p-type semiconductor and exhibits variety of promising properties like high power density, chemical stability, low toxicity, magnetism etc. It is used in applications as sensors, electrodes for batteries, electrochromic films, magnetic memory devices, photovoltaic cells as well as for renewable and clean energy sources [1–6]. NiO nanostructures have received important attention in semiconductor industry for their optoelectronic properties. These properties crucially depend on the electronic structure and density of nanostructures as well as on surface characteristics at nanoscale [3, 4, 6]. In addition, defects also play an important role as they control the photo-charge generation in devices [7] and their migration can effect the electrical and electronic characteristics in a device.

A new concept of high density and non-volatile memory device has emerged in recent years due to the fundamental limit of conventional flash memories. Numerous efforts have been undertaken to identify the low energy, high speed and scalable technologies for next generation memory devices [1–3, 8]. In addition, resistance-based non-volatile memory devices like magneto-resistive random access memory (MRAM), phase-change random access memory (PRAM) and resistive random access memory (ReRAM) have been proposed and are being investigated for replacing the conventional memories. Due to simple structure for three-dimensional stacking, good scalability and high operation speed, ReRAM devices have attracted immense attention in resistive-switching (RS) based memory applications [3]. The

ReRAM devices rely on the formation and disruption of the conducting filaments (CF) in insulating metal-oxide layers, under the action of applied electric field [1, 3]. This CF enables the switching of ReRAM devices to low and high resistance states. The formation and disruption of CF can be of thermo-chemical type (Joule heating-assisted formation and rupture of localized CF), electro-chemical type (cation migration-based formation and dissolution of metal filaments) or valence change type (field-induced ion migration-based change of Schottky/tunnel barrier at the interface) [9]. Many efforts have been undertaken to understand the nature and structure of CF by methods like impedance spectroscopy [10], transmission electron microscopy (TEM) [8], scanning transmission X-ray microscopy etc.. The CFs are of nanoscale dimensions and their distributions are inhomogeneous in nature. For understanding the nature of charge transport in nanoscale RS devices it is crucial to understand the composition of the metal oxide layers during the development of the filaments. The resistive switching phenomena, through conducting filament formation and disruption, has been reported for various oxide semiconductors like TiO_2, ZrO_2, $SrTiO_3$ (STO), HfO etc. [3]. RS behavior for NiO layers in AZO/NiO and other hybrid structures has also been investigated for understanding issues of oxygen migration and CF formation in heterojunctions and devices [1–3, 8, 11].

This chapter investigates the resistive switching behavior and photo-absorption characteristics of NiO nanoflakes. The nanoflakes, grown by hydrothermal technique, show variation in metallic Ni and Ni^{2+} state with reaction time. Conducting Atomic Force Microscopy (CAFM) has been utilized for investigating the RS behavior in the nanoflakes and the results demonstrate their *bi-stable reversible resistive switching* characteristics and Unipolar nature. Systematic investigations of I-V behavior show that formation and rupturing of the filaments, in NiO nanoflakes, occurs at voltages that depend on the metallic Ni concentration. Photo absorption response, interestingly, demonstrates a nearly similar behavior in UV and visible regions, for nanoflakes grown at low reaction time, but an enhanced UV response for the flake obtained at large times. These nanoflakes displaying multifunctional properties of photo- absorption and RS behavior, that can be modulated with reaction time, are attractive for optoelectronic, electrochromic and RS based memory applications.

7.2 Experimental :

NiO nanostructures have been grown on Au films through hydrothermal method. Gold films act as bottom electrode and were deposited on Si(100) substrates by e-beam evaporation technique, at a base pressure of 2×10^{-7} mbar, using Knudsen cell with 99.995 $\%$ purity gold. The deposition rate and sample rotation speed were maintained at 0.1 $\mathring{A}$ s^{-1} and 20 rpm, respectively.

All chemicals utilized for hydrothermal process were of analytical grade and have been used without any further purification. In a typical procedure, aqueous solution was prepared by mixing 0.05 M nickel nitrate hexahydrate ($Ni(NO_3)_2{\cdot}6H_2O$) and 0.05 M hexamine (HMT, $C_6H_{12}N_4$) solutions. Gold deposited Si substrates were introduced into a glass beaker (reactor) filled with 20 mL aqueous solution. The reactor was then mounted on a hot plate maintained at a constant temperature of 60°C. The reaction was allowed to proceed for times varying from 2 to 10 hr. Finally, the substrates were annealed at 350°C for an hour. This procedure resulted in NiO nanoflakes on Au films.

The morphology of the NiO nanostructures has been investigated using a field-emission scanning electron microscope (FESEM) from Carl Zeiss. Optical absorption and structural properties of the nanostructures were studied using Shimadzu UV-Vis spectrophotometer and JEOL High Resolution Transmission Electron Microscope (HRTEM), respectively. Core level studies have been performed, in UHV, using a VG X-ray Photoelectron spectroscopy (XPS) system having an instrumental resolution of 0.9 eV. The spectra reported here were obtained with Mg Kα radiation at a pass energy of 20 eV. The emission angle of photoelectrons was kept at 30° with respect to surface normal. The C 1s line at 284.6 eV has been utilized for charge correction. A Shirley type background was removed from all the XPS spectra. CAFM measurements were performed using a Bruker AFM (Nanoscope V) setup. A schematic diagram for CAFM measurements is presented in fig. 7.1. By sweeping voltage(V) between the AFM tip and the bottom Au electrode, under sample bias condition, corresponding current (I) is measured . The voltages were sweeped from 0 to +8 V in the positive direction and from +8 to 0 V in the reverse direction. CAFM measurements have been performed on various regions of the sample.

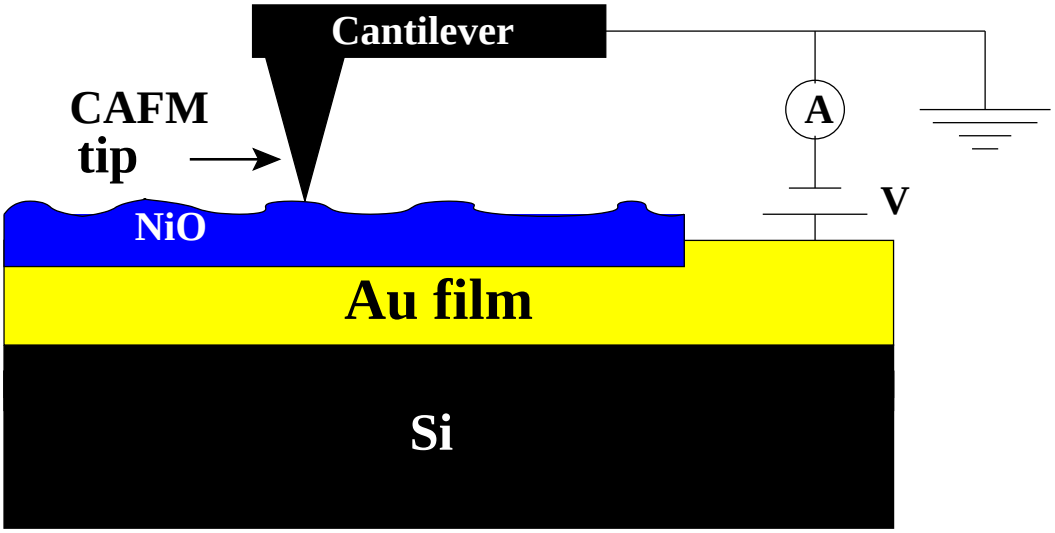

Figure 7.1: Schematic diagram for Conducting AFM (CAFM) measurements. For measuring I-V response, V is applied between the tip of the cantilever and the Au electrode. This voltage is sweeped and the corresponding I is measured.

7.3 Results and Discussions :

Figure 7.2 presents FESEM images of NiO nanostructures at various reaction times. Fig. 7.2 (a) displays an image after a reaction time of 6 hour where nanoflakes can be seen. The evolution of these nanoflakes, with reaction time can be observed in fig. 7.2 (b,c).

During the hydrothermal growth of NiO, nickel nitrate ($Ni(NO_3)_2$) acts as a source of Ni^{2+} ions and HMT ($C_6H_{12}N_4$) as a precipitant. The growth of NiO nanostructures takes place through following systematic reactions :

$$Ni(NO_3)_2 \rightarrow Ni^{2+} + 2NO_3^- \tag{7.1}$$

$$(CH_2)_6N_4 + 6H_2O \rightarrow 6HCHO + 4NH_3 \tag{7.2}$$

$$NH_3 + H_2O \leftrightarrow NH_4^+ + OH^- \tag{7.3}$$

$$Ni^{2+} + 4NH_3 \leftrightarrow Ni[(NH_3)_4]^{2+} \tag{7.4}$$

$$Ni^{2+} + 2OH^- \xrightarrow{60^\circ C} Ni(OH)_2 \tag{7.5}$$

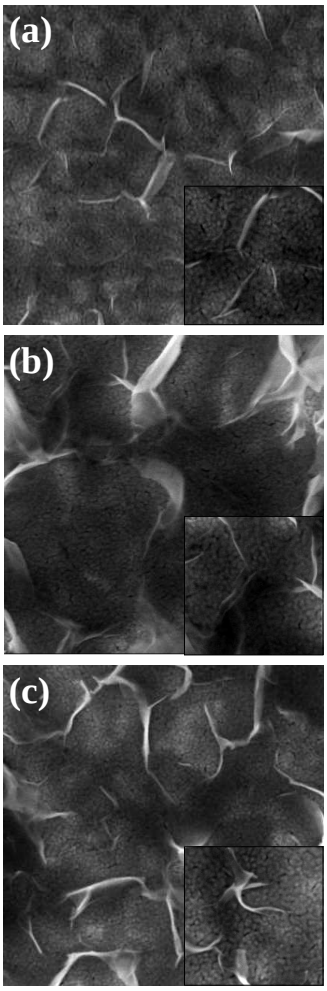

Figure 7.2: FESEM images (3×3 μm^2) from NiO nanostructures grown at different reaction time of (a) 6, (b) 8, and (c) 10 hr. Insets show high resolution image of nanoflakes from a (1×1 μm^2) region.

The last reaction process is

$$Ni(OH)_2 \xrightarrow{350^\circ C} NiO + H_2O \tag{7.6}$$

In the initial kinetics of hydrothermal growth, decomposition of nickel nitrate hexahydrate and HMT introduce Ni^{2+}, OH^- and ammonia in the aqueous solution (eqn. 7.1-7.3). Ni^{2+} ions form the hexa-aqua coordinated $Ni[(H_2O)_4]^{2+}$ species during reaction with H_2O. This gets converted into the thermodynamically more stable hexa-ammine complex $Ni[(NH_3)_4]^{2+}$ after reaction with ammonia (a stronger base and ligand compared to H_2O, eqn. 7.4). At elevated temperatures, this complex favors, according to eqn. 7.3 and 7.4, the formation of Ni^{2+} ions and releases NH_3 to provide OH^- ions in the aqueous solution [12,13]. Reaction between these ions

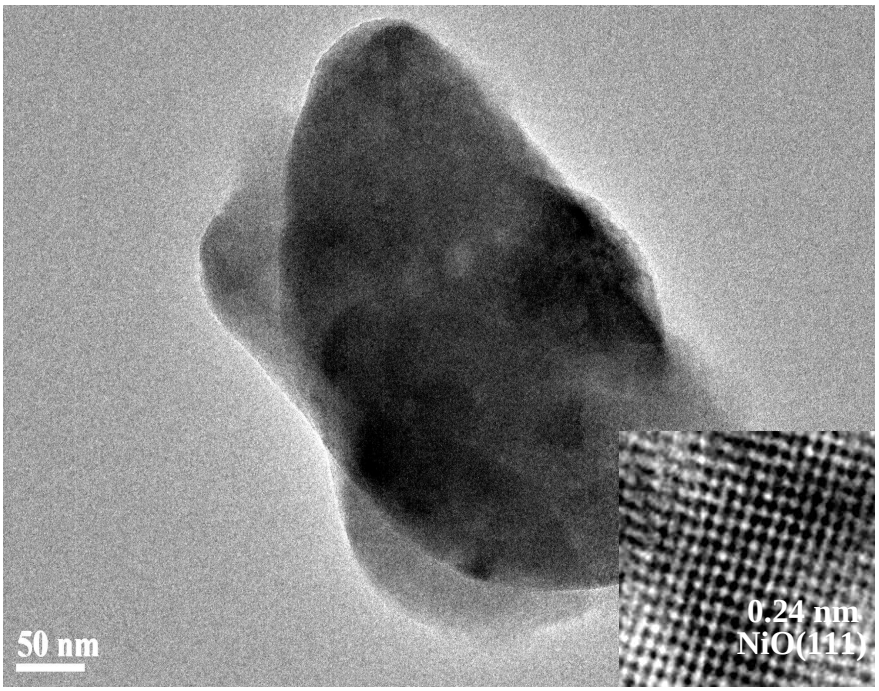

Figure 7.3: TEM image of NiO nanoflakes, deposited at 10 hr reaction time. Inset shows the HRTEM image of a 4.4 x 4.4 nm^2 region of NiO nanoflake.

leads to the precipitation of $Ni(OH)_2$ (eqn. 7.5). Finally, thermal decomposition of $Ni(OH)_2$ produces NiO nanostructures (by eqn. 7.6) via dehydration [14]. Removal of bonding water molecules, during dehydration, still retains the regular arrangement of Ni and O atoms in NiO lattice structure [14, 15]. Figure 7.3 presents the TEM image of a 350 nm nanostructure grown at the reaction time of 10 hr. Inset displays a high resolution lattice image of the nanoflake. The lattice fringes demonstrate an inter planer spacing of $\sim$ 0.24 nm from cubic NiO (111) planes [14] and suggest nanoflakes to be of crystalline nature.

XPS spectra from Ni(2p) region for NiO nanoflake are shown in fig. 7.4, for various reaction times. The XPS spectrum after the reaction time of 2 hr (fig. 7.4(a)), shows two distinct features at 852.5 and 853.8 eV associated with Ni^0 and Ni^{2+} states, respectively [15, 16]. These features represent the $Ni2p_{3/2}$ state of the metallic nickel and NiO, respectively [15, 16]. Being of similar intensity, these features suggest the existence of some metallic Ni on NiO nanoflakes. Moreover, the satellite features associated with the metallic Ni and NiO, labeled as Ni_{sat} and NiO_{sat}, respectively, are also observed at 858.3 and 859.8 eV [15,16]. The former represents the characteristic transition $c3d^{10}4s \rightarrow c3d^9 4s^2$ (c being a core hole) in metallic Ni, and latter the transition $c3d^9L \rightarrow c3d^{10}L^2$ (L being a ligand hole) in NiO [17]. For increasing reaction time,

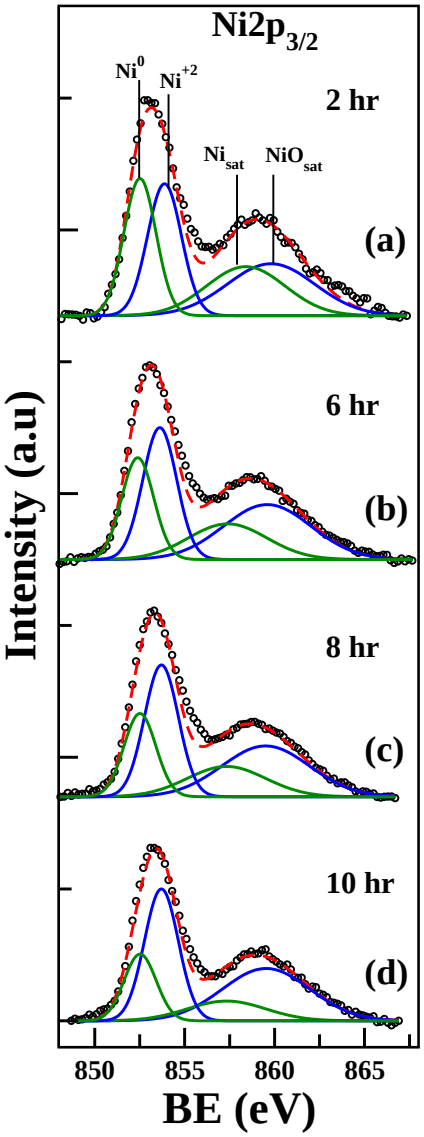

Figure 7.4: Ni(2p) XPS spectra from NiO nanostructures grown at reaction time of (a) 2, (b) 6, (c) 8 and (d) 10 hr. Peak fitted components for Ni^{2+}, Ni^{0} states and satellite features for NiO and Ni are shown.

the relative intensity of the Ni^{0} feature is observed to decrease, with respect to the Ni^{2+} feature. The associated satellite intensities of Ni^{0} and Ni^{2+} (i.e. Ni_{sat} and Ni^{2+}_{sat}) also demonstrate similar behavior (fig. 7.4). In the final reaction of hydrothermal growth process (eqn. 7.5), Ni^{2+} and OH^{-} react at 60°C leading to the formation of $Ni(OH)_2$. Calcining or annealing at 350°C of this $Ni(OH)_2$ forms NiO nanoflakes. The production of these nanoflakes depends on the concentrations of OH^{-} and Ni^{2+} in the solution as well as the reaction time. With increasing reaction time, the production of NiO increases due to enhanced availability of OH^{-}

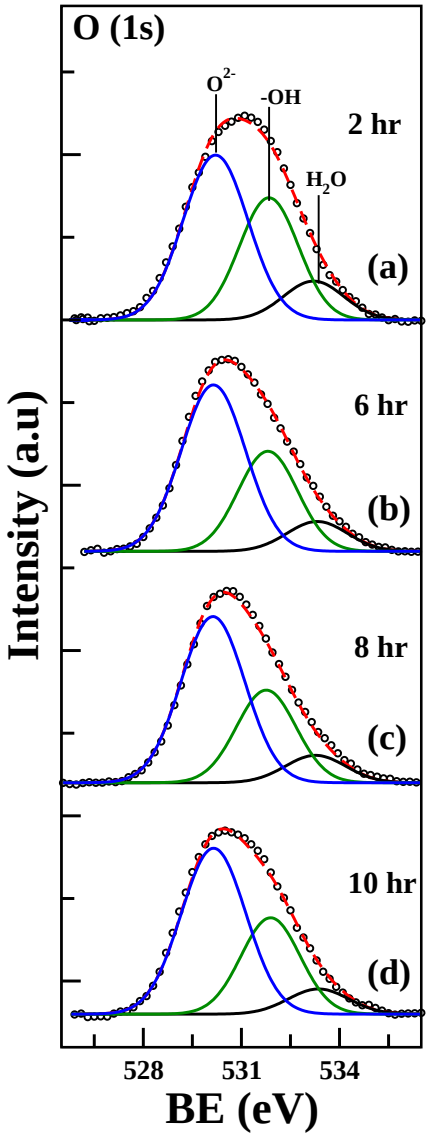

Figure 7.5: O(1s) XPS spectra from NiO nanostructures grown at reaction time of (a) 2, (b) 6, (c) 8 and (d) 10 hr. Peak fitted components for states related to O^{2-}, -OH and adsorbed H_2O are shown.

(as per reaction of eqn. 7.3). The enhancement in Ni^{2+} feature, in fig. 7.4, is a consequence of the creation of NiO nanoflakes with less metallic Ni for increasing reaction time. Core level XPS spectra from O (1s) region for NiO nanoflakes, grown at various reaction times, are shown in fig. 7.5. Spectra display three components at 530.2, 532.0 and 533.6 eV. The first feature is related to the O^{2-} state of NiO nanoflakes [16]. The latter two features correspond to the adsorption of -OH and H_2O, respectively [16, 18]. No significant variation in the relative intensity of these components, for various reaction times, is observed.

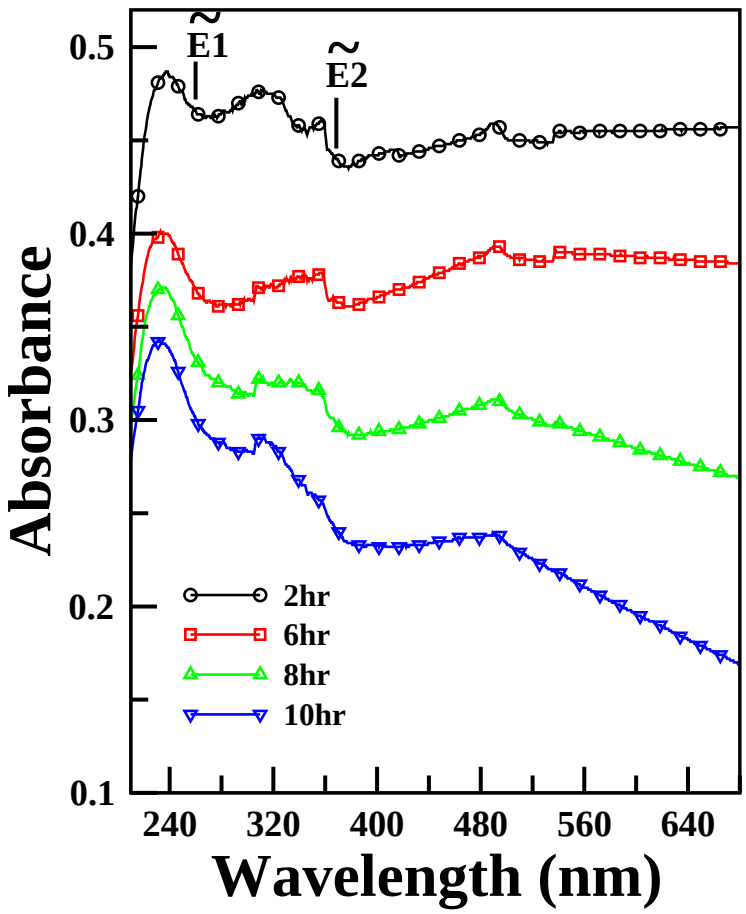

Figure 7.6: UV-Visible absorption spectra from NiO nanostructures grown at different reaction time. $\widetilde{E1}$ and $\widetilde{E2}$ designate the two band edges observed in NiO nanoflakes.

Figure 7.6 shows the optical absorption spectra from NiO nanoflakes for various reaction times. All absorption spectra show primarily two absorption edges, $\widetilde{E1}$ and $\widetilde{E2}$. The former is related to the direct bandgap transition in NiO, from O(2p) valence band to Ni(3d) derived conduction band [12, 19]. The latter is due to the A_{2g} to T_{2g} transition in Ni^{2+} ions located in oxygen octahedral sites [12, 13]. The feature seen at nearly 500 nm is related to Au plasmon feature from bottom gold electrode. NiO is a large bandgap (3.0-4.5 eV) p-type semiconductor with an absorbance tail in the visible region [20]. Interestingly in the present study, the highest photo-absorption has been observed for NiO nanostructures created at the smallest reaction time of 2hr. For these nanostructures, a high absorbance can be noticed for both, UV and visible, regions. Moreover, the absorbance response is reasonably flat, displaying nearly similar photo absorbance over all the wavelengths studied here. Although the absorption response behaviour also remains nearly flat for nanostructures forming after 6 hr reaction time,

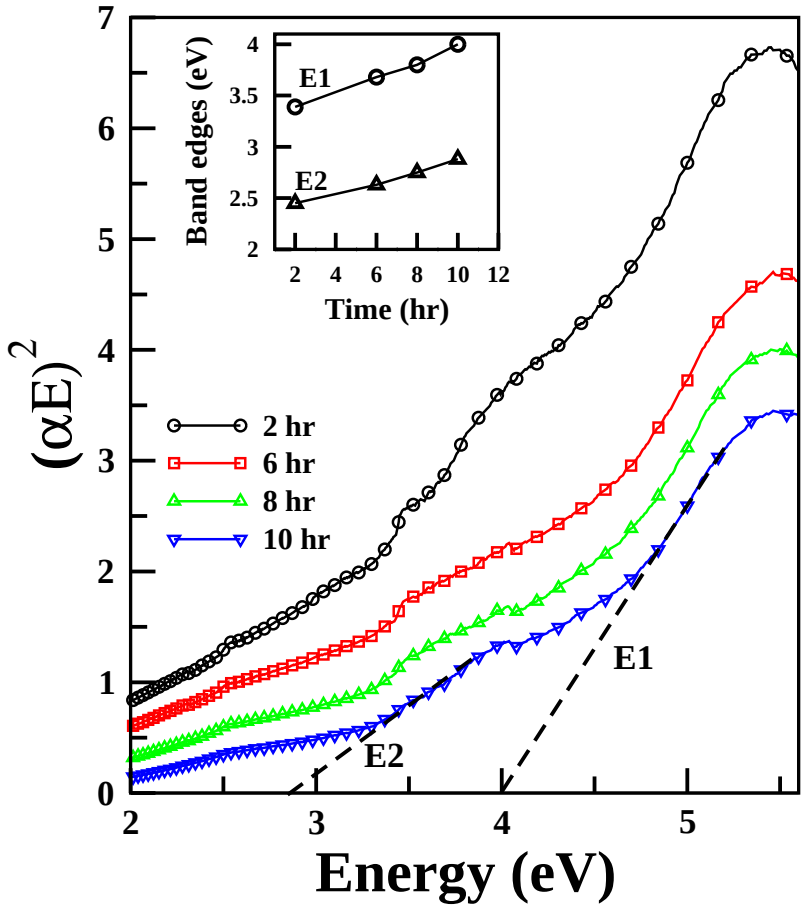

Figure 7.7: Tauc plots are shown for NiO nanostructures grown at different reaction time. α is the absorption coefficient and E is the photon energy. Inset shows the variations in E1 and E2 as a function of reaction time.

the absorbance is much lower. For nanostructures forming at 10 hr, a distinctly large absorption in the UV region, but a relatively lower absorption in the visible region, is observed.

Tauc plots, shown in fig. 7.7, have been generated using absorbance data (of fig. 7.6) and display two bandgaps, E1 and E2. These are respectively related to the band edges, $\widetilde{E1}$ and $\widetilde{E2}$, observed in fig. 7.6. The inset of fig. 7.7 displays E1 and E2 as a function of reaction time. For NiO nanostructures, created at 2 hr, E1 and E2 are at $\sim$3.40 and $\sim$2.45 eV, respectively. E1 observed here is similar to NiO bandgaps (3.0-4.5 eV) observed earlier [20, 21]. For higher reaction times, an increase in E1 is observed. For nanostructures created at 10 hr, E1 is found to be $\sim$4.0 eV. Thus, the smallest bandgap (E1) and highest absorbance, with similar response in UV and visible range, is observed for NiO flakes grown at 2 hr, whereas for the highest reaction time (10 hr), a distinctly high absorbance in the UV region, compared to visible region,

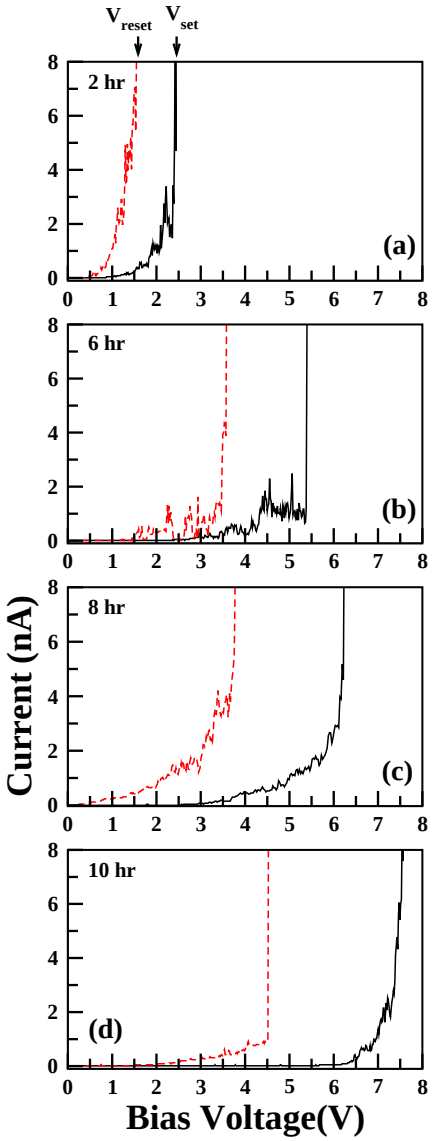

Figure 7.8: I-V characteristics from NiO nanoflakes fabricated at different reaction time of (a) 2, (b) 6, (c) 8 and (d) 10 hr.

accompanied by large bandgap, E1, is observed.

I-V characteristics from NiO nanoflakes are presented in fig. 7.8. For these measurements, voltage (V) is sweeped between AFM tip and the bottom (Au) electrode, on which NiO nanoflakes were grown and corresponding I is measured. For NiO nanoflakes grown for 2 hr reaction time, initially at small voltages no current is detected. The percolation threshold is reached at 1.1 V where small current is detected. A sharp rise in current, however, is observed with application of 2.4 V. Thus, nanoflakes which were under high resistance state (HRS) undergo a transition to low resistance state (LRS) at 2.4 V. At the percolation threshold, few weak

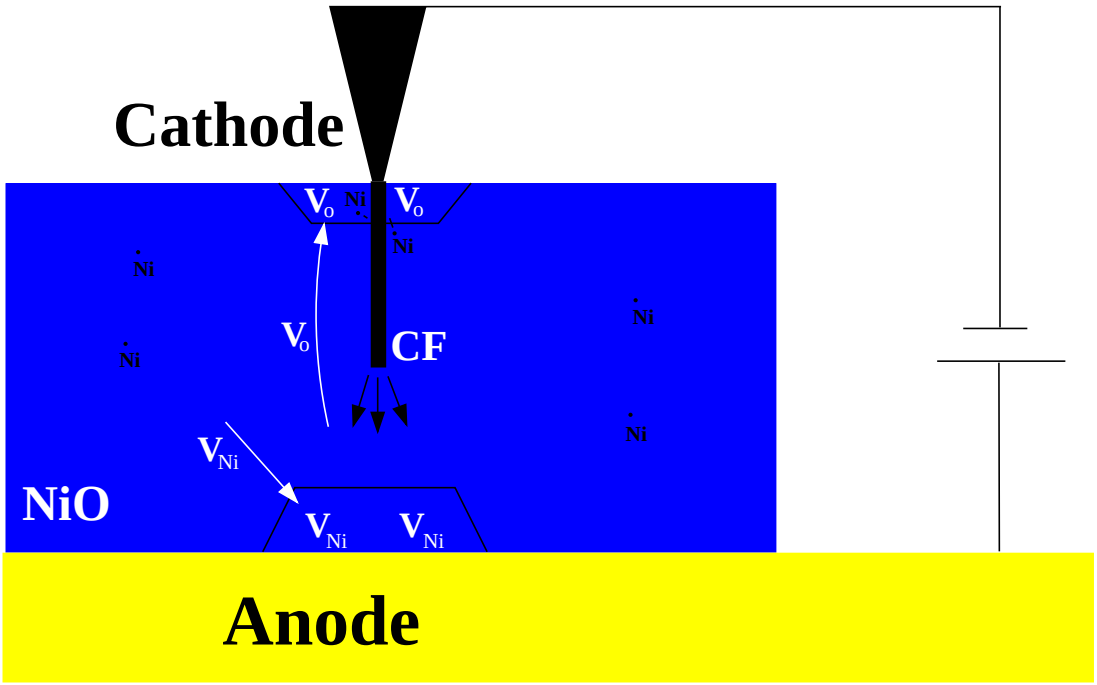

Figure 7.9: Process of Conducting Filament formation in NiO. Contribution from metallic Ni (labelled as dots) from flakes, in CF formation, is also shown.

conducting paths get created.

NiO inherently possess nickel vacancy (V_{Ni}) type defects but develop oxygen vacancies (V_o) when reduced [22–25]. Upon application of the voltage to NiO device, as shown in fig. 7.9, oxygen and nickel vacancies will respectively migrate towards the cathode and anode. Oxygen vacancies are also generated at the anode [3], which will also move towards and get accumulated near cathode. As a result, their is a decrease in concentration of nickel vacancies near cathode region, and oxygen vacancies near anode region. Presence of large number of oxygen vacancies, in the cathode region, produce a thermodynamic instability. As a result, the NiO in the cathodic region phase separates into Ni and NiO. The metallic Ni phase grows and forms a conducting path (CF) from cathode towards anode. After this process of electroforming, the electroformed state is said to be attained when metallic Ni phase touches the anode. Processes of Ni filament growth during electroforming is shown in figure 7.9. Presence of metallic Ni in NiO films, as shown by XPS results of fig. 7.4, also contribute in the formation of CF in the present study. Metallic Ni, present near the phase separated region will be primarily playing this role. The transition from HRS to LRS occurs when such paths become stronger and larger in number. The fluctuations near percolation threshold, in fig. 7.8, are due to the random

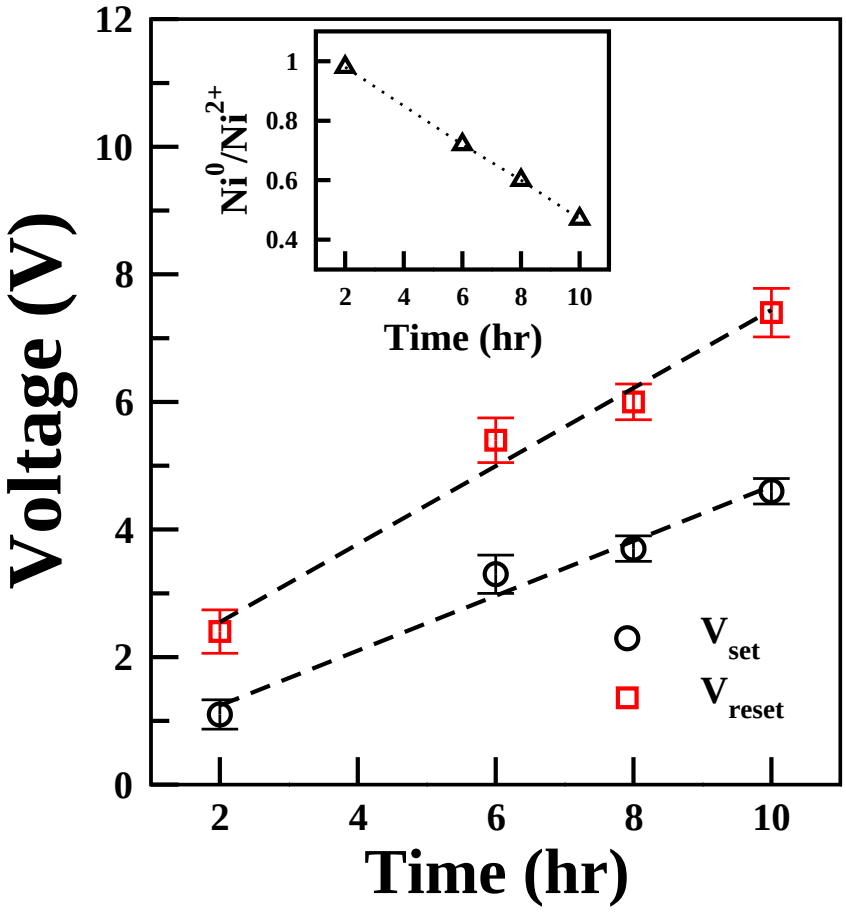

Figure 7.10: Variations in V_{set} and V_{reset} voltages as a function of reaction time. Inset shows the variations in the ratio, Ni^0/Ni^{2+}, in NiO nanoflakes.

telegraphic noise [2] or variations in the metal Ni concentration.

After the HRS to LRS transition occurs, V between CAFM tip and Au electrode (see fig. 7.1), is decreased and is sweeped in the reverse direction up to the stage when a sharp decrease in current is noticed (see fig. 7.8). The latter transition is termed as LRS to HRS and occurs at 1.1 V for NiO nanoflakes grown at 2 hr. At this stage, the conducting filaments, that had developed for conduction, become severely ruptured. The voltage required for the transition from HRS to LRS is defined as V_{set} voltage, whereas V_{reset} voltage is needed for driving LRS to HRS. The transitions from HRS to LRS at V_{set}, and LRS to HRS at V_{reset} suggest existence of two stable, HRS and LRS, states for NiO nanoflakes. Moreover, this behaviour is reversible indicating that these NiO nanostructures demonstrate *bi-stable reversible switching* behaviour. This switching is also of unipolar nature with both, V_{set} and V_{reset}, being of same positive polarity.

The V_{set} and V_{reset} voltages observed here for NiO nanoflakes are plotted in fig. 7.10 as a function of reaction time. Both the voltages demonstrate a nearly linear increase with reaction time. For the reaction time of 2 hr, only a small set voltage (V_{set}) is required. This observation is associated with the fact that at this stage NiO flakes are rich in Ni^0, as demonstrated by XPS studies in fig. 7.4. High metallic content in these nanostructures results in the percolation of current at a lower threshold voltage. At higher reaction times, larger V_{set} values are observed. Inset of fig. 7.10 shows the ratio of Ni^0 to Ni^{2+}, as calculated using the XPS results of fig. 7.4, at various reaction times. The metallic content, Ni^0, decreases in NiO nanoflakes with the reaction time leading to higher V_{set} voltage for attaining the conduction. With increasing reaction time, higher V_{reset} voltages are also observed. High V_{reset} voltages, for higher reaction times are also due to the fact that the lower metallic Ni content (inset fig. 7.10) does not allow continuous conducting filaments at lower voltages and the CF bonds, leading to conduction phenomena, rupture. Mobile oxygen vacancy and Nickle vacancy, under the applied bias, will also be responsible for the observed phenomenon [3]. These results indicate that V_{set} and V_{reset} voltages crucially depend on the metallic Ni present in NiO nanoflakes.

7.4 Conclusion :

In conclusion, NiO nanoflakes have been fabricated, with simple hydrothermal growth process, as a function of reaction time. NiO nanoflakes, grown at the smallest reaction time (of 2 hr), delineate the highest photo-absorbance response, in addition to displaying the smallest bandgap. The nanoflakes grown at 10 hr, however demonstrate distinct UV absorption conjugated with the largest bandgap. With the detailed quantitative investigations of I-V characteristics, it is observed that the metallic Ni in NiO nanostructures, along with the mobile oxygen vacancies and Ni vacancies, controls the voltages for the formation and rupturing of conducting filaments. These NiO flakes demonstrate *bi-stable reversible switching* behaviour of unipolar nature. NiO nanoflakes demonstrating photo absorption response and resistive switching character, that can be modulated with reaction time, will be important in optoelectronic, electrochromic and RS based memory devices.

Bibliography

[1] K. Jung, J. Choi, Y. Kim, H. Im, S. Seo, R. Jung, D. Kim, J. S. Kim, B. H. Park, and J. P. Hong, J. Appl. Phys. **103**, 034504 (2008).

[2] F. Nardi, D. Deleruyelle, S. Spiga, C. Muller, B. Bouteille, and D. Ielmini, J. Appl. Phys. **112**, 064310 (2012).

[3] D. S. Jeong, R. Thomas, R. S. Katiyar, J. F. Scott, H. Kohlstedt, A. Petraru, and C. S. Hwang, Rep. Prog. Phys. **75**, 076502 (2012).

[4] G. Wang, X. Lu, T. Zhai, Y. Ling, H. Wang, Y. Tong, and Y. Li, Nanoscale **4**, 3123 (2012).

[5] P. Justin, S. K. Meher, and G. R. Rao, J. Phys. Chem. C **114**, 5203 (2010).

[6] S. Seo, M. J. Lee, D. H. Seo, S. K. Choi, D. S. Suh, Y. S. Joung, I. K. Yoo, I. S. Byun, I. R. Hwang, S. H. Kim, and B. H. Park, Appl. Phys. Lett. **86**, 093509 (2005).

[7] N. Alidoust, M. C. Toroker, J. A. Keith, and E. A. Carter, ChemSusChem **7**, 195 (2014).

[8] J. Sullaphen, K. Bogle, X. Cheng, J. M. Gregg, and N. Valanoor, Appl. Phys. Lett. **100**, 203115 (2012).

[9] R. Waser, R. Dittmann, G. Staikov, and K. Szot, Adv. Mater. **21**, 2632 (2009).

[10] Y. H. You, B. S. So, J. H. Hwang, W. Cho, S. S. Lee, T. M. Chung, C. G. Kim, and K. S. An, Appl. Phys. Lett. **89**, 222105 (2006).

[11] S. Lee, I. Hwang, S. Oh, S. Hong, Y. Kim, Y. Nam, K. Lee, C. Yoon, W. Kim, and B. H. Park, Scie. Rep. **4**, 06871 (2014).

[12] J. Gangwar, K. K. Dey, S. K. Tripathi, M. Wan, R. R. Yadav, R. K. Singh, Samta, and A. K. Srivastava, Nanotechnology **24**, 415705 (2013).

[13] Y. Cui, C. Wang, S. Wu, G. Liu, Z. F. Zhanga, and T. Wanga, CrystEngComm **13**, 4930 (2011).

[14] J. Zhu, Z. Gui, Y. Ding, Z. Wang, Y. Hu, and M. Zou, J. Phys. Chem. C **111**, 5622 (2007).

[15] N. Kitakatsu, V. Maurice, C. Hinnen, and P. Marcus, Surf. Sci. **407**, 36 (1998).

[16] M. C. Biesinger, B. P. Payne, L. W. M. Lau, A. Gerson, and R. S. C. Smart, Surf. Int. Anal. **41**, 324 (2009).

[17] A. P. Grosvenor, M. C. Biesinger, R. S. Smart, and N. S. McIntyre, Surf. Sci. 600, **9**, 1771 (2006).

[18] P. Prieto, V. Nistor, K. Nouneh, M. Oyama, M. Abd-Lefdil, and R. Daz, Appl. Surf. Sci. **258**, 8807 (2012).

[19] K. Oka, T. Yanagida, K. Nagashima, M. Kanai, B. Xu, B. H. Park, H. K. Yoshida, and T. Kawai, J. Ame. Chem. Soc. **134**, 2535 (2012).

[20] T. K. Townsend, “Inorganic Metal Oxide nanocrystal Photocatalysts for Solar Fuel generation from Water”, publ. Springer (2014).

[21] G. A. Sawatzky and J. W. Allen, Phys. Rev. Lett. **53**, 2339 (1984).

[22] J. A. Rodriguez, J. C. Hanson, A. I. Frenkel, J. Y. Kim, and M. Perez, J. Am. Chem. Soc. **124** 346, (2001).

[23] S. Wang, M. Awano, and K. Maeda, J. Electrochem. Soc. **150**, D209 (2003).

[24] S. P. Mitoff, J. Chem. Phys. **35**, 882 (1961).

[25] T. Karakasidis, and M. Meyer, Phys. Rev. B **55**, 13853 (1997).

Chapter 8

Summary and Future Scope

Present thesis discusses the fabrication of nanostructures of TiO_2, ZnO, NiO and nanopatterned surfaces. Metal oxide nanostructures display many exciting and technologically useful applications in photocatalysis, photovoltaic cells, memory devices, sensors, opto-electronics, spintronics and resistive switching. This is owing to their excellent and important properties like chemical stability, high reactivity, bio-compatibility, non-toxicity etc. The nanostructures, discussed here, have been achieved by the process of self assembly and express many interesting and exciting behaviors like enhanced photo-absorption, magnetic response, resistive switching characteristics etc.

Chapter-1 presents basic concepts, theoretical description of nanostructure formation and nano-patterning of surfaces along with their importance in current research. Nanostructures have been fabricated through several methods like ion irradiation, atom beam sputtering and hydrothermal growth. The synthesis methods, characterization techniques, utilized here, and the properties of materials are discussed in **chapter-2**.

Chapter-3 presents the fabrication and photoabsorption behaviour of 2-dimensional nanostructures, created via ion irradiation of TiO_2 (110) single crystals by low energy ion beams. Irradiation techniques provide a powerful method for the formation of self-assembled nanostructures. Nanostructures and nanopatterned surfaces, obtained by this technique, can be generated in large area in a technologically single step. Patterns are created on the surface through the development of instability due to competing erosive and diffusive processes. TiO_2 (110) surfaces have been bombarded by Ar^+ ions of 60 keV, from an ECR source, at a variety of fluences ranging from 5×10^{15} to 5×10^{17} ions/cm^2. Ion irradiation also leads to the creation of oxygen vacancies, due to the preferential sputtering of oxygen atoms. This results in the formation of Ti-rich regions on the surface which act as the nucleation centers for the development of TiO_2

nanostructures. The nanostructures evolve with fluence and grow in size. The oxygen vacancy states, Ti^{3+}, however, display saturation beyond a critical fluence. Surprisingly, the highest photoabsorption, in UV-visible wavelength, is demonstrated by nanostructures of 15 nm size and not the smaller nanostructures with larger surface areas. An intricate dependency of photo-absorbance response, from TiO_2 nanostructure, on the size of the nanostructure and number of vacancy states is observed here. With the detailed quantitative investigation of oxygen vacancy states, it is demonstrated that competition between the size of nanostructures and the number of vacancy states controls the photo- absorption properties. A small bandgap widening due to quantum confinement effects is also observed. The complex relationship between these factors is responsible for the anomalous absorption response that has been observed here in the absence of any dopant. This can have extensive implications in the area of TiO_2 based photocatalytic devices.

Chapter-4 reports the magnetic properties of the TiO_2 nanostructures, fabricated by ion beam sputtering of TiO_2 single crystals in chapter 3 . SQUID investigations of TiO_2 nanostructures (of size 5, 10, 25nm) display a direct correlation between the size and their magnetic behavior. Small, single domained TiO_2 nanostructures, of $\sim$5 nm size, show super- paramagnetic (SPM) behavior. Ferromagnetic behavior, however, is demonstrated by bigger nanostructures. Nano- dimensional domain size estimates obtained through the Langevin function fitting of magnetization results suggest the presence of a magnetically inert layer on nanostructures. Results, presented here in the absence of any dopant material, will be significant for spintronic devices.

Chapter-5 discusses the photo-absorption properties of constrained TiO_2 nanostructures fabricated by Ar^+ ion irradiation at higher irradiation fluences of 6×10^{17} to 1×10^{19} ions/cm^2. The nanostructures are anisotropic in nature, being elongated along [001] direction. Though, the anisotropy of nanostructures increases with irradiation fluence, their width does not grow proportionally. As a result, the nanostructures are constrained along $[1\bar{1}0]$ direction. An asymmetric diffusion of mobile species, Ti^{3+} and itinerant Ti, created during the preferential sputtering of TiO_2, play an important role in regulating the self organization and the anisotropy of the nanostructures. Photo-absorption response demonstrates, surprisingly, an exponentially decaying dependence on the nanostructure- length along [001]. With this being the fast diffusion direction for the mobile species, results show their immense control on surface morphology. These results, obtained in the absence of any dopant elements, can lead to fascinating con-

sequences for exciting photo- catalytic properties of self assembled nano- systems of TiO_2 through controlled designing of their morphology.

Chapter-6 presents the formation of ZnO nanostructures through atom beam sputtering technique. 1.5 keV Ar atom beam were utilized to irradiate ZnO(0001) surfaces at two different incident angles leading to the formation of self-assembled crystalline nanostructures of two different sizes. The morphology of the surface, upon irradiation, is determined by the undergoing competitive processes of erosion and diffusion. Role of preferential sputtering of low mass oxygen atoms is also very important. XPS results indicate development of Zn rich sites on the sputtered surfaces which promote the nucleation of the nanostructures. Among the different sizes of nanostructures studied here, bigger (78 nm) nanostructures demonstrate hexagonal closed packed ordering and long ranged periodic behavior. The smaller nanostructures (60 nm) however do not display any ordering or periodicity. The bigger nanostructures, also displaying some new crystalline phases, show higher photo- absorption response. The enhanced photo response is primarily related to the bandgap narrowing by $\sim$0.09 eV, which occurs due to the creation of Zn interstitials during irradiation. These results are significant as they have been obtained in the absence of any dopant element and can be important for photocatalytic applications.

Chapter-7 presents the photo absorption response and resistive switching (RS) properties of NiO nanoflakes, grown by hydrothermal method. Nanoflakes grown at low reaction time (2 hr), display a very high, and a nearly similar, photo-absorption response, both in both UV and visible regions. These nanostructures also demonstrate smallest bandgap. The nanoflakes grown at the largest time (10 hr) however show a very distinct UV photoabsorption along with the largest bandgap. The NiO nanoflakes devices were also fabricated here with gold as bottom electrode. Detailed quantitative investigations of I-V characteristics have been carried out using CAFM technique. By this method resistive switching behavior in nanodimension regions can be explored. The results presented here show that the metallic Ni, in NiO nanostructures, controls the voltages for the formation and rupturing of conducting filaments necessary for switching. These NiO flakes demonstrate *bi-stable reversible switching* behaviour of unipolar nature. Both, photo absorption response and resistive switching character, shown by NiO nanflakes, display interesting variations and can be tuned with reaction time. Such multifunctional properties can be important in optoelectronic, electrochromic and RS based memory devices.

Present studies display the feasibility of several potential applications of wide bandgap materials as renewable energy sources and photocatalysis. There is an enormous potential for observed visible light activity of TiO_2 and ZnO, in the absence of any dopant, in photovoltaics as well as in photocatalyst based applications. An increase in photoabsorption properties of TiO_2 and ZnO is observed. This occurs due to the development of Ti or Zn rich nanostructures on the surface as well as the creation of oxygen vacancy sites. The oxygen vacancies get modulated by small nanostructures at low fluences and their fine control will be useful in providing detailed precise parameters for enhanced photoabsorption. In addition, observation of superparamagnetism in single domained quantum confined TiO_2 nanostructures can provide important template for spintronics and multiferroics based devices. The resistive switching phenomena, observed in NiO nanostructures, would be of immense use for resistive switching based random access memory devices. In the present study the role of metallic Ni in the formation of conducting filaments during HRS to LRS has been investigated. For detailed understanding of resitive switching mechanism in NiO, more exploration of the forming and rupturing behaviour is required.